








# A systematic analysis of the X-ray emission in optically selected tidal disruption events: observational evidence for the unification of the optically and X-ray selected populations

MURYEL GUOLO <sup>1</sup>, SUVI GEZARI <sup>2,1</sup>, YUHAN YAO <sup>3,4,5</sup>, SJOERT VAN VELZEN <sup>6</sup>, ERICA HAMMERSTEIN <sup>7,8,9</sup>,  
S. BRADLEY CENKO <sup>8,10</sup> AND YARONE M. TOKAYER <sup>11</sup>

<sup>1</sup>*Bloomberg Center for Physics and Astronomy, Johns Hopkins University, 3400 N. Charles St., Baltimore, MD 21218, USA*

<sup>2</sup>*Space Telescope Science Institute, 3700 San Martin Drive, Baltimore, MD 21218, USA*

<sup>3</sup>*Cahill Center for Astrophysics, California Institute of Technology, MC 249-17, 1200 E California Boulevard, Pasadena, CA 91125, USA*

<sup>4</sup>*Miller Institute for Basic Research in Science, 468 Donner Lab, Berkeley, CA 94720, USA*

<sup>5</sup>*Department of Astronomy, University of California, Berkeley, CA 94720, USA*

<sup>6</sup>*Leiden Observatory, Leiden University, PO Box 9513, 2300 RA Leiden, The Netherlands*

<sup>7</sup>*Department of Astronomy, University of Maryland, College Park, MD 20742, USA*

<sup>8</sup>*Astrophysics Science Division, NASA Goddard Space Flight Center, Mail Code 661, Greenbelt, MD 20771, USA*

<sup>9</sup>*Center for Research and Exploration in Space Science and Technology, NASA/GSFC, Greenbelt, MD 20771, USA*

<sup>10</sup>*Joint Space-Science Institute, University of Maryland, College Park, MD 20742, USA*

<sup>11</sup>*Department of Physics, Yale University, P.O. Box 208120, New Haven, CT 06520, USA*

## ABSTRACT

We present a systematic analysis of the X-ray emission of a sample of 17 optically selected, X-ray-detected tidal disruption events (TDEs) discovered between 2014 and 2021. The X-ray light curves show a diverse range of temporal behaviors, with most sources not following the expected power-law decline. The X-ray spectra are mostly extremely soft and consistent with thermal emission from the innermost region of an accretion disk, which cools as the accretion rate decreases. Three sources show formation of a hard X-ray corona, at late-times. The spectral energy distribution shape, probed by the ratio ( $L_{\text{BB}}/L_{\text{X}}$ ) between the UV/optical and X-ray, shows a wide range  $L_{\text{BB}}/L_{\text{X}} \in (0.5, 3000)$  at early-times, and converges to disk-like values  $L_{\text{BB}}/L_{\text{X}} \in (0.5, 10)$  at late-times. We estimate the fraction of optically discovered TDEs with  $L_{\text{X}} \geq 10^{42}$  erg s<sup>-1</sup> to be at least 40%, and show that X-ray loudness is independent of black hole mass. We argue that distinct disk formation time scales are unlikely to fully explain the diverse range of X-ray evolutions. We combine our sample with X-ray discovered ones to construct an X-ray luminosity function, best fitted by a broken power-law, with a break at  $L_{\text{X}} \approx 10^{44}$  erg s<sup>-1</sup>. We show that there is no dichotomy between optically and X-ray selected TDEs, instead there is a continuum of early time  $L_{\text{BB}}/L_{\text{X}}$ , at least as wide as  $L_{\text{BB}}/L_{\text{X}} \in (0.1, 3000)$ , with optical/X-ray surveys selecting preferentially, but not exclusively, from the higher/lower end of the distribution. Our findings are consistent with unification models for the overall TDE population.

*Keywords:* Tidal disruption (1696) – X-ray transient sources (1852) – Supermassive black holes (1663)  
– Time domain astronomy (2109) – High energy astrophysics (739) – Accretion (14)

## 1. INTRODUCTION

The occasional tidal disruption of a star that approaches close enough to a massive black hole (MBH) was predicted by theorists as a signpost for MBHs lurking in the center of galaxies (Hills 1975; Rees 1988; Ulmer 1999). These luminous events, called tidal disruption events (TDE), are observed throughout the entire electromagnetic spectrum, and are now a well-established class of transients (see recent review by Gezari 2021). TDEs are a unique opportunity to probe

the existence of quiescent black holes in the low mass end of the MBH’s mass function ( $< 10^8 M_{\odot}$ ). At higher black hole masses, a TDE is not observable; stars are swallowed whole since the tidal disruption radius lies inside the event horizon (Hills 1975; van Velzen 2018; Yao et al. 2023b).

The first observational evidence for TDEs came from the detection of X-ray flares from the centers of quiescent galaxies during the *ROSAT* all-sky survey (RASS) in 1990–1991 (e.g., Bade et al. 1996; Grupe et al. 1999;

Komossa & Greiner 1999; Greiner et al. 2000). The flares exhibited soft spectra with temperatures  $T \sim 10^6$  K (for a review on X-ray selected TDEs, see Saxton et al. 2020). Since 2020, the Spektrum-Roentgen-Gamma (*SRG*) mission (Sunyaev et al. 2021), with its sensitive eROSITA telescope (Predehl et al. 2021), and six-month cadenced all-sky surveys, has become the most prolific discoverer of TDEs in X-rays, presenting thirteen new sources discovered during the first two All-sky scans (Sazonov et al. 2021).

The discovery of TDEs has increased dramatically in the last few years due to the operation of wide-field optical surveys, such as iPTF (Blagorodnova et al. 2017, 2019; Hung et al. 2017), Pan-STARRS (Gezari et al. 2012; Chornock et al. 2014; Holoien et al. 2019), ASASSN (Holoien et al. 2014, 2016a,b; Wevers et al. 2019a), and ZTF (van Velzen et al. 2019, 2021; Hammerstein et al. 2023a; Yao et al. 2023b); with ZTF now dominating the number of discoveries with a rate of  $\sim 10$  per year (Hammerstein et al. 2023a; Yao et al. 2023b). Although, the number of optically selected TDEs dominates over the ones discovered by means of high-energy observations, the nature of what is powering their bright optical flares is uncertain. Unlike the soft X-ray component detected in some optically selected TDEs – which is similar to the X-ray selected TDEs and is consistent with thermal emission from the inner radii of an accretion disk – the UV/optical component seems, in most cases, not consistent with the direct emission from the Rayleigh-Jeans tail of the expected disk to form from the circularization of the stellar debris streams around a  $10^5 - 10^8 M_\odot$  black hole. This implies the existence of an unknown, larger emitting structure that competing interpretations invoke to be either produced as a result of reprocessing of the extreme UV and X-ray emission (Miller et al. 2015; Dai et al. 2018; Parkinson et al. 2022; Thomsen et al. 2022), or from shocks between intersecting debris streams themselves (Shiokawa et al. 2015; Piran et al. 2015; Jiang et al. 2016; Bonnerot et al. 2017).

Besides the origin of optical emission, a second important aspect of optically-selected TDEs is that most of them are X-ray faint. In the unifying reprocessing scenario, the distinct classes of TDEs are given by the viewing angle with respect to the accretion disk and its associated reprocessing layer; the X-ray bright, ‘optically faint’ TDEs are the ones observed more face-on, the optically bright, X-ray faint are edge-on, while the ones that show both emission components are seen at intermediate angles (Guillochon et al. 2014; Dai et al. 2018; Parkinson et al. 2022). In this scenario, X-rays from sources at intermediate angles can only break out after the reprocessing gas has expanded enough to be-

come transparent to X-rays (Metzger & Stone 2016; Lu & Kumar 2018; Thomsen et al. 2022). However, in the stream-stream collision scenario, the intrinsically X-ray faint TDEs have been proposed to be a result of delayed accretion, due to the timescale required for the circularization of the debris into an appreciable accretion disk (Gezari et al. 2017; Liu et al. 2022).

In addition to the study of nascent accretion disks, TDEs can be used to study the formation and evolution of other physical structures related to MBH accretion. Relativistic (e.g., Cenko et al. 2012; Pasham et al. 2015; Zauderer et al. 2011; Brown et al. 2017; Pasham et al. 2023; Yao et al. 2023a) and non-relativistic (e.g., Alexander et al. 2016; Bright et al. 2018; Stein et al. 2021) jets, as well as outflows with velocities varying from 200-600  $\text{km s}^{-1}$  (Miller et al. 2015; Krolik et al. 2016; Cenko et al. 2016; Blagorodnova et al. 2018; Kosec et al. 2023) up to  $0.2c$  (e.g., Lin et al. 2015; Kara et al. 2018) have been detected in several sources.

This paper presents an analysis of the X-ray light curves, X-ray spectral evolution, and broadband UV/optical/X-ray spectral energy distribution (SED) evolution of 16 X-ray detected, optically discovered TDEs between 2014 and December 2021, and one more simultaneous discovered by *SRG/eROSITA* (AT2020ksf) but with extensive UV/optical follow-up. We present new *XMM-Newton* data for half of our sources and systematically reanalyze all publicly available ZTF, *Neil Gehrels Swift Observatory* and *XMM-Newton* data presented in previous studies on individual sources. In §1.1 we present our sample and its selection criteria. In §2 we present the data and describe its basic analyses. In §3 we present a detailed discussion on the X-ray spectral fitting in TDEs and its general properties. In §4 we show our results and their interpretations, which are discussed in terms of the current literature in §5; our conclusion are presented in §6.

We adopt a standard  $\Lambda$ CDM cosmology with matter density  $\Omega_M = 0.3$ , dark energy density  $\Omega_\Lambda = 0.7$ , and the Hubble constant  $H_0 = 70 \text{ km s}^{-1} \text{ Mpc}^{-1}$ . Optical and UV magnitudes are reported in the AB system. Uncertainties of X-ray model parameters are reported at the 68% confidence level, and upper limits are reported at  $3\sigma$ .

### 1.1. Sample Selection

Aiming to explore the diversity of X-ray evolution in optically selected TDEs, we draw our sample from sources discovered by optical time-domain surveys. We compile sources from ZTF sample papers (van Velzen et al. 2021; Hammerstein et al. 2023b; Yao et al. 2023b) as well as studies on individual sources from other sur-

veys (Wyrzykowski et al. 2017; Holoien et al. 2016a,b; Wevers et al. 2019a). We did not consider nuclear transients with pre-existing active galactic nuclei (AGN) from TDE candidates, these excludes those with host galaxies with AGN-like broad emission lines or *NEOWISE* (Mainzer et al. 2014) Mid Infrared (MIR) variability before the transient, as well as  $W1 - W2$  MIR color exceeds AGN selection criteria (e.g., Stern et al. 2012). We limited the sample based on the epoch of discovery; given that the first optically discovered TDE to be systematically followed-up by X-ray telescopes was ASASSN-14li, we delimited the sample with sources discovered after 2014. Our discovery epoch criteria also exclude those sources discovered after December 2021, allowing us to have more than one year of data for the entire sample. Finally we require every source to have at least one  $3\sigma$  *Swift*/XRT detection<sup>1</sup>, yielding our final sample of 17 optically selected X-ray detected TDEs. The complete sample and the basic information on the sources are shown upper portion of Table 1, in Fig. 1 we show some the distribution of some basic properties of our sample. Besides the observations on the 17 sources that make our main sample, we also present deep upper-limits based on *XMM-Newton* observations of another 9 optically-selected TDEs that never show detectable X-ray emission; these sources are shown the bottom portion of Table 1.

## 2. OBSERVATIONS, DATA REDUCTION AND ANALYSES

### 2.1. Observations and Data Reduction

#### 2.1.1. *XMM-Newton*

The primary data set underlying this work is based on *XMM-Newton* observations, these were obtained primarily from a series of Announcement of Opportunity (AO) programs (AO-18 84259, AO-20 88259, P.I.: Gezari, and AO-21 90276 P.I. Yao) aimed on the deep X-ray follow-up of ZTF-discovered TDEs. These observations were taken in Full Frame mode with the thin filter using the European Photon Imaging Camera (EPIC; Strüder et al. 2001) and are presented here for the first time. We also included publicly available observations from several other AO and Director Discretionary Time (DDT) proposals. The details on the *XMM-Newton* observations are shown in Table 2.

The observation data files (ODFs) were reduced using the *XMM-Newton* Standard Analysis Software (SAS; Gabriel et al. 2004). The raw data files were then processed using the `epproc` task. Since the pn instrument generally has better sensitivity than MOS1 and MOS2, we only analyze the pn data. Following the *XMM-Newton* data analysis guide, to check for background activity and generate “good time intervals” (GTIs), we manually inspected the background light curves in the 10–12 keV band. Using the `evselect` task, we only retained patterns that correspond to single and double events (`PATTERN<=4`). The source spectra were extracted using a source region of  $r_{\text{src}} = 35''$  around the peak of the emission. The background spectra were extracted from a  $r_{\text{bkg}} = 108''$  region located in the same CCD. The ARFs and RMF files were created using the `arfgen` and `rmfgen` tasks, respectively. Some of the observations for ASASSN-14li and AT2020ocn presented pile-up effects. Therefore, we followed the SAS guide<sup>2</sup> by excising the core of the point spread function (PSF), up to a radius where the pile-up fraction becomes negligible following the `epatplot` command results.

#### 2.1.2. *Neil Gehrels Swift Observatory*

All the sources were observed by the X-ray Telescope (XRT; Burrows et al. 2005) and the Ultra-Violet/Optical Telescope (UVOT; Roming et al. 2005) on board *Neil Gehrels Swift Observatory* (Gehrels et al. 2004). The number of observations varies from a few for the more distant sources to a hundred for the most well-sampled sources.

The 0.3–10 keV X-ray counts light curves were produced using the UK Swift Data center online XRT data products tool, which uses the HEASOFT v6.22 software (Arnaud 1996). We used a fixed aperture at the ZTF coordinate of the transient, generating one count rate point per visit (i.e., per ObsID) for most of the sources; for faint sources (AT2018zr, AT2018hyz and AT2019qiz), in which the count rate of individual visits were close to the XRT detection limit ( $\sim 10^{-3}$  count  $s^{-1}$ ) we stack few observations using the ‘dynamical binning’ as described in Evans et al. (2007), in order to obtain a smooth X-ray light curve.

The short XRT exposures do not allow for spectral fitting of individual visits, so we stacked consecutive observations using an automated online tool<sup>3</sup> (Evans et al. 2009). We aimed to have at least 100 counts per stacked spectrum, allowing the bins to be at maximum 100

<sup>1</sup> For the standard 2 ks observations this translate to a 0.3-10 keV flux greater than  $few \times 10^{-13}$  erg  $\text{cm}^{-2}$   $s^{-1}$

<sup>2</sup> <https://www.cosmos.esa.int/web/xmm-newton/sas-thread-epatplot>

<sup>3</sup> [https://www.swift.ac.uk/user\\_objects](https://www.swift.ac.uk/user_objects)

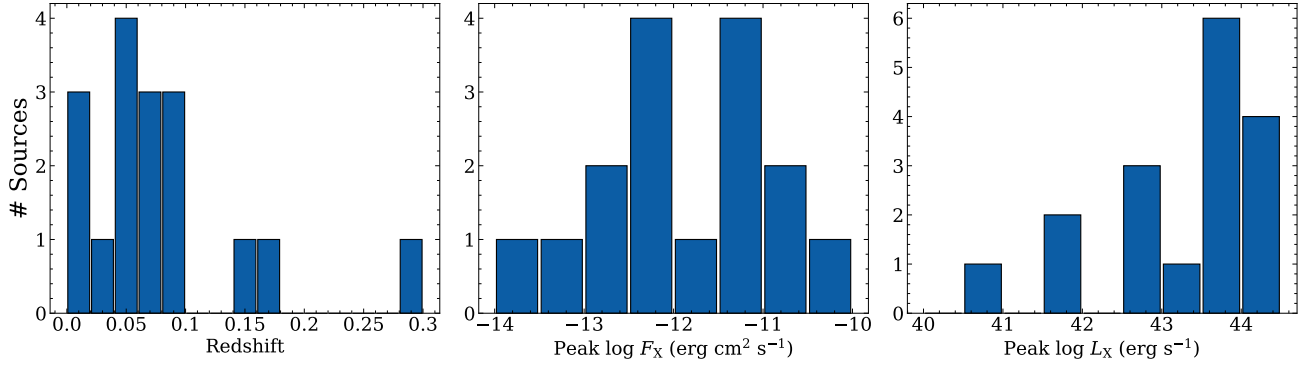


**Figure 1.** Histogram of the distributions of the properties of our main sample. Redshift ( $z$ , left), neutral absorption corrected peak 0.3-10 keV X-ray flux ( $F_X$ , middle), neutral absorption corrected peak 0.3-10 keV X-ray luminosity ( $L_X$ , right).

**Table 1.** Sample Information.

IAU	Discovery	Optical/UV peak	Redshift	$N_{H,G}$	$\log(M_*/M_\odot)^b$	$\sigma_*$	$\log(M_{\text{BH}}/M_\odot)^c$	TDE
Name	Name	(MJD)		( $10^{20} \text{ cm}^{-2}$ ) <sup>a</sup>		( $\text{km s}^{-1}$ )		Classification
AT2018zr	ZTF18aabtxvd	58214	0.071	4.17	$10.01^{+0.08}_{-0.14}$	$49 \pm 5^{(d)}$	$5.83 \pm 0.51$	ATel #11444
AT2018hyz	ASASSN-18zj	58422	0.045	2.59	$9.96^{+0.09}_{-0.16}$	$57 \pm 1^{(e)}$	$6.12 \pm 0.46$	ATel #12198
AT2019azh	ASASSN-19dj	58558	0.022	4.15	$9.74^{+0.08}_{-0.05}$	$77 \pm 2^{(f)}$	$6.68 \pm 0.46$	ATel #12568
AT2019dsg	ZTF19aapreis	58600	0.051	6.46	$10.55^{+0.09}_{-0.12}$	$94 \pm 1^{(g)}$	$7.04 \pm 0.45$	ATel #12752
AT2019ehz	Gaia19bpt	58611	0.074	1.42	$9.65^{+0.09}_{-0.12}$	$47 \pm 11^{(d)}$	$5.75 \pm 0.59$	ATel #12789
AT2019qiz	ZTF19abzrhgq	58764	0.015	6.35	$10.01^{+0.09}_{-0.12}$	$70 \pm 2^{(h)}$	$6.49 \pm 0.46$	ATel #13131
AT2019teq	ZTF19accmaxo	58794	0.087	4.54	$9.95^{+0.07}_{-0.11}$	...	$6.32 \pm 0.49$	TNSCR #7482
AT2019vcb	ZTF19acspeuw	58838	0.088	1.45	$9.49^{+0.06}_{-0.06}$	...	$5.59 \pm 0.52$	TNSCR #7078
AT2020ddv	ZTF20aamqmfk	58915	0.16	1.35	$10.30^{+0.13}_{-0.16}$	$57 \pm 10^{(d)}$	$6.09 \pm 0.55$	ATel #13655
AT2020ksf	Gaia20cjk	58976	0.092	3.61	$10.12^{+0.13}_{-0.09}$	$52 \pm 2^{(i)}$	$5.92 \pm 0.48$	Gilfanov et al. (2020)
AT2020ocn	ZTF18aakelin	58972	0.07	1.28	$10.28^{+0.13}_{-0.70}$	$81 \pm 8^{(d)}$	$6.77 \pm 0.49$	ATel #13859
AT2021ehb	ZTF21aanxhvj	59330	0.018	9.88	$10.18^{+0.01}_{-0.02}$	$93 \pm 5^{(j)}$	$7.04 \pm 0.46$	TNSCR #10001
AT2021yzv	ZTF21abxngcz	59475	0.286	8.60	$10.65^{+0.04}_{-0.06}$	...	$7.45 \pm 0.47$	TNSCR #11890
...	ASASSN-14li	56993	0.02	1.95	$9.68^{+0.04}_{-0.09}$	$81 \pm 2^{(k)}$	$6.77 \pm 0.46$	ATEL #6777
...	ASASSN-15oi	57259	0.048	4.86	$10.02^{+0.04}_{-0.03}$	...	$6.42 \pm 0.48$	ATEL #7936
AT2018fyk	ASASSN-18sul	58389	0.059	1.16	$10.56^{+0.21}_{-0.12}$	$158 \pm 1^{(l)}$	$8.04 \pm 0.44$	TNSCR #2723
...	OGLE16aaa	57403	0.165	2.72	$10.47^{+0.09}_{-0.11}$	...	$7.14 \pm 0.48$	Wyrzykowski et al. (2017)
AT2018bsi	ZTF18aahqkbtr	58389	0.051	4.91	$10.62^{+0.05}_{-0.07}$	$118 \pm 8^{(d)}$	$7.48 \pm 0.46$	ATel #12035
AT2018hco	ATLAS18way	58479	0.088	4.12	$10.01^{+0.12}_{-0.16}$	...	$6.40 \pm 0.49$	ATel #12263
AT2018iih	ATLAS18yzs	58558	0.212	3.19	$10.81^{+0.11}_{-0.14}$	...	$7.70 \pm 0.48$	van Velzen et al. (2021)
AT2018lna	ZTF19aabbnzo	58561	0.091	6.42	$9.56^{+0.08}_{-0.14}$	$36 \pm 4^{(d)}$	$5.20 \pm 0.53$	ATel #12509
AT2019mha	ZTF19abhejal	58705	0.148	1.71	$10.01^{+0.14}_{-0.18}$	...	$6.41 \pm 0.49$	van Velzen et al. (2021)
AT2019meg	ZTF19abhhjcc	58743	0.152	5.08	$9.64^{+0.07}_{-0.08}$	...	$5.81 \pm 0.52$	AN-2019-88
AT2020pj	ZTF20aabqihu	58866	0.068	2.24	$10.01^{+0.07}_{-0.08}$	...	$6.43 \pm 0.49$	TNSCR #7481
AT2020vwl	ZTF20achpcvt	59167	0.032	2.23	$9.89^{+0.08}_{-0.08}$	...	$6.21 \pm 0.49$	TNSCR #8572
AT2020wey	ZTF20acitpfz	59156	0.027	6.19	$9.67^{+0.09}_{-0.12}$	$39 \pm 3^{(d)}$	$5.38 \pm 0.51$	TNSCR #7769

NOTE—Top: X-ray detected TDE (main sample). Bottom: X-ray non-detected TDEs with new deeper upper-limits. Abbreviations ATel corresponding to the Astronomer’s Telegram (<https://astronomerstelegam.org>), AN corresponding to AstroNotes (<https://www.wis-tns.org/astronotes>), and TNSCR corresponding to TNS classification reports. a) Galactic absorption column density from H4PI Collaboration et al. (2016); b) Host galaxy stellar mass from SED fitting (see 2.2.1); c) Black hole masses. When a  $\sigma_*$  measurement is available it is estimated using the Gültekin et al. (2019)  $\sigma_*-M_{\text{BH}}$  relation, when  $\sigma_*$  is not available, this is estimated from the  $M_*-M_{\text{BH}}$  relation presented in Yao et al. (2023b). d) Hammerstein et al. (2023b); e) Short et al. (2020); f) Liu et al. (2022); g) Cannizzaro et al. (2021); h) Nicholl et al. (2020); i) Wevers et al., in prep; j) Yao et al. (2022); k) Wevers et al. (2019b); l) Wevers et al. (2019a)

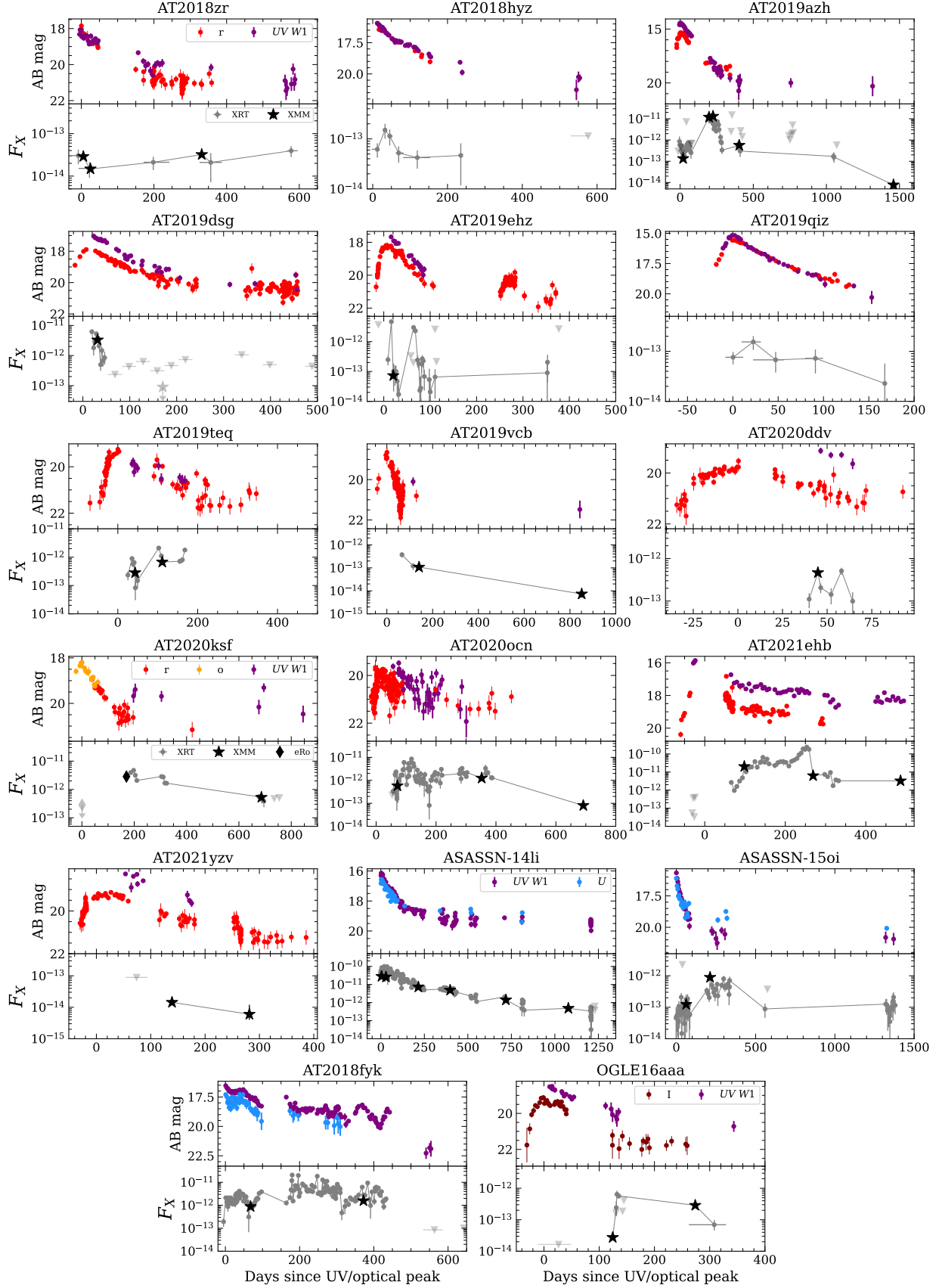


**Figure 2.** UV/Optical (top panels) and X-ray (bottom panels) light curves from our sample of 17 optically selected X-ray detected TDEs. On top panels we show ZTF  $r$ -band (red points), *Swift*/UVOT UV W1 band (purple points), ATLAS  $o$ -band (orange points) and OGLE  $I$ -band (maroon points), all in magnitudes in the AB system. On bottom panels we show the neutral absorption corrected 0.3-10 keV X-ray flux ( $F_X$ ), *Swift*/XRT in grey points, *XMM-Newton* in stars and *SRG/eROSITA* in diamonds.



days long, we also ensure there was no large evolution in the hardness ratio within each bin. For AT2018zr, AT2019vcb, AT2020ddv and ASASSN-15oi there were not enough counts to generate a fitable spectrum, even combining all the XRT observations, therefore we restrict our XRT analysis on their light curves and only perform spectral analysis in their *XMM-Newton* data, which will be described in detailed in §3.

We used the `uvotsource` package to analyze the Swift UVOT photometry, using an aperture of  $5''$  for all sources except AT2019azh, AT2019qiz, and AT2019dsg, which required a larger aperture to capture the host galaxy light. We subtracted the host galaxy flux estimated from the population synthesis modeling of archival pre-event photometry described in §2.2.1. We apply Galactic extinction correction on all bands using  $E(B - V)$  values at the position of each source from Schlafly & Finkbeiner (2011).

### 2.1.3. Zwicky Transient Facility

We performed point spread function (PSF) photometry on all publicly available ZTF data using the ZTF forced-photometry service (Masci et al. 2019, 2023) in  $g$ - and  $r$ -band. Similar to UVOT, ZTF photometry was corrected for Galactic extinction.

### 2.1.4. Additional Data

OGLE16aaa was discovered by the fourth phase of the Optical Gravitational Lensing Experiment (OGLE-IV, Udalski et al. 2015) survey, we added the I band (7970 Å) data, which is the best sampled optical light curve of the source; the data was retrieved from the survey website<sup>4</sup>.

The optical peak of AT2020ksf was missed by ZTF, however the Asteroid Terrestrial-impact Last Alert System (ATLAS, Tonry et al. 2018) started observing the field containing the source  $\sim 60$  days before ZTF, hence allowing us to measure the date of its optical peak; we added available ATLAS data to our light curve of AT2020ksf. The source was first detected in the X-rays by the *SRG/eROSITA*, although the spectral data is not yet publicly available, we added the reported detection flux of  $1.7 \times 10^{-12} \text{ erg cm}^{-2} \text{ s}^{-1}$  ( $2.85 \times 10^{-12} \text{ erg cm}^{-2} \text{ s}^{-1}$  unabsorbed) observed in 20th November 2020 (MJD 59162), as well as the previous X-ray upper limit ( $\leq 2.85 \times 10^{-13} \text{ erg cm}^{-2} \text{ s}^{-1}$ ) from a visit taken on 8th May 2020 (MJD 58977) which is fortuitously timed at

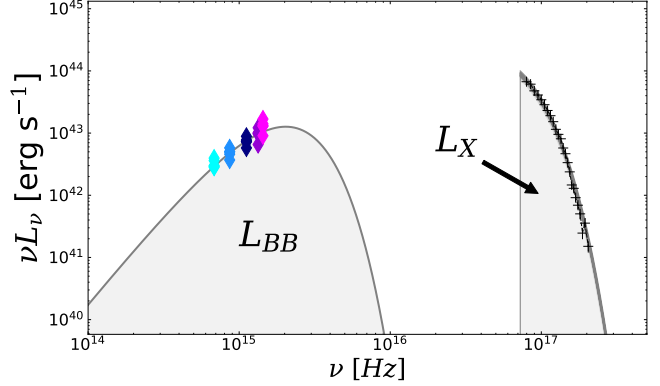


**Figure 3.** Illustration of how the UV/optical blackbody luminosity ( $L_{BB}$ ) and the 0.3-10 keV X-ray luminosity ( $L_X$ ) are measured and what those values represent regarding the full SED of the transient. Colored points indicate observed UV/optical photometry, underline it the best-fitting blackbody function is shown in dark gray, and the area below the curve is the measured  $L_{BB}$ . The black crosses show the observed X-ray spectra and best-fitted X-ray model, and the measured  $L_X$  is also shown in gray. Both UV/optical and X-ray components are corrected for Galactic extinction/absorption.

the optical peak of the source, both reported by Gilfanov et al. (2020).

## 2.2. UV/optical Data Analyses

### 2.2.1. Host Galaxy SED modeling

Before analyzing the transient’s UV/optical light curve, the host contamination needs to be subtracted. We followed van Velzen et al. (2021) prescription to fit the host galaxy pre-flare photometry. We compile the host galaxy spectral energy distribution (SED) using archival observations in the UV through IR bands. We use the *Prospector* software (Johnson et al. 2021) to run a Markov Chain Monte Carlo (MCMC) sampler (Foreman-Mackey et al. 2013) to obtain the posterior distributions of the Flexible Stellar Population Synthesis models (Conroy et al. 2009). We adopted a simple power law star formation history, with the same ranges and priors as in van Velzen et al. (2021), for the 5 free parameters: stellar mass, Calzetti et al. (2000) dust model optical depth, stellar population age, metallicity, and the e-folding time of the star formation history. The resulting host stellar mass ( $M_*$ ) are presented in Table 1, the fitting for all host galaxies of our sample are presented either in van Velzen et al. (2021), Hammerstein et al. (2023a) or Yao et al. (2023b), the reader is referred to these papers for the full list of best-fitting parameters. We subtract the host contribution to the transient’s UVOT filter’s photometry. The UV W1 band (2600 Å, observed frame) host-subtracted light curves

<sup>4</sup> <http://ogle.astrouw.edu.pl/ogle4/transients/2017a/transients.html>

**Table 2.** Summary of *XMM-Newton* Observations

Source	Obs ID	Obs Date	phase ( $\Delta t$ ) <sup>a</sup>	$\log F_X^b$	$\log L_X^b$	$L_{\text{BB}} / L_X$	First
		MJD	(days)	( $\text{erg cm}^2 \text{ s}^{-1}$ )	( $\text{erg s}^{-1}$ )		
AT2018zr	0822040301	58220	5	$-13.538^{+0.040}_{-0.045}$	$41.610^{+0.040}_{-0.045}$	$95.46^{+9.26}_{-9.30}$	van Velzen et al. (2019)
	0822040501	58241	25	$-13.831^{+0.052}_{-0.059}$	$41.317^{+0.052}_{-0.059}$	$127.48^{+16.28}_{-16.24}$	this work
	0822040401	58569	331	$-13.493^{+0.033}_{-0.036}$	$41.656^{+0.033}_{-0.036}$	$12.38^{+0.99}_{-1.00}$	
AT2019azh	0822041101	58579	20	$-12.872^{+0.016}_{-0.017}$	$41.178^{+0.016}_{-0.017}$	$889.10^{+34.07}_{-34.09}$	this work
	0842591001	58760	197	$-10.924^{+0.002}_{-0.002}$	$43.125^{+0.002}_{-0.002}$	$0.58^{+0.01}_{-0.01}$	
	0823810401	58788	225	$-10.881^{+0.001}_{-0.001}$	$43.168^{+0.001}_{-0.001}$	$0.41^{+0.01}_{-0.01}$	
	0842592601	58971	404	$-12.248^{+0.013}_{-0.014}$	$41.801^{+0.013}_{-0.014}$	$2.14^{+0.07}_{-0.07}$	
	0902761101	60049	1458	$-14.114^{+0.116}_{-0.158}$	$39.936^{+0.116}_{-0.158}$	...	
AT2019dsg	0842590901	58633	31	$-11.483^{+0.004}_{-0.004}$	$43.316^{+0.004}_{-0.004}$	$3.16^{+0.03}_{-0.03}$	Stein et al. (2021)
	0842591901	58779	170	$< -13.046$	$< 41.753$	$> 15.99$	
AT2019ehz	0842590801	58633	20	$-13.138^{+0.022}_{-0.023}$	$41.998^{+0.022}_{-0.023}$	$50.89^{+2.63}_{-2.63}$	this work
AT2019teq	0842591701	58841	43	$-12.549^{+0.011}_{-0.012}$	$42.736^{+0.011}_{-0.012}$	$2.25^{+0.06}_{-0.06}$	this work
	0842592401	58915	111	$-12.173^{+0.005}_{-0.006}$	$43.111^{+0.005}_{-0.006}$	$0.49^{+0.01}_{-0.01}$	
AT2019vcb	0871190301	58991	140	$-12.967^{+0.020}_{-0.106}$	$42.339^{+0.020}_{-0.106}$	$1.71^{+0.08}_{-0.08}$	Quintin et al. (2023)
	0882591401	59764	851	$-14.136^{+0.106}_{-0.150}$	$41.169^{+0.106}_{-0.150}$	$7.12^{+1.97}_{-2.08}$	this work
AT2020ddv	0842592501	58967	44	$-12.332^{+0.008}_{-0.008}$	$43.523^{+0.008}_{-0.008}$	$5.05^{+0.09}_{-0.09}$	this work
AT2020ksf	0882591201	59725	749	$-12.280^{+0.009}_{-0.010}$	$43.057^{+0.009}_{-0.010}$	$2.92^{+0.06}_{-0.06}$	this work
AT2020ocn	0863650101	59048	76	$-12.238^{+0.005}_{-0.006}$	$42.848^{+0.005}_{-0.006}$	$1.42^{+0.02}_{-0.02}$	Pasham et al. (2024)
	0872392901	59349	377	$-11.902^{+0.004}_{-0.004}$	$43.183^{+0.004}_{-0.004}$	$0.06^{+0.01}_{-0.01}$	this work
	0902760701	59712	685	$-13.094^{+0.020}_{-0.021}$	$41.991^{+0.020}_{-0.021}$	$2.73^{+0.13}_{-0.13}$	
AT2021ehb	0882590101	59430	98	$-10.696^{+0.003}_{-0.004}$	$43.177^{+0.003}_{-0.004}$	$0.49^{+0.01}_{-0.01}$	Yao et al. (2022)
	0882590901	59604	269	$-11.203^{+0.003}_{-0.003}$	$42.670^{+0.003}_{-0.003}$	$0.52^{+0.01}_{-0.01}$	this work
	0902760101	59825	486	$-11.489^{+0.006}_{-0.006}$	$42.384^{+0.006}_{-0.006}$	$0.67^{+0.01}_{-0.01}$	
AT2021yzv	0882591001	59654	139	$-13.844^{+0.054}_{-0.062}$	$42.580^{+0.054}_{-0.062}$	$99.26^{+13.22}_{-13.19}$	this work
	0882591501	59837	281	$-14.222^{+0.301}_{-0.176}$	$42.204^{+0.301}_{-0.176}$	$68.48^{+68.48}_{-22.83}$	
ASASSN-14li	0694651201	56997	3	$-10.549^{+0.002}_{-0.002}$	$43.442^{+0.002}_{-0.002}$	$2.33^{+0.01}_{-0.01}$	Miller et al. (2015)
	0694651401	57023	29	$-10.588^{+0.002}_{-0.002}$	$43.403^{+0.002}_{-0.002}$	$1.31^{+0.01}_{-0.01}$	Kara et al. (2018)
	0694651501	57213	215	$-11.135^{+0.004}_{-0.004}$	$42.856^{+0.004}_{-0.004}$	$0.78^{+0.01}_{-0.01}$	
	0770980501	57399	397	$-11.312^{+0.005}_{-0.005}$	$42.679^{+0.005}_{-0.005}$	$0.49^{+0.01}_{-0.01}$	Wen et al. (2020)
	0770980701	57726	718	$-11.855^{+0.007}_{-0.008}$	$42.136^{+0.007}_{-0.008}$	$2.04^{+0.04}_{-0.04}$	
ASASSN-15oi	0722160501	57324	62	$-12.907^{+0.027}_{-0.029}$	$41.837^{+0.027}_{-0.029}$	$77.94^{+5.07}_{-5.06}$	Gezari et al. (2017)
	0722160701	57482	212	$-12.051^{+0.011}_{-0.011}$	$42.693^{+0.011}_{-0.011}$	$1.22^{+0.03}_{-0.03}$	
AT2018fyk	0831790201	58461	67	$-12.056^{+0.005}_{-0.005}$	$42.874^{+0.005}_{-0.005}$	$29.62^{+0.31}_{-0.31}$	Wevers et al. (2021)
	0853980201	58783	372	$-11.803^{+0.003}_{-0.003}$	$43.127^{+0.003}_{-0.003}$	$2.97^{+0.02}_{-0.02}$	
OGLE16aaa	0790181801	57548	124	$-13.563^{+0.056}_{-0.064}$	$42.322^{+0.056}_{-0.064}$	$15.06^{+2.06}_{-2.06}$	Kajava et al. (2020)
	0793183201	57722	273	$-12.543^{+0.012}_{-0.012}$	$43.342^{+0.012}_{-0.012}$	$0.49^{+0.01}_{-0.01}$	
AT2018bsi	0822040801	58389	164	$< -13.453$	$< 41.319$	$> 42$	this work
AT2018hco	0822040901	58479	71	$< -13.974$	$< 41.312$	$> 291$	this work
AT2018iih	0822040701	58558	95	$< -14.250$	$< 41.867$	$> 254$	this work
AT2018lna	0822041001	58561	48	$< -14.057$	$< 41.260$	$> 309$	this work
AT2019mha	0842592201	58705	33	$< -14.288$	$< 41.483$	$> 43$	this work
AT2019meg	0842592101	58743	40	$< -13.919$	$< 41.878$	$> 82$	this work
AT2020wey	0902760401	59851	676	$< -13.0857$	$< 41.1449$	... <sup>c</sup>	this work
AT2020pj	0902760801	59809	882	$< -13.5102$	$< 41.5488$	... <sup>c</sup>	this work
AT2020vwl	0902760301	59776	590	$< -13.568$	$< 40.8932$	... <sup>c</sup>	this work

NOTE—a) Relative to the rest-frame UV/optical peak; b) 0.3-10.0 keV band, upper limits are  $3\sigma$ . c) No simultaneous UV/optical detections available.

are shown in the top panels of Figure 2 for individual sources.

### 2.2.2. UV/optical light curves

Following the standard approach for optical TDEs (e.g., van Velzen et al. 2021; Hammerstein et al. 2023a) we estimate the integrated UV/optical luminosity ( $L_{BB}$ ) by fitting the transient UV/optical SED with an evolving, Gaussian rise and power law decay, blackbody (BB) function. The model can be written as:

$$L_{BB}(t) = L_{BB,peak} \frac{\pi B_\nu(T(t))}{\sigma_{SB} T^4(t)} \times \begin{cases} e^{-(t-t_{peak})^2/2\sigma^2}, & t \leq t_{peak} \\ [(t-t_{peak})/t_0]^p, & t > t_{peak} \end{cases} \quad (1)$$

We consider a non-parametric temperature evolution; we fit the temperature at grid points spaced  $\pm 30$  days apart beginning at peak and use a log-normal Gaussian prior at each grid point. We use a Gaussian likelihood function to estimate the parameters of the models above; we use the `emcee` sampler (Foreman-Mackey et al. 2013). Details on the fitting process and resulting UV/optical integrated light curves can be seen in either van Velzen et al. (2021) or Hammerstein et al. (2023a) for all the sources. The time dependent model assumed in Eq. 1, was assumed for the first 350 days of the optical light curve, after that the light curve shape usually deviates from the power-law decay (van Velzen et al. 2021; Hammerstein et al. 2023a). For the later epochs, we measured the integrated UV/optical luminosity by fitting again with a blackbody function for the available UV/optical photometry data, epoch by epoch, when  $L_{BB}$  measurements were necessary (see §4). In Fig. 3, we illustrate what fitting a blackbody to the UV/optical broad-band photometric data means in terms of the full SED of the transient; it also illustrates how misleading it can be to interpret  $L_{BB}$  as a ‘bolometric’ luminosity, as is commonly done by some authors; such aspects will be further explored in §4.4.

### 2.3. Black Hole Masses

The black holes masses ( $M_{BH}$ ) of the TDE hosts were estimated from the host galaxy scaling relations. If a measurement of the velocity dispersion ( $\sigma_*$ ) of their nuclear stellar populations were publicly available (e.g., Wevers et al. 2019b; Yao et al. 2023b; Hammerstein et al. 2023b)  $M_{BH}$  was estimated from  $\sigma_*-M_{BH}$  relation by Gültekin et al. (2019). Alternatively, if  $\sigma_*$  was not available,  $M_{BH}$  was estimated from the host galaxy mass ( $M_*$ , as measured from 2.2.1) using the relation

presented in Yao et al. 2023b. The  $\sigma_*$ ,  $M_*$  and  $M_{BH}$  values are shown in Table 1. Uncertainties in  $M_{BH}$  are the result of the addition in quadrature of the statistical uncertainty of  $\sigma_*/M_*$  and the systematic spread of the scaling relations, and are usually  $\sim 0.5$  dex.

## 3. X-RAY SPECTRAL FITTING

The following procedures were performed using the python version of `xspec` (Arnaud 1996), `pyxspect`<sup>5</sup>. For all spectral models described below, we included the Galactic absorption using the `TBabs` model (Wilms et al. 2000), with the hydrogen-equivalent neutral column density  $N_{H,G}$  fixed at the values shown in Table 2 (HI4PI Collaboration et al. 2016). We shifted the TDE emission using the convolution model `zshift`, with the redshift  $z$  shown in Table 1. *XMM-Newton* spectra were grouped to have at least 25 counts per bin, but limiting the over-sampling of the instrumental resolution to a factor of 5; we assume a  $\chi^2$ -statistic. For *Swift*/XRT data fitting, the stacked spectra were grouped to have at least 1 count per bin; we assume a C-statistic (Cash 1979). To convert the count rate of each visit to flux, we assume the closest in time best-fit model to the stacked spectra. We check for the convergence of the fitting using the `steppar` command in `xspec`.

### 3.1. General Spectral Properties

The most distinct characteristic property of the X-ray spectra of TDEs is its softness – a visual inspection of our *XMM-Newton* observations confirms this trend for our optically detected X-ray bright TDEs sample – this makes TDE X-ray spectra clearly distinguishable from the dominant sources of extragalactic X-ray emission from AGN. While AGN usually emits from the soft X-ray up to the hard X-rays ( $E \gg 10$  keV), with a non-thermal (power-law) spectrum, TDEs rarely show emission at energies higher than 2.0 keV.

To demonstrate this, we compare the X-ray spectral properties of our TDE sample with the X-ray properties of the non-blazar Type I and Type II of the BAT AGN Spectroscopic Survey (BASS, Ricci et al. 2017). Details on how the BASS comparison sample was retrieved is described in appendix §C. In the left panels of Fig. 4 we compare the model independent – but instrument dependent – hardness ratio (HR) of the samples, which is defined as  $HR = (H - S)/(H + S)$ , where  $S$  is the 0.3-2.0 keV count rate and  $H$  is the 2.0-10.0 keV count. Our entire TDEs sample has  $HR \leq -0.5$ , with 85% having  $HR \leq -0.80$ . The Type I AGN sample is concentrated

<sup>5</sup> <https://heasarc.gsfc.nasa.gov/xanadu/xspec/python>



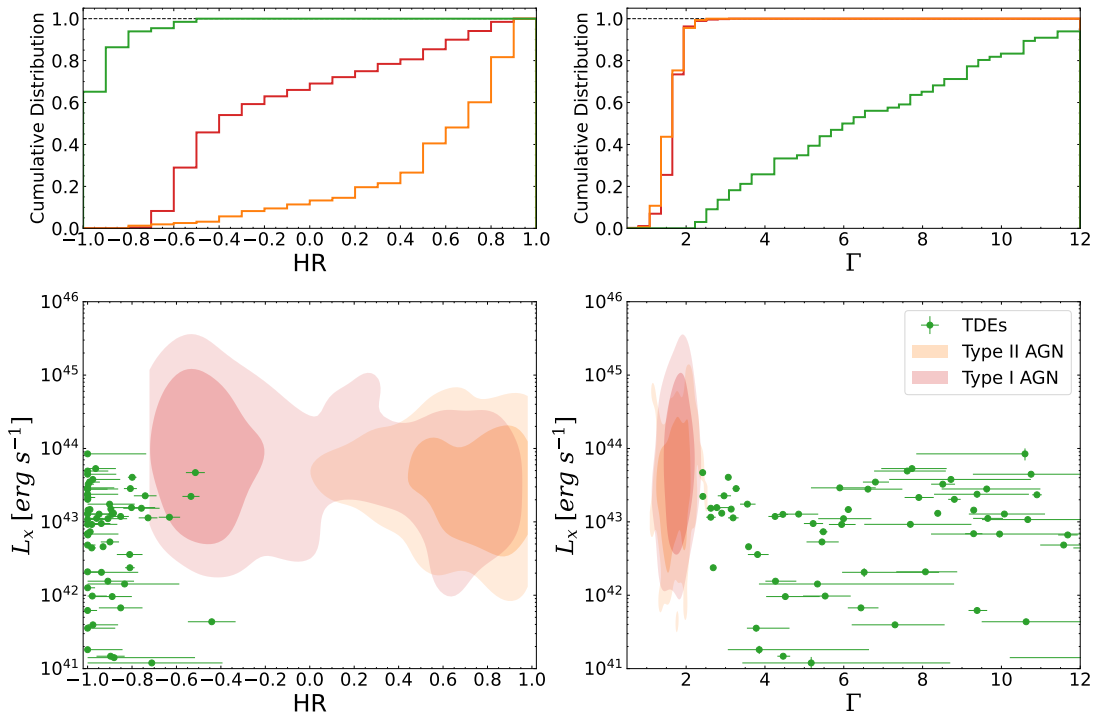


**Figure 4.** Comparison between X-ray spectral properties of TDEs (green) and AGN (Type I in red and Type II in gold) from the BAT AGN Spectroscopic Survey (BASS, Ricci et al. 2017). In the left panels we compare the *Swift*/XRT or *XMM-Newton* hardness ratio (HR, see text for definition), in the right panels we compare the  $\Gamma$  power-law index when TDEs are fitted with an absorbed power-law model. The top panels show the cumulative distribution of the parameters, while the bottom panels show the distribution of samples in the  $L_X$  vs. HR and  $L_X$  vs.  $\Gamma$  parameter space. For AGNs the contours represent 68% and 90% of the sample distribution, for TDEs each point is a *XMM-Newton* or *Swift*/XRT stacked spectrum.

between  $-0.7 \leq \text{HR} \leq 0.0$ , while the increased column density ( $N_H$ ) in obscured type II AGN makes their HR to range from 0.0 to 1.0. Such HR is dependent on the X-ray instrument response, these values are valid for *Swift*/XRT and/or *XMM-Newton*, which have similar relative soft-to-hard sensibility.

### 3.2. Absorbed Power-law Model

In AGN the main X-ray emission originates from the ubiquitous corona, and it is usually fitted with a phenomenological powerlaw model. Fitting TDE’s extremely soft spectra with an absorbed power-law (i.e. `TBabs*zashift*(TBabs*powerlaw)` in `xspec`) like in AGN, usually results in best-fitted  $\Gamma$  parameter higher than 5; such high values are nonphysical in the case of inverse up-scattering of seed photons by a hot corona (Titarchuk & Lyubarskij 1995) and hence do not represent any meaningful physical measurement.

Nevertheless, fitting with powerlaw may be useful to differentiate X-ray TDE spectra from AGN ones. In the right panels of Fig. 4, we compare the photon index  $\Gamma$  with those of AGN from the BASS comparison sample. In AGN, both Type I and Type II,  $\Gamma$  only varies between  $\sim 1.0$  and 2.5, while in TDEs these are much steeper, with  $\Gamma \in (2, 12)$ . The large uncertainties in the

spectra with  $\Gamma \geq 4$  is not due to low S/N, instead by the inadequacy of the absorbed power-law to described TDE spectra, and the large degeneracy between the intrinsic  $N_H$  and  $\Gamma$ , when a power-law model is fitted in a underlying thermal/soft spectra, epochs/spectra with  $\Gamma \leq 4$  are those in which corona formation is observed (see §4.3).

In summary, an absorbed powerlaw model is an inappropriate model for the emission of non-jetted TDEs, usually no physical interpretation can be derived from such fit, however, it still may be a good tool to differentiate (when more information is lack) TDEs from AGN, as clearly demonstrate by Fig. 4.

### 3.3. Blackbody Model

TDE soft spectra can be fitted with thermal models, in their simplest form, a single temperature blackbody (`blackbody` or `bbbodyrad`, in `xspec`), has been used for some of the first X-ray discovered TDEs (see review by Saxton et al. 2020). We employed such model in our data (`TBabs*zashift*bbbodyrad` in `xspec`), the model fits well spectra with low signal-to-noise ratio (S/N). However, the model seems to be insufficient to fit spectra of high count rate observations, in which the model results in systematically worse fit (in terms of reduced  $\chi^2$ )

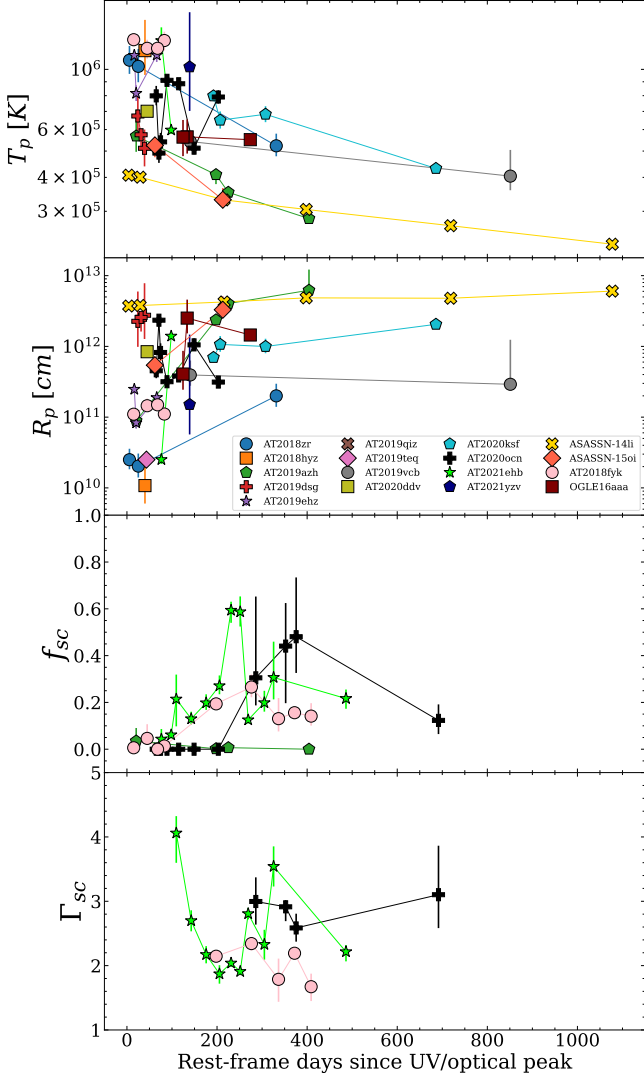


**Figure 5.** Best-fitting parameters from X-ray spectral modeling as function of time from the UV/optical peak. From top to bottom: Peak temperature ( $T_p$ ) and Radius ( $R_p$ ) from `tdediscspec`; fraction of comptonized photons ( $f_{sc}$ ) and power-law photon index ( $\Gamma_{sc}$ ) of `simPL`.

than multi-temperature thermal models, which are usually associated with a standard accretion disk (Shakura & Sunyaev 1973; Mitsuda et al. 1984; Mummery 2021, see below). Furthermore, as shown by Mummery (2021), `bbbodyrad` can lead to unphysical emitting regions sizes.

### 3.4. Accretion Disk + Comptonization Model

In terms of multi-temperature thermal models, the `diskbb` model (Shakura & Sunyaev 1973; Mitsuda et al. 1984) developed for stellar black holes in X-ray binaries (XRB) is usually employed in TDE spectra. The model, however, assumes quasi-static state condition which are not necessarily present in the newly form accretion disk of TDEs.

Recently, Mummery (2021) developed a model specifically tailored for TDE accretion disks; the author based their modeling on the convenient property of TDE disks being relatively cool, with their spectra peaking below the low bandpass of X-ray telescopes,  $kT \leq 0.3$  keV. This means that X-ray observations of TDE disks probe the quasi-Wien tail of the disk spectrum; hence no assumption about the disk temperature profile needs to be made; instead, the only assumption inherent to the model is that each disk radius emits like a color-corrected blackbody and that there exists some disk radius where the disk temperature peaks. The `xspec` model, called `tdediscspec`, fits the following expression to the observed X-ray spectra (Mummery 2021; Mummery & Balbus 2021):

$$F_\nu(R_p, \tilde{T}_p, \gamma) \simeq \frac{4\pi\xi_1 h\nu^3}{c^2 f_{\text{col}}^4} \left(\frac{R_p}{D}\right)^2 \left(\frac{k\tilde{T}_p}{h\nu}\right)^\gamma \exp\left(-\frac{h\nu}{k\tilde{T}_p}\right) \quad (2)$$

where  $\tilde{T}_p \equiv f_{\text{col}} f_\gamma T_p$ , and  $T_p$  is the parameter of interest, i.e., the hottest temperature in the accretion disc. The factor  $f_\gamma$  is the photon energy-shift factor, defined as the ratio of the observed photon frequency  $\nu$  to the emitted photon frequency  $\nu_{\text{emit}}$ ,  $f_\gamma = \nu/\nu_{\text{emit}} \approx 1/\sqrt{2}$  (see Mummery & Balbus 2021, and reference therein for details), while  $f_{\text{col}}$  is the ‘color-correction’ factor, which is included to model disk opacity effects. This correction factor generally takes a value  $f_{\text{col}} \sim 2.3$  for typical TDE disk temperatures (Done et al. 2012; Mummery 2021; Mummery et al. 2023), which is the value assumed in the `tdediscspec` model. The radius  $R_p$  is a normalization parameter that corresponds to radius of the hottest region. The constant  $\gamma$  depends on assumptions about both the inclination angle of the disk and the disk’s inner boundary condition and is limited to the range  $1/2 \leq \gamma \leq 3/2$ . The properties of  $\gamma$  are discussed in more detail in Mummery (2021) and references therein. In practice, the observed accretion disk spectrum is only weakly dependent on  $\gamma$ , which cannot be strongly constrained from observations (Mummery 2021). In this model,  $\gamma$  is therefore treated as a nuisance parameter, letting it vary between its allowed limits for each source. In fact, the  $1\text{-}\sigma$  uncertainties on  $\gamma$  typically fill the entire permitted range, and as such, the  $\gamma$  parameter merely extends the uncertainty range of the parameters  $T_p$  and  $R_p$ .

We fit our spectra with `TBabs` $\times$ `zshift`  $\times$  `tdediscspec`, the model shows both better fitting quality in terms of fitting statistics (see Table 7 and Fig. 24) as well as physical interpretation of the derived

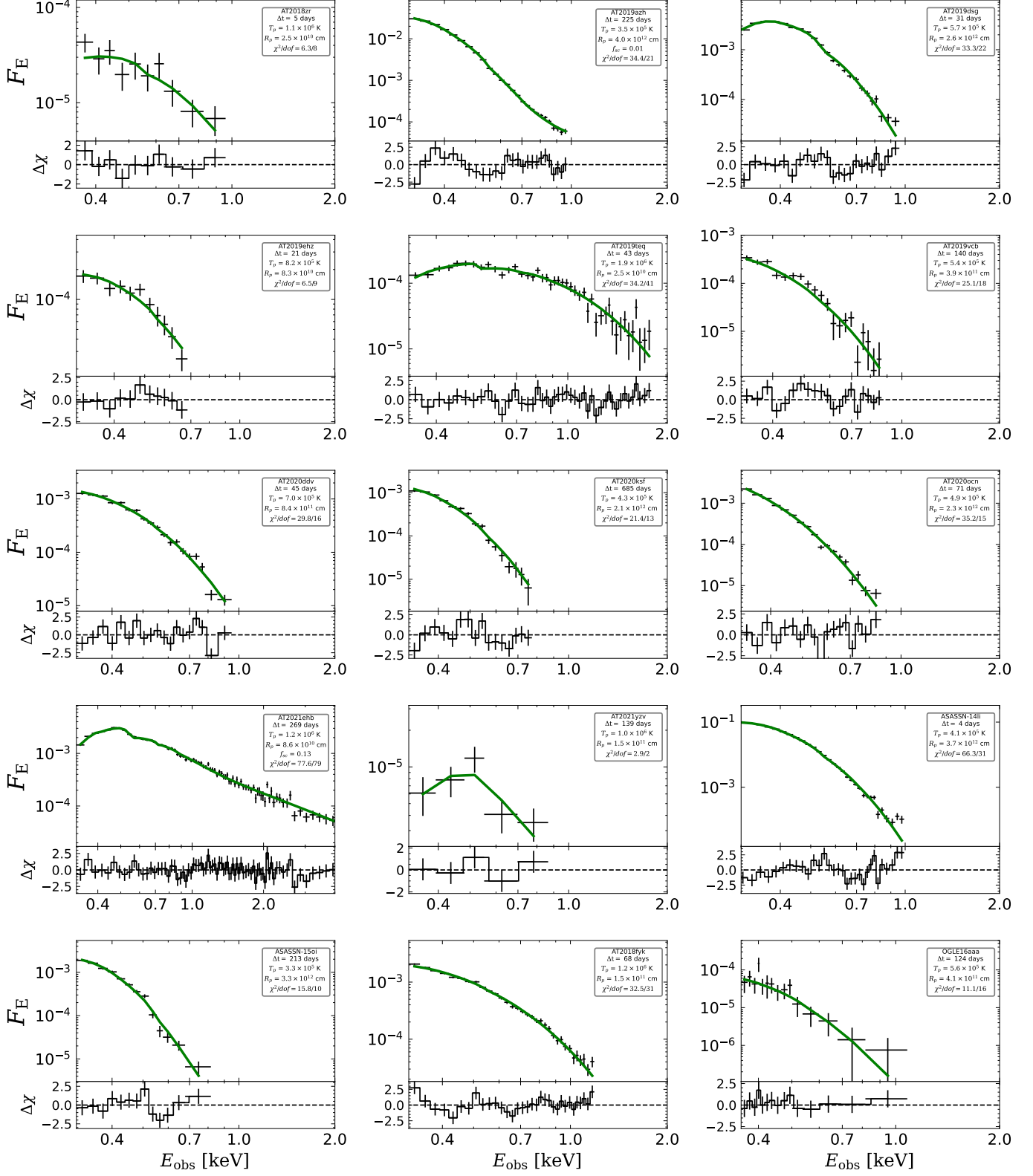


**Figure 6.** Representative unfolded spectra, best-fit model and residuals for all the source with available *XMM-Newton* data in our sample. Top panels shows the unfolded spectra in black and the best-fitting model in green (either `tdediscspec` or `simPL@tdediscspec`) in units of  $\text{keV cm}^{-2} \text{s}^{-1} \text{keV}^{-1}$ . Bottom panels show the residuals in  $\Delta\chi$ .

parameters, as compared to the aforementioned models, we hence adopted it as our main model for the soft component in TDEs.

For several sources/epochs, when fitted only with a soft component, a large residual at higher energies is present. Such a ‘hard excess’ is well described by a power-law function and was already reported for both X-ray (e.g., Saxton et al. 2017) and optically selected TDEs (e.g., Wevers et al. 2021; Yao et al. 2022), and is associated with Compton up-scattering of the soft photons by a corona of hot electrons near the accretion disk (Titarchuk & Lyubarskij 1995).

In AGN, this component is the dominant component of their X-ray spectra and is modeled with a phenomenological model ( $F(E) \propto E^{-\Gamma}$ , `powerlaw` in `xspec`). However, for soft and intermediate state XRBs, which in contrast to AGN and similar to TDEs, have both their main continuum and the power-law in the X-ray band, a more physically motivated and self-consistent model was developed by Steiner et al. (2009) to describe the Comptonization process, called `simPL` in `xspec`. The model has two free parameters,  $f_{sc}$ <sup>6</sup> and  $\Gamma_{sc}$ <sup>7</sup>; the first is the fraction of photons from the soft component that are up-scattered to create the power-law, and the second is the photon index of the resulting power-law. A more detailed discussion on using `simPL` on X-ray TDE spectra is presented in Appendix §A.

We employ the models described above, either `tdediscspec` or `simPL`⊗`tdediscspec`, depending on the need for the ‘hard tail’, based on a simple  $\chi^2/d.o.f$  analysis. Therefore, our X-ray modeling has either two free parameters ( $T_p$  and  $R_p$ ), if fitted only with `tdediscspec`, or four free parameters ( $T_p$ ,  $R_p$ ,  $f_{sc}$  and  $\Gamma_{sc}$ ) if fitted with `simPL`⊗`tdediscspec`. We also check whether an additional intrinsic neutral absorption was necessary by adding a `zTBabs` component to the model. Only for ASASSN-14li and AT2019dsg,  $N_H$ ’s of respectively  $\sim 5 \times 10^{20} \text{ cm}^{-2}$  and  $\sim 3 \times 10^{20} \text{ cm}^{-2}$ , significantly improve the residuals at the most soft energies, and were added to the final model. For all other sources the intrinsic absorption component was negligible to the fit quality which constrained their intrinsic  $N_H$  to be  $\ll 10^{20} \text{ cm}^{-2}$ .

<sup>6</sup> This should not be confused with the fractional flux of the power-law with respect to the total flux, at  $f_{sc} \sim 0.3$  the total flux is already dominated by the powerlaw component as shown in §A.

<sup>7</sup> We will use  $\Gamma_{sc}$  for the power-law photon index when the TDE X-ray spectra are fitted with `simPL`⊗`tdediscspec`, and  $\Gamma$  when the spectra are fitted with `powerlaw` model.

The stacked *Swift*/XRT spectrum of AT2019qiz and the second *XMM-Newton* epoch of AT2019teq show a divergent degeneracy between some of the model parameters, hence no uncertainties on the parameters could be determined and therefore no interpretation of the derived best-fitting parameters will be done, although we use the best-fitted parameters to scale the count-rates to flux/luminosity. The measured temperature of second epoch of AT2019teq is hotter than the  $T_p$  maximum limit on quasi-Wien approximation of `tdediscspec`, similarly no physical interpretation is attributed from the derived physical parameter of this epoch.

In Fig. 5, we show the best-fit value and its evolution for all four parameters in our modeling. A representative *XMM-Newton* observation and modeled spectra, as well as residuals for each source, are shown in Fig. 6. In Table 3 we summarize the spectral fitting procedures and models describe in this section.

Our final continuum models fit very well the continuum of most observations ( $\chi^2/d.o.f \sim 1.0$ ). However, some sources present features that resemble absorption lines, usually associated with O VII ( $\sim 0.54 \text{ keV}$ ) and/or O VIII ( $\sim 0.65 \text{ keV}$ ); these can be highly blueshifted (up to  $0.2c$ ) and interpreted as ultra fast outflows (UFO, e.g., Kara et al. 2018). We will explore these absorption lines’ detection, physical interpretation, and modeling in separate publications for those sources in which the statistical significance of the absorption detection can be assured.

#### 4. RESULTS

In Fig. 5, we show the best-fitting parameters from the X-ray spectral fitting, first the main parameters of `tdediscspec`, the peak temperature ( $T_p$ ) and apparent radius in which  $T_p$  occurs ( $R_p$ ), and for the power-law component (`simPL`), the fraction of the comptonized photons ( $f_{sc}$ ) and the photon index of the power-law ( $\Gamma_{sc}$ ), the later is only shown for three sources (AT2018fyk, AT2020ocn, AT2021ehb) in which a strong enough power-law is detected at some epoch (i.e.,  $f_{sc} \geq 0.1$ ), given the high uncertainty in  $\Gamma_{sc}$  when the component is only marginally detected. We also do not show the measurements of  $T_p$  and  $R_p$  for the epochs in which  $f_{sc} \geq 0.2$  given that the power-law emission completely dominates the spectra; hence no trustworthy information on the underline thermal emission can be recovered, as discussed in §A.

In Fig. 7, we show in left panels the neutral absorption corrected 0.3-10 keV luminosity ( $L_X$ ) and in the right panels the ratio ( $L_{BB}/L_X$ ) between the UV/optical integrated luminosity ( $L_{BB}$ , Eq. 1) and  $L_X$ , for the light curves of all the sources, as classified below.

**Table 3.** Summary of X-ray spectral modeling described in §3.

Model	XSPEC <sup>a</sup>	Free Parameters	Notes
Absorbed power-law	TBabs × powerlaw	$N_H, \Gamma, \text{norm}$	<ul style="list-style-type: none"> <li>• Inappropriate model for X-ray emission of non-jetted TDEs</li> <li>• Overestimate intrinsic <math>N_H</math></li> <li>• It can be used to differentiate the emission of AGN and TDEs (See Fig. 4)</li> </ul>
Single Temperature Blackbody	bodyrad	$T, R$	<ul style="list-style-type: none"> <li>• Better fit than absorbed power-law</li> <li>• Good fit for low S/N spectra</li> <li>• Leave significant residuals for high S/N spectra</li> </ul>
Accretion Disk	tdediscspec <sup>b</sup>	$T_p, R_p$	<ul style="list-style-type: none"> <li>• Good fit for most sources</li> <li>• <b>Final model<sup>c</sup> for source with no ‘hard excess’</b></li> <li>• Leaves residuals at high energies for source with some hard emission</li> </ul>
Accretion Disk + Comptonization	simPL ⊗ tdediscspec <sup>c</sup>	$T_p, R_p, f_{sc}, \Gamma_{sc}$	<ul style="list-style-type: none"> <li>• Accounts for comptonization of a fraction of disk’s photons</li> <li>• <b>Final model<sup>c</sup> for source with ‘hard excess’</b></li> </ul>

NOTE—a) All models were preceded by TBabs×zashift×. b) tdediscspec has an additional nuance parameter  $\gamma$ , see text for discussion. c) We also check whether an additional intrinsic neutral absorption was necessary by adding a zTBabs component to the model. Only for ASASSN-14li and AT2019dsg it significantly improve the fit, hence added to the final model. For all other sources, the intrinsic neutral absorption component was negligible.

#### 4.1. Diversity of X-ray Light Curves

A surprising characteristic of optically discovered X-ray bright TDEs – first observed in ASASSN-15oi by Gezari et al. (2017) – is that their X-ray light curve does not necessarily follow the theoretically expected fallback rate ( $\propto t^{-5/3}$ , Rees 1988), not even a more general lower-law decay ( $\propto t^{-\alpha}$ ), which is now established as the general evolution of their optical component (Hammerstein et al. 2023a). Instead, a wide diversity of time evolution and luminosity ranges are observed, in extreme contrast with some predictions, for example those by Lodato & Rossi (2011). This diversity also means that the time evolution of the ratio between the UV/optical and X-ray components also evolves in distinct ways in different sources. To search for a general picture of such diversity, we classified the sources in groups with similar evolution in terms of  $L_X$  and  $L_{BB}/L_X$ ; in Fig. 7, we show from top to bottom panels the following classes:

*Power-law Decaying* – ASASSN-14li, AT2019dsg and AT2019cvb are the only three source to show prompt bright ( $L_X \geq 10^{43}$  erg s<sup>-1</sup>) X-ray emission during the optical peak. The three sources show a power-law-like decay X-ray light curve, although the decay rate of the X-ray light curve in AT2019dsg is much higher than ASASSN-14li and AT2019cvb. Given the X-ray behavior, their  $L_{BB}/L_X$  do not show much variability staying in the  $0.5 \leq L_{BB}/L_X \leq 10$  range during the entire evolution of the sources.

*Late-time Brightening* – Most sources in our sample show a  $L_{BB}/L_X \gg 100$  near the optical peak, usually resulting from the faint X-ray emission ( $L_X \leq 10^{42}$  erg s<sup>-1</sup>) at early times. However, between 100-200 days after the optical peak, they show a significant brightening (more than an order of magnitude,  $L_X \geq 10^{43}$  erg s<sup>-1</sup>) in the X-rays, simultaneously to the UV/optical dimming and plateau, consequently  $L_{BB}/L_X$  tends to approach  $\sim 1$ .

*X-ray Faint* – AT2018zr, AT2018hyz, and AT2019qiz also show  $L_{BB}/L_X \gg 100$  near the optical peak, again resulting from the faint X-ray emission ( $L_X \leq 10^{42}$  erg s<sup>-1</sup>) at early times. However, the three sources never show a bright X-ray phase, although similar with previous classes their  $L_{BB}/L_X$  values also decrease with time.

*Flaring* – AT2019ehz show a unique behavior, the X-ray light curve show flares of almost two orders of magnitudes, from  $L_X \sim \text{few} \times 10^{41}$  erg s<sup>-1</sup> up to  $L_X \sim \text{few} \times 10^{43}$  erg s<sup>-1</sup> in a short scale of tens of days, while the  $L_{BB}$  show a standard smoothly evolution.

We could fit 13 of our 17 sources in these four classes; however, for the remaining sources, we do not have enough time coverage to assign them to one of these classes of X-ray evolution, either lack of sampling (AT2021yzv), lack of long-term follow-up (AT2019vcb and AT2020ddv), or lack of observations within the first 50 days from the optical peak (AT2022ocn). The later being fundamental to access whether the prompt bright X-ray emission is present or not.



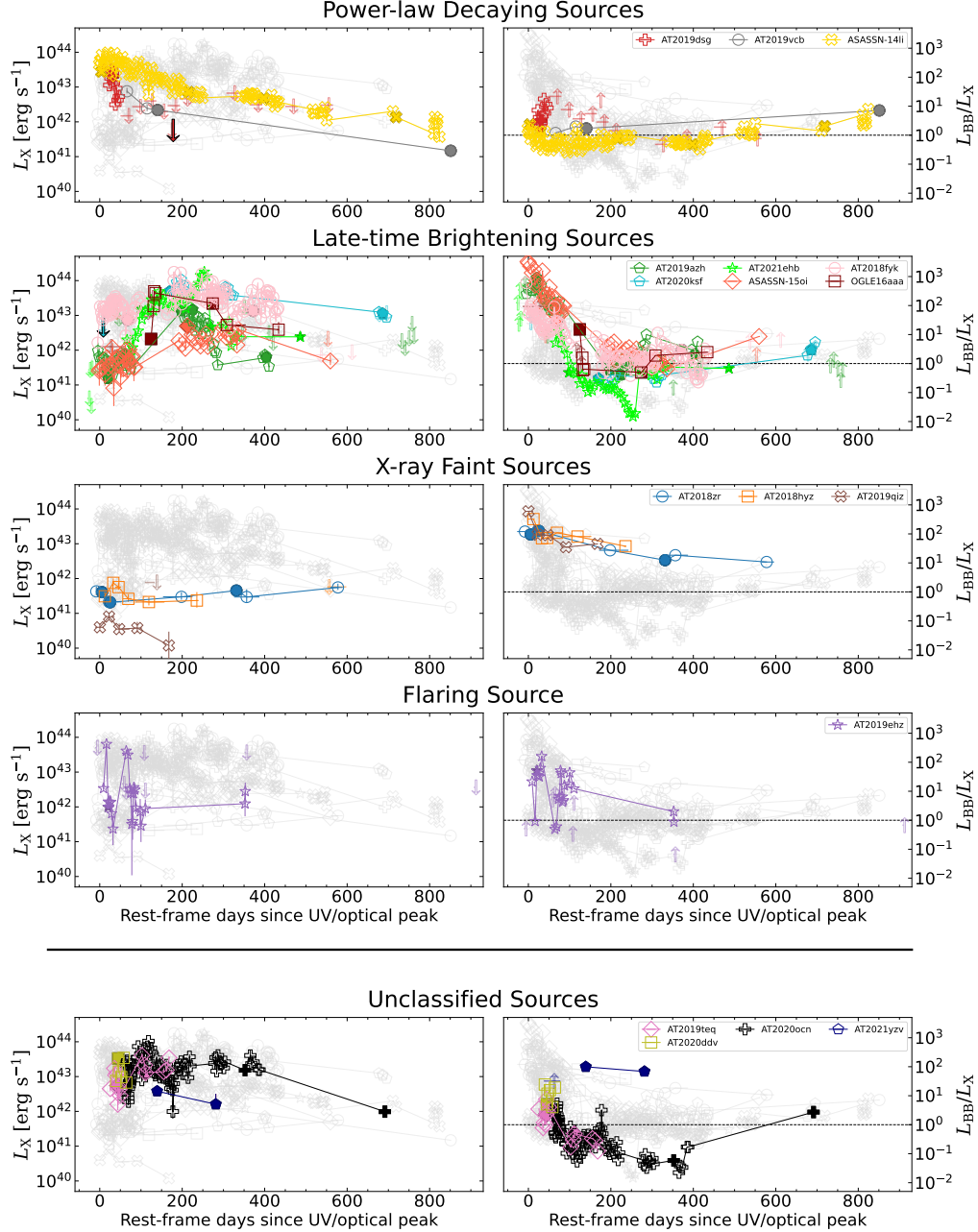


**Figure 7.** Left: The 0.3-10 X-ray luminosity ( $L_X$ ). Right: ratio of UV/optical blackbody luminosity to X-ray luminosity ( $L_{BB}/L_X$ ), grey dotted line shows  $L_{BB} = L_X$ . Top to Bottom panels show the different classes of X-ray evolution as described in §4.1.

#### 4.2. Temperature and Radius Evolution

In this section, we explore the evolution of the temperature ( $T_p$ ) and radius ( $R_p$ ) derived from the X-ray continuum fitting (`tbabspec`); we focus our analyses in the sources with higher temporal coverage in which some assessments on the long-term evolution of the derived parameters can be made. Due to the degeneracy between  $f_{sc}$  and  $T_p$ , at high values of  $f_{sc}$ , and the underline thermal can not be uniquely recovered (see §A), we exclude the sources with strong corona formation (i.e.,

$f_{sc} \geq 0.1$ ) from this analyses, these sources will be separately discussed in §4.3.

The temporal evolution of  $T_p$  is shown in Fig. 8; the cooling of the X-ray continuum is clearly observed: most sources show a peak X-ray temperature at their first available spectra, i.e., the closest to the peak of the UV/optical emission, with a decreasing  $T_p$  with time. This behavior is observed even for the sources with faint X-ray emission at early times.

In a Newtonian time evolving standard disk (Shakura & Sunyaev 1973; Cannizzo et al. 1990), the peak temperature follows a power law in time for a power-law declining accretion rate,  $T_p \propto t^{(-n/4)}$ , where  $n$  depends on the boundary conditions of the accretion disk: for finite stress at the innermost stable circular orbit (ISCO),  $n \approx 0.8$ , for a vanishing ISCO stress  $n \approx 1.2$  (Mummery & Balbus 2020). These solutions seem to qualitatively agree with the observed behavior shown by the filled ( $T_p \propto t^{(-1.2/4)}$ ) and dotted ( $T_p \propto t^{(-0.8/4)}$ ) black lines in Fig. 8. The current quality/cadence of available data on X-ray TDEs does not allow for a more detailed assessment of the temperature evolution.

For a standard disk emission,  $T_p$  should also correlate with the bolometric luminosity, in the form  $L_{disk,bol} \propto T^4$ , while the relation with the observed X-ray luminosity should have a more general form of  $L_X \propto T^\alpha$ , where  $\alpha$  is related to both the temperature evolution (i.e.,  $n$ ) and the measured temperature itself, given that the latter dictates the fraction of the bolometric luminosity emitted in the X-ray band.

In the top panel of Fig. 9, we show that such correlation is observed for several sources. However, some sources, namely AT2018zr, AT2019azh, ASASSN-15oi, and OGLE16aaa, show a decoupling between  $L_X$  and  $T_p$ . Such decoupling is a result of their maximum  $T_p$  occurring at early times (like all other sources), while their X-ray luminosity is at the faintest levels at early times ( $L_X \leq 10^{42}$ ), which runs contrary to the expectation of higher luminosity at higher temperatures. All these sources are either *Late-time brightening* or *X-ray faint* sources. The resulting decoupling, driven by the faint early-time X-ray emission, can also be seen by the color of the points in Fig. 9 representing their  $L_{BB}/L_X$  values: all sources that show  $L_X \propto T^\alpha$  (top panel) have  $L_{BB}/L_X < 10$  in all epochs, sources with decoupling between  $L_X$  and  $T_p$  have epochs with  $L_{BB}/L_X \gg 10$ , and it is in those specific epochs that the decoupling is observed. These results points towards a suppression of the X-ray flux/luminosity in this sources/epochs, while the observed  $T_p$  seems be following its expected behavior. An X-ray spectrum of AT2020ksf (another *Late-time brightening* source) at its early-time X-ray faint phase is not available to confirm whether such decoupling from the expected relationship is also present.

A similar analysis can be done regarding the apparent radius of the peak disk temperature ( $R_p$ ); for a standard disk (with no ionizing/neutral absorption or/and reprocessing), the temperature should peak near the ISCO, i.e.,  $R_p \approx R_{ISCO} = (1 - 6) \times R_g$  (depending on the MBH spin), where  $R_g = GM_{BH}/c^2$  is the gravitational radius. Given that the (systematic plus statistical) un-

certainties in  $M_{BH}$  derived from scaling relations (see §2.3) are in the order of 0.5 dex, any measured radius in the  $0.3 \leq R_p/R_g \leq 20$  range is still statically consistent with being emitted near the  $R_{ISCO}$ .

From Fig. 11, it is clear that for most sources/epochs, the recovered  $R_p$  are within the physically valid interval (i.e.,  $0.3 \leq R_p/R_g \leq 20$ ) hence are consistent with  $R_{ISCO}$ , in agreement with Mummery et al. (2023) findings. However, some epochs/sources show unphysically low values, i.e.,  $R_p/R_g \ll 0.3$ , interestingly these sources show a large apparent  $R_p$  evolution, from unphysical values at early times to valid reasonable values at late times; a consequence of this is that the  $R_p/R_g$  seems closely connected with  $L_{BB}/L_X$  (and hence the distinct light curve evolution classes): the epochs with  $R_p/R_g \ll 0.3$  are the epochs with higher  $L_{BB}/L_X$  (this can also be seen in Fig. 15). This correlation is not only observed for the general sample but also in distinct epochs of the same source (see, e.g., AT2019azh, OGLE16aa, AT2018zr in Fig. 11).

The  $L_{BB}/L_X$  (hence the shape of the SED) for a standard accretion disk also has a limiting range of values; based on our simulation shown in §B, for  $T_p$  range measured in our sample (i.e.,  $5.5 \leq \log T_p \leq 6.1$  K), the ratio between the observe  $L_{BB}$  and  $L_X$ , can only be  $5 \times 10^{-2} \leq L_{BB}/L_X \leq 70$ . Combing the valid ranges for  $L_{BB}/L_X$  and for  $R_p/R_g$ , in Fig. 11 we show in a gray shaded region the space of parameters in which derived properties *could*, in principle, be explained by a *bare/unreprocessed* accretion disk. For observations that fall outside this region, however, the derived parameters are inconsistent with the ones of a *bare/unreprocessed* disk; hence additional radiative processes must be present. Interestingly, the epochs/sources in which the measured  $L_{BB}/L_X$  and  $R_p/R_g$  fall outside the disk region are the same epochs/sources that are decoupled from the  $L_X \propto T^\alpha$  relation. i.e., all sources showing faint X-ray emission at early times.

In the following paragraphs we aim to demonstrate that the apparent unphysical  $R_p/R_g$  values derived from *X-ray faint* sources and the early-time observations of *Late-time brightening* are evidence for the suppression of the emitted X-ray in these sources/epochs and can be explained by the way that  $R_p$  is ‘measured’ by the X-ray continuum fitting.

In the color-corrected quasi-Wien approximation of `tdediscspec`<sup>8</sup>, the X-ray spectrum ( $F_X(\nu)$ ) is related to  $R_p$  and  $T_p$  as follows:

<sup>8</sup> The specific equations are for `tdediscspec` but the same arguments holds for any thermal model.

$$F_X(\nu) \propto \left(\frac{R_p}{D}\right)^2 \tilde{T}_p^\gamma \exp\left(-\frac{h\nu}{k\tilde{T}_p}\right) \quad (3)$$

where  $\tilde{T}_p = f_{col} f_\gamma T_p$  (see definitions in §3), and  $D$  is the source luminosity distance. This means that the shape of the X-ray spectra shape depends exclusively on  $T_p$ , but not on  $R_p$  which is only a ‘physically scaled’ normalization factor that translates the observed count rate per energy bin to a flux per energy bin. Similarly,

$$L_X \propto R_p^2 \tilde{T}_p^\gamma \int_{\nu_i}^{\nu_f} \exp\left(-\frac{h\nu}{k\tilde{T}_p}\right) d\nu \quad (4)$$

where  $\nu_i = \frac{0.3 \text{ keV}}{h}$  and  $\nu_f = \frac{10 \text{ keV}}{h}$ . Therefore for a constant  $T_p$ ,  $L_X \propto R_p^2$ , while  $L_X$  decreases with decreasing  $T_p$  for constant  $R_p$ .

As we have shown, all sources – including those with faint X-ray emission at early times – show a decreasing or constant  $T_p$  with time; this means that their faint X-ray emission and late time X-ray brightening (or constant  $L_X$ , in AT2018zr) will translate into to an extremely low  $R_p$  at early times and an order of magnitude increase in  $R_p$  at late times. Such behavior is a consequence of eq. 4 in which  $R_p$  can not be constant with time if  $T_p$  is decreasing (or held constant) and  $L_X$  is not decreasing – as is the case for all sources in the bottom panel of Fig. 9.

One can take the earliest ( $\Delta t = 21$  days) spectrum of AT2019azh as an example: the measured temperature and apparent radius were  $\log T_p \approx 5.75$  K and  $R_p/R_g \approx 6 \times 10^{-2}$ , while  $L_X \approx 2 \times 10^{41} \text{ erg s}^{-1}$ . In order for the  $R_p/R_g$  to be within the physically valid range (i.e., to be at least 0.3), based on eq. 4, the observed luminosity would have to be higher by a factor of  $\left(\frac{0.3}{0.06}\right)^2 \approx 25$ , similarly, for the early time  $R_p/R_g$  to be at the same value as the late-time  $R_p/R_g \approx 3$  (hence a physically valid and approximately constant value during its entire evolution) the observed early time  $L_X$  would have to be higher by a factor of  $\left(\frac{3}{0.06}\right)^2 \approx 2 \times 10^3$ . Such an increase would make the early time  $L_X$  to be coupled to the  $T_p$  during the entire evolution of the source, as can be seen by the bottom panel of Fig. 9.

A similar analysis can be done for the early time spectra of all the *Late-time Brightening* and *X-ray faint* sources, that show this unphysical value/evolution of the apparent  $R_p$ , for all of them an increase in the  $L_X$  by a factor  $\gg 10$  is necessary for a physical value of  $R_p/R_g$ , given their measured temperature evolution.

In summary, the unphysical values of  $R_p/R_g$ , accompanied by decoupling between  $L_X$  and  $T_p$ , and a SED shape ( $L_{\text{BB}}/L_X$ ) inconsistent with an accretion disk, indicates suppression of the emitted X-rays in these

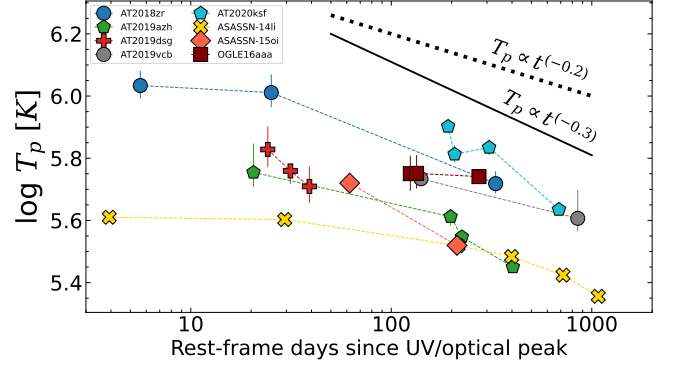


**Figure 8.** Peak temperature ( $T_p$ ) of the accretion disk model as function of days since the UV/optical peak. Only sources with at least two fittable spectra and with no corona emission (see §4.3) are shown. The solid black line show the expected theoretical evolution for a finite stress at the innermost stable circular orbit.

epochs/sources. However, such suppression of the X-ray emission seems to have a small effect in the measured  $T_p$  – given that the cooling of the accretion disk is still observed and is independent of the observed flux level – while suppression of the total observed X-ray flux is high. We will discuss possible mechanisms responsible for such suppression in §5.1. In Mummery et al. (2023), when the authors average all  $R_p$  values obtained in each spectrum to find a  $\langle R_p \rangle$  for each source, the information on the unphysical nature of the  $R_p/R_g$  obtained at early times was missed. Furthermore important data such as high S/N X-ray spectra of, for example, AT2019azh at early times and AT2018zr at late times, as well as a  $M_{\text{BH}}-\sigma_*$  measurement of AT2018zr’s black hole mass were not available to the authors, but are presented here. Although, we agree on the authors main claim, i.e.  $R_p$  is tracing  $R_{\text{ISCO}}$ , we show that this is only valid in the cases where the X-rays are not suppressed and the SED is consistent with a *bare/unreprocessed* disk, which is usually not the case for the very early times of optically discovered TDEs (as we will discuss in §4.4).

#### 4.3. Soft $\rightarrow$ Hard Transition: Real-Time Corona Formation

The X-ray spectra of AT2018fyk, AT2020ocn, and AT2021ehb exhibit extreme softness at early times ( $\Delta t \leq 100$  days), similar to other spectra in our sample. However, these three sources undergo a transition to a hard power-law-like state with a timescale of  $\sim 200$  days after the UV/optical peak. The power-law component dominates the disk emission in this state and extends to much higher energies than in the soft state. As an extreme example, the *NuSTAR* spectra of AT2021ehb presented by Yao et al. (2022) show power-law emission detected above background up to 30 keV.

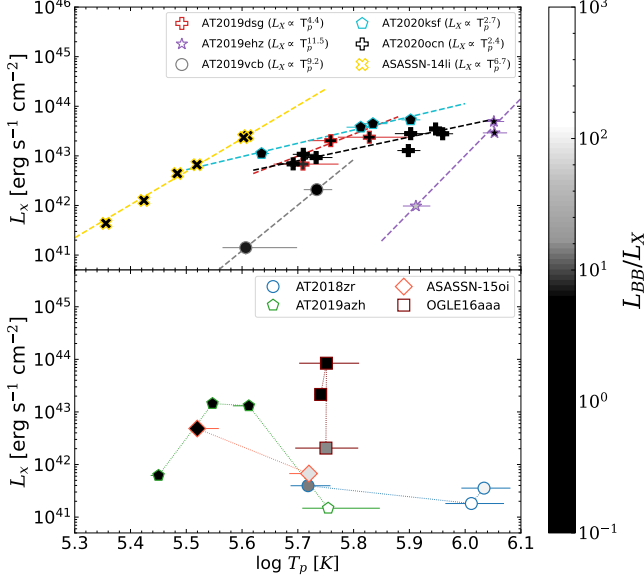


**Figure 9.** X-ray luminosity ( $L_X$ ) as a function of peak temperature ( $T_p$ ). The upper panel show sources where a  $L_X \propto T_p^\alpha$  relation is observed, with the best-fitted  $\alpha$  for each source shown in the legend. The bottom panel show the source where a clear decoupling between  $L_X$  and  $T_p$  is present. The color in which the markers are filled maps the  $L_{BB}/L_X$  ratio between the UV/optical luminosity and the  $L_X$  following the color-bar in the right side if the figure.

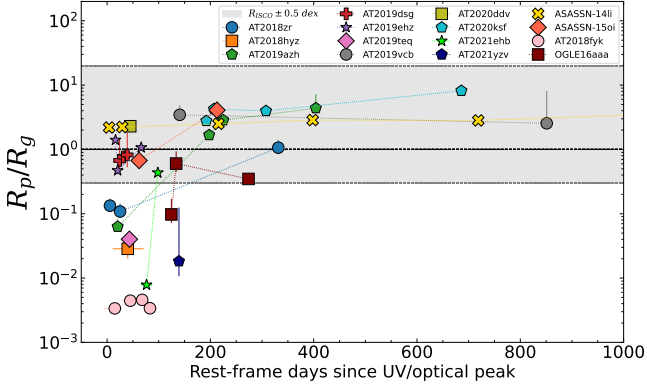


**Figure 10.** Apparent radius ( $R_p$ ) of the peak temperature normalized by the gravitational radius ( $R_g$ ) as function of days since the UV/optical peak. Only sources with no corona emission (see §4.3) are shown. Gray shaded region shown the  $0.3 \leq R_p/R_g \leq 20$  interval in which the measured  $R_p/R_g$  is statistically consistent with  $R_{ISCO}$ .

In the case of AT2018fyk, a faint hard excess ( $f_{sc} \leq 0.05$ ) emerges around  $\Delta t \approx 50$  days, followed by a rapid formation of a strong coronal component between  $50 \leq \Delta t \leq 200$  days. By  $\Delta t = 209^{+34}_{-35}$  days, the *Swift*/XRT spectrum already exhibits  $f_{sc} \approx 0.2$ , and the corona emission peaks at  $\Delta t = 209^{+45}_{-30}$  days with  $f_{sc} \approx 0.3$ . During this phase, the power-law component

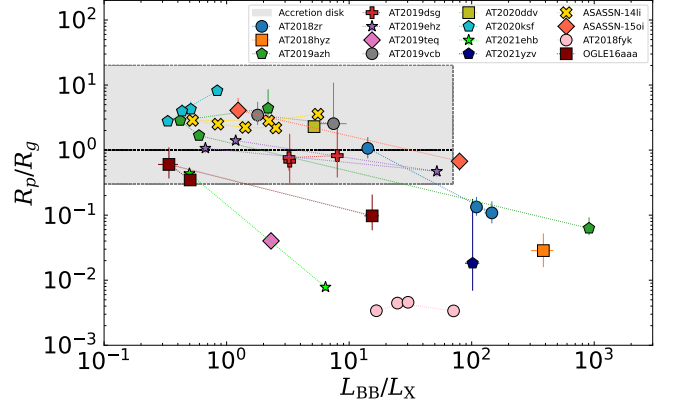


**Figure 11.** Distribution of apparent disk radius ( $R_p$ ) normalized by the gravitational radii ( $R_g$ ), and the  $L_{BB}/L_X$  ratio between the UV/optical luminosity and the X-ray luminosity. The shaded gray region delimits the parameters space in which the emission can be explained by a *bare/unreprocessed* standard accretion disk, see text for details. Several sources/epochs fall outside this region having unphysically low  $R_p/R_g$  values while also having SED shapes ( $L_{BB}/L_X$ ) that, deviate from the allowing SED shape of disk, and require additional radiative processes.

dominates the X-ray flux over the thermal component, with the fraction of up-scattered photons decreasing to  $f_{sc} \approx 0.15$  at  $\Delta t \approx 350$  days, remaining relatively constant until the source becomes undetectable in the X-rays at  $\Delta t = 500$  days. In the case of AT2020ocn, the state transition is more extreme, remaining completely soft and disk-dominated ( $f_{sc} = 0.00$ ) up to  $\Delta t \approx 200$  days. However, a spectrum taken after a seasonal gap at  $\Delta t \approx 290$  days reveals the corona dominating the X-ray emission ( $f_{sc} \approx 0.5$ ). The source persists in this hard state for at least 100 days, transitioning to an intermediate state again at  $\Delta t \approx 700$  days. For AT2021ehb, a hard excess ( $f_{sc} \approx 0.02 - 0.05$ ) is present from the first X-ray detections at  $\Delta t \approx 70 - 100$  days.  $f_{sc}$  then gradually increases to  $\sim 0.15$  at  $\Delta t \approx 200$  days, followed by an abrupt transition to a corona-dominated state ( $f_{sc} \approx 0.5$ ) at  $\Delta t \approx 250$  days, resembling typical AGN X-ray spectra. The source subsequently transitions back to an intermediate state around  $\Delta t \approx 300$  days. Figure 12 illustrates the evolution of the softest early-time spectrum (left panels), the hardest spectrum (middle panels), and the intermediate state at very late times (right panels) for the three sources, depicting the formation of the corona.

Transitions from a soft disk-dominated state to a hard corona-dominated state are commonly observed in stellar-mass black holes in X-ray binary systems. They follow a standard *q-shape* evolution in the hardness-intensity diagram (HID, e.g., Remillard & McClintock 2006; Wang et al. 2022). However, in the case of MBHs,

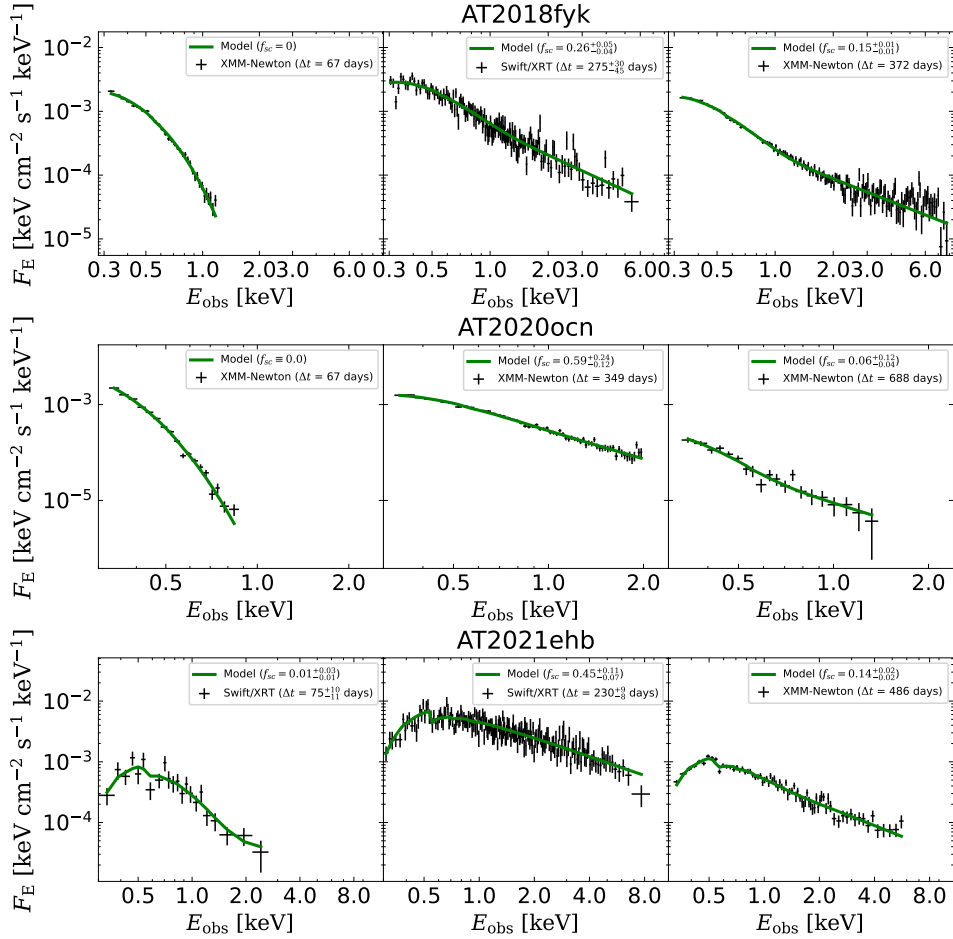


**Figure 12.** Spectral evolution of the three sources that show soft  $\rightarrow$  hard state transition, i.e., corona formation. From top to bottom: AT2018fyk, AT2020ocn, and AT2021ehb. From left to right: early time soft state spectra, hardest state spectra, and late-time intermediate state spectra. Unfolded spectra are shown in black crosses, best fitted models are shown in green.

the corona is a ubiquitous and dominant component of the X-ray spectra of AGN. Dramatic state transitions, such as the appearance or disappearance of X-ray power-law emission, are usually not observed in AGN, except in the case of the Changing-look AGN 1ES 1927+654 (Trakhtenbrot et al. 2019; Ricci et al. 2020), where the corona was destroyed and later reformed. Therefore, X-ray bright TDEs provide a new window for studying the emission and formation of this poorly understood component.

A study by Wevers et al. (2021) suggested that AT2018fyk exhibits a “Fainter harder brighter softer” behavior similar to X-ray binary outbursts. Additionally, Wevers (2020) argued that this behavior could be ubiquitous in X-ray bright TDEs. The HID analysis conducted by Wevers et al. (2021) involved using the  $\alpha_{OX}$  parameter, defined as the logarithmic ratio between the UV flux (representing the disk emission) and the 2 keV flux (representing the corona emission), along with the

bolometric luminosity ( $L_{\text{Bol}}$ ) normalized by the Eddington luminosity ( $L_{\text{Edd}}$ ).

The HID in the left panel of Fig. 13 illustrates corona formation for the three sources using  $\frac{f_{\text{sc}}}{\max(f_{\text{sc}})}$  for hardness and  $\frac{L_{\text{BB}}+L_{\text{X}}}{L_{\text{Edd}}}$  for intensity. Representing the relative corona strength and intensity, respectively. Given the uncertainty in the spectral energy distribution (SED) shape between the UV and X-ray regions, we use  $L_{\text{BB}} + L_{\text{X}}$  as a proxy for  $L_{\text{Bol}}$ <sup>9</sup> and  $\frac{L_{\text{BB}}+L_{\text{X}}}{L_{\text{Edd}}}$  as a proxy for the Eddington ratio. From the left panel of Fig. 13, it can be observed that all three sources start in a soft state and then quickly transition to a hard state. The transition occurs at  $\frac{L_{\text{BB}}+L_{\text{X}}}{L_{\text{Edd}}}$  values

<sup>9</sup> A significant portion of the bolometric luminosity should be emitted in the unobserved extreme UV (EUV) range, the shape of the SED between the UV and X-ray regions is not fully understood and highly dependent on models, especially when the total SED deviates from a standard accretion disk SED (e.g., when  $L_{\text{BB}}/L_{\text{X}} \gg 10$ , see §4.4). The actual value of  $L_{\text{Bol}}$  would be much higher if the EUV emission were taken into account.



between  $5 \times 10^{-3}$  and  $5 \times 10^{-2}$  for the three sources. However, as time passes and the luminosity decreases, all sources undergo further transitions, either returning to a completely soft state or transitioning to an intermediate state ( $0.05 \leq f_{sc} \leq 0.15$ ); this behavior contrasts with the *Fainter harder brighter softer* pattern.

In the right panel of Fig. 13, we compare the power-law index ( $\Gamma_{sc}$ ) of the emerging corona in the three TDE showing a state transition ( $f_{sc} \geq 0.1$ ) to the corona power-law index ( $\Gamma$ ) measured from the population of unobscured ( $N_H \leq 10^{22} \text{ cm}^2$ ) AGN in the BAT AGN Spectroscopic Survey (BASS, Ricci et al. 2017). In the AGN population,  $\Gamma$  exhibits values in a narrow range between 1.2 to 2.5 with a mean value of  $\Gamma \approx 1.7$ , TDEs however, even at their harder state are rarely as hard as AGN, instead their  $\Gamma_{sc}$  can exhibit a broader range of values between 1.7 and 4.0.

The characteristic power-law spectrum, is thought to be produced by the Comptonization of lower energies photons emitted by the accretion disks by a corona of hot electrons (Haardt & Maraschi 1991; Titarchuk & Lyubarskij 1995) located within a light-hour from the accreting massive black hole (Fabian et al. 2009). The process depends on the Compton parameter  $y$ , given by:

$$y = \frac{k T_e}{m_e c^2} \max(\tau_e, \tau_e^2) \quad (5)$$

where  $\tau_e$  and  $T_e$  are, respectively, the corona optical depth and electron temperature of the corona; the resulting power-law spectrum has a photon index has a inverse dependence on  $y$ .

Although the exact mechanism responsible for the corona formation is still to be fully understood, the need for a strong magnetic field is common feature of the different models. In all three sources, the spectrum is soft at early times, and the complete hardening of the X-ray spectrum is only observed at  $\Delta t \geq 200$  days. This gradual hardening process suggests that it takes approximately  $10^2$  days for the magnetically dominated hot corona region to develop. The initial weak magnetic fields present in the bound debris could undergo amplification through the combined effects of the disk's differential rotation and the magnetorotational instability (Balbus & Hawley 1991; Miller & Stone 2000; Yao et al. 2022).

Although the corona forms in these sources, their hard state is short-lived, transitioning back to a soft/intermediate state at later times ( $\Delta t \gg 400$  days). This suggests that the high optical depth corona cannot be sustained as the accretion rate onto the black hole decreases. Another indicator of inefficient corona formation is the measured  $\Gamma_{sc}$  (see the right panel of Fig.

13). TDE spectra exhibit higher power-law indices compared to typical AGN spectra, translating to lower values of  $T_e \times \max(\tau_e, \tau_e^2)$  – based on the equation 5, and the inverse relation between  $\Gamma$  and  $y$  – when compared with AGN corona. Distinguishing between  $\tau_e$  and  $T_e$  effects requires detecting the cut-off energy ( $E_{cut}$ ) of the power-law spectra, feasible with instruments like *NuSTAR* for bright AGN but currently challenging for TDEs. The proposed High Energy X-ray Probe (Madsen et al. 2019, HEX-P) may enable  $E_{cut}$  measurements in bright TDEs. The reasons why only these three sources exhibit corona formation remains unclear; while all three have  $M_{BH} \geq 5 \times 10^6 M_\odot$  – at the high-mass end of the TDE  $M_{BH}$  function and consistent with sub-Eddington accretion requirements – a high  $M_{BH}$  alone does not seem sufficient, as other TDEs with similar  $M_{BH}$  did not show such state transitions.

#### 4.4. SED Evolution

A natural consequence of the diversity of X-ray light curves and the uniformity of the UV/optical light curves is that the spectral energy distribution (SED) shows very distinct shapes and evolution. The shape of the broad-band SED can be probed by the  $L_{BB}/L_X$  ratio. As shown in the right panels of Fig. 7; these ratios can vary between  $\text{few} \times 10^3$  and  $\text{few} \times 10^{-2}$ . In Fig. 14, we show the cumulative distribution of  $L_{BB}/L_X$  at three time bins, early times ( $\Delta t \leq 50$  days) in purple, and at late times ( $150 \leq \Delta t \leq 250$  days) in orange, and very late times ( $400 \leq \Delta t \leq 800$  days) in black. The SED also show a noticeable trend: at early times they have  $L_{BB}/L_X$  as large as 3000 and as low as 0.5, but with most sources showing  $L_{BB}/L_X \geq 10$ ; with increase time from optical peak this range of  $L_{BB}/L_X$  shrinks, and at very late times all sources show  $0.5 \leq L_{BB}/L_X \leq 10$ .

As discussed in §4.2 and demonstrated in Appendix §B, the SED produced by a *bare/unprocessed* standard accretion disk with  $T_p$  in the range of values find in TDEs (i.e,  $5.5 \leq \log T_p \leq 6.1$  K) can only produce  $5 \times 10^{-2} \leq L_{BB}/L_X \leq 70$ . Therefore the values of  $L_{BB}/L_X$  in the range 100-3000 found in the early times of a large fraction of our sources indicate that an additional emission mechanism that deviates from a standard accretion disk-corona is operating. The deviation from a standard disk is stronger at early phases, given that the  $L_{BB}/L_X$  ratios converge towards the expected disk values at late times.

In Fig. 15, we explore how a standard disk SED compares with the observed SED for three distinct TDEs: one *Power-law Decaying*, one *Late-time brightening* and one *X-ray faint*. We assume a color-corrected disk so-

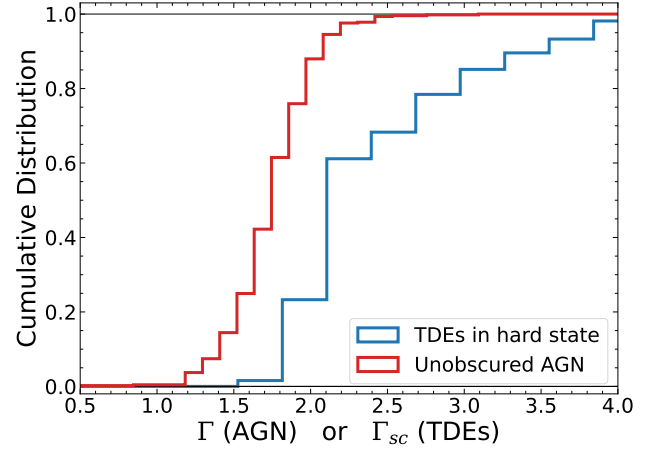
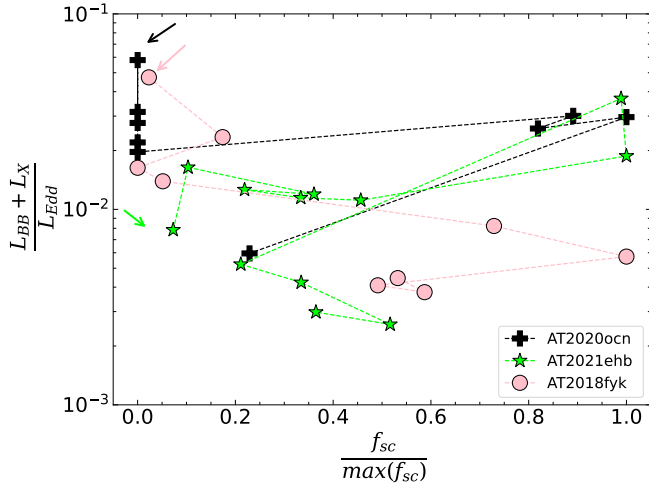


**Figure 13.** Properties and evolution of the corona emission in TDEs. Left: Hardness intensity diagram (HID), the total observed luminosity ( $L_{BB} + L_X$ ) in units of the Eddington luminosity, as a function of the hardness as traced by the normalized fraction ( $f_{sc}$ ) of the photons upper-scatter by the corona. The arrows indicate the first available spectra for each source, and the points are connected by increasing  $\Delta t$ . Right: comparison between the power-law index of the corona emission spectra in local AGN ( $\Gamma$ , blue) from the BAT AGN Spectroscopic Survey (BASS), and TDEs ( $\Gamma_{sc}$ , red) that show corona formation (AT2020ocn, AT2021ehb, AT2018fyk).

lution, where the SED can be obtained numerically, as approximately:

$$L(\nu) \approx \frac{8\pi^2}{f_{col}^4} \int_{R_p}^{R_{out}} B_\nu(\nu, f_{col}T(r)) r dr \quad (6)$$

where  $B_\nu(\nu, T)$  is a Planck function,  $T(r)$  is the temperature radial profile of the disk,  $T(R_p) = T_p$ , and  $R_{out}$  is the outer radius of the disk. For a given values of the inner temperature ( $T_p \pm \delta T_p$ ) and radius ( $R_p \pm \delta R_p$ ) – obtained from the the X-ray fitting – the expected UV/optical emission will depend on the extended disk structure, its size, i.e.,  $R_{out}/R_p$  ratio, and its temperature profile  $T(r)$ . At early times  $R_{out}$  should be limited to the circularization radii ( $R_{circ}$ ), which for a solar-like disrupted star is:

$$R_{out} = R_{circ} = 2R_T = 94R_g(M_{BH}/10^6 M_\odot)^{-2/3} \quad (7)$$

where  $R_T$  is tidal disruption radius. However, at late times such requirement is lifted due to viscous spread of the disk. To emulate our ignorance on the extended properties of the disk, we generated a series of solutions to equation 6, assuming disk sizes between  $R_{out}/R_p \in (5, 50)$ , temperatures profiles as  $T(r) \propto r^{-3/4}$  (for a vanishing ISCO stress, Shakura & Sunyaev 1973; Cannizzo et al. 1990) and  $T(r) \propto r^{-7/8}$  (for a finite ISCO stress, Agol & Krolik 2000; Schmittman et al. 2016), and the range of the  $1\sigma$  uncertainty for  $T_p$  and  $R_p$ . The shaded gray region in Fig. 15 represents the region of possible solutions resulting from the assumed parameters. Our goal is to visualize how much the full SED deviates from

a standard disk SED, and how much UV/optical ‘excess’ is present.

From the top panel of Fig. 15, we can see that the SED of ASASSN-14li is not far from an accretion disk SED; very little UV/optical excess is present even at early times; at late time the SED is consistent with an accretion disk, furthermore, the evolution in SED shape with time is very small and compatible with the cooling of the disk. The same holds for the other *Power-law decaying* sources, although for AT2019dsg the rapid decay of X-ray emission indicates a quicker cooling of the disk (Cannizzaro et al. 2021).

For AT2019azh, however, the disk emission extrapolated from the X-rays under-predicts the UV/optical emission by more than two orders of magnitude, as can be seen from the left middle panel of the Fig. 15. This is mainly a consequence of the low X-ray luminosity  $L_X \approx 5 \times 10^{41}$  erg s $^{-1}$  and high  $T_p$ , that result in both an unphysical  $R_p/R_g$  and a high  $L_{BB}/L_X \approx 890$ . At later times however,  $L_{BB}$  decays and  $L_X$  brights ( $L_{BB}/L_X \approx 1$ ), and the SED is consistent with a standard accretion disk. Such behavior is observed in all *Late-time brightening* sources. One should notice that in AT2021ehb, the  $L_{BB}/L_X$  reaches extremely low value  $\sim 10^{-2}$  given the strong corona formation that increases  $L_X$ , consequently decreasing  $L_{BB}/L_X$ .

In the case of AT2018zr, the early time is very similar to AT2019azh; however, even at  $\Delta t \approx 331$  days, the SED is yet not consistent with a standard disk, although the UV/optical excess does decrease, while  $L_X$  is approximately constant during the entire evolution. Similar

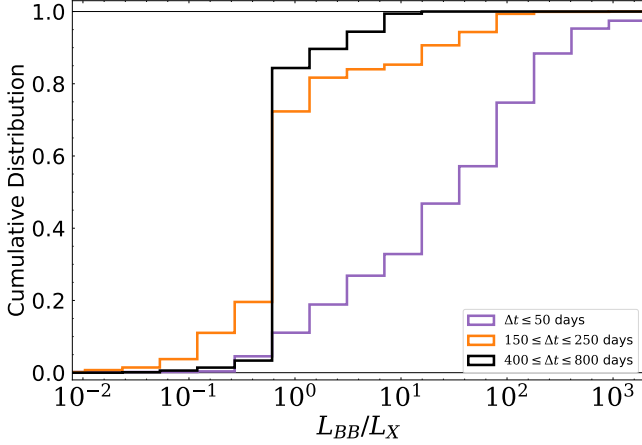


**Figure 14.** Evolution of the distribution of SED shapes, as trace by the ratio ( $L_{BB}/L_X$ ) between the UV/optical luminosity ( $L_{BB}$ ) and the 0.3-10 keV luminosity ( $L_X$ ). Each color show the distribution in a different time bin. The contribution of each source for the total distribution was weighed by the number of spectral observation available in each  $\Delta t$  interval.

behavior is found in the other *X-ray faint sources*. The physical interpretation of the diversity of SED shapes at early times and the convergence to a disk-like SED at late times, will be discussed and compared with the theoretical expectations in §5.1.

As discussed in §4.2, there is a clear anti-correlation between  $L_{BB}/L_X$  and the radius derived from the X-ray spectral fitting,  $R_p/R_g$  assumes nonphysical values at the highest  $L_{BB}/L_X$  (usually with  $L_{BB}/L_X \gg 10$ ), this can also be seen in the legend of Fig. 15. In light of the discussion of this current section and §4.2, we can conclude that  $R_p/R_g$  values are nonphysical when the SED strongly deviates from the SED of a standard disk. Both lines of evidence point towards the suppression of the observed X-ray emission as discussed in §4.2.

#### 4.5. The ratio of X-ray loud TDEs in optical surveys and its (in)dependence on $M_{BH}$

A surprising characteristic of the population of TDEs discovered by optical surveys is the lack of detectable X-ray emission in most sources, contrary to that first theoretical expectation (Rees 1988) and the fact that first TDE were discovered in the X-rays (e.g., Bade et al. 1996). We would like to determine the fraction ( $N_{opt,x}/N_{opt}$ ) of optically discovered TDEs that show X-ray emission. Therefore, a controlled sample of total discovered TDE and X-ray bright TDEs needs to be compared.

We will use the first 3 years of the ZTF (October 2018 to August 2020 for ZTF-I and September 2020 to August 2021 for ZTF-II) survey to determine this ratio. After a

ZTF TDE candidate (see, van Velzen et al. 2021; Yao et al. 2023b, for selection criteria) is spectrally classified, a few *Swift* observations are performed to confirm the UV brightness characteristic of TDEs and check whether the source is detected in the X-rays. The number of visits and the cadence varies from source to source, but at a minimal a few 1-2 ks long observations (usually with a total of  $\sim 10$  ks) are performed, leading to a detection limit of  $\sim 5 \times 10^{-14}$  erg cm $^{-2}$  s $^{-1}$  with XRT, which means any TDE with  $L_X > 10^{42}$  erg s $^{-1}$  can be detected up to  $z \approx 0.09$ , while  $L_X \sim 10^{41}$  erg s $^{-1}$  can only be detected if extremely nearby ( $z < 0.04$ ). Therefore, we will use  $L_X \geq 10^{42}$  erg s $^{-1}$  to define the sub sample X-ray bright TDEs. During the first three years of ZTF 10 sources showed, at some point in time,  $L_X \geq 10^{42}$  erg s $^{-1}$ , therefore  $N_{opt,x} = 10$ .

To construct the control sample, we start with all TDEs discovered by ZTF during the same time period (from van Velzen et al. 2021; Hammerstein et al. 2023a; Yao et al. 2023b). For sources at  $z < 0.09$  (24 sources), we select those with *Swift*/XRT observations, for sources with no XRT detection we stacked all their *Swift*/XRT observations and check whether  $L_X$  upper-limit (after correcting for Galactic absorption) was deeper than  $10^{42}$  erg s $^{-1}$ . Only 3 sources (AT2021mhg, AT2021sdu, AT2021yte) the upper limit were not deep enough to constraint the presence  $L_X \geq 10^{42}$  erg s $^{-1}$ , particularly because of their higher Galactic absorption  $N_{H,G} \geq 10^{21}$  cm $^{-2}$ , than the typical  $N_{H,G} \approx \text{few} \times 10^{20}$  cm $^{-2}$  of the other sources. For our typical exposure times, *XMM-Newton* detection limit is around  $5 \times 10^{-15}$  erg cm $^{-2}$  s $^{-1}$ , this means that we can detected  $L_X > 10^{42}$  erg s $^{-1}$  up to  $z \approx 0.25$ . Therefore, we include all sources at  $0.09 \leq z \leq 0.25$  that had at least one *XMM-Newton* visit to our control sample (adding 4 more sources). This results in 25 sources in which a  $L_X \geq 10^{42}$  erg s $^{-1}$  could be (or was) detected if such level of emission was present, hence  $N_{opt} = 25$ . Therefore for ZTF, we obtain  $N_{opt,x}/N_{opt} = 10/25$ , meaning that in ZTF,  $\sim 40\%$  of the discovered TDEs had (eventually) some X-ray bright emission ( $L_X \geq 10^{42}$  erg s $^{-1}$ ). The list of the 25 TDEs and their redshift are present in Table 5. Given the non-uniformity of the X-ray follow-up, particularly at late-time for those at higher  $z$ , the ratio should be seen as a lower-limit.

We also use this above-defined sub samples to investigate whether the presence of  $L_X \geq 10^{42}$  is dependent on  $M_{BH}$ . In Fig. 16 we show the cumulative distribution of  $M_{BH}$  for the two sub samples ( $L_X$  higher and lower than  $10^{42}$  erg s $^{-1}$ ), where the underlying distribution was constructed by adding a normalized probability dis-

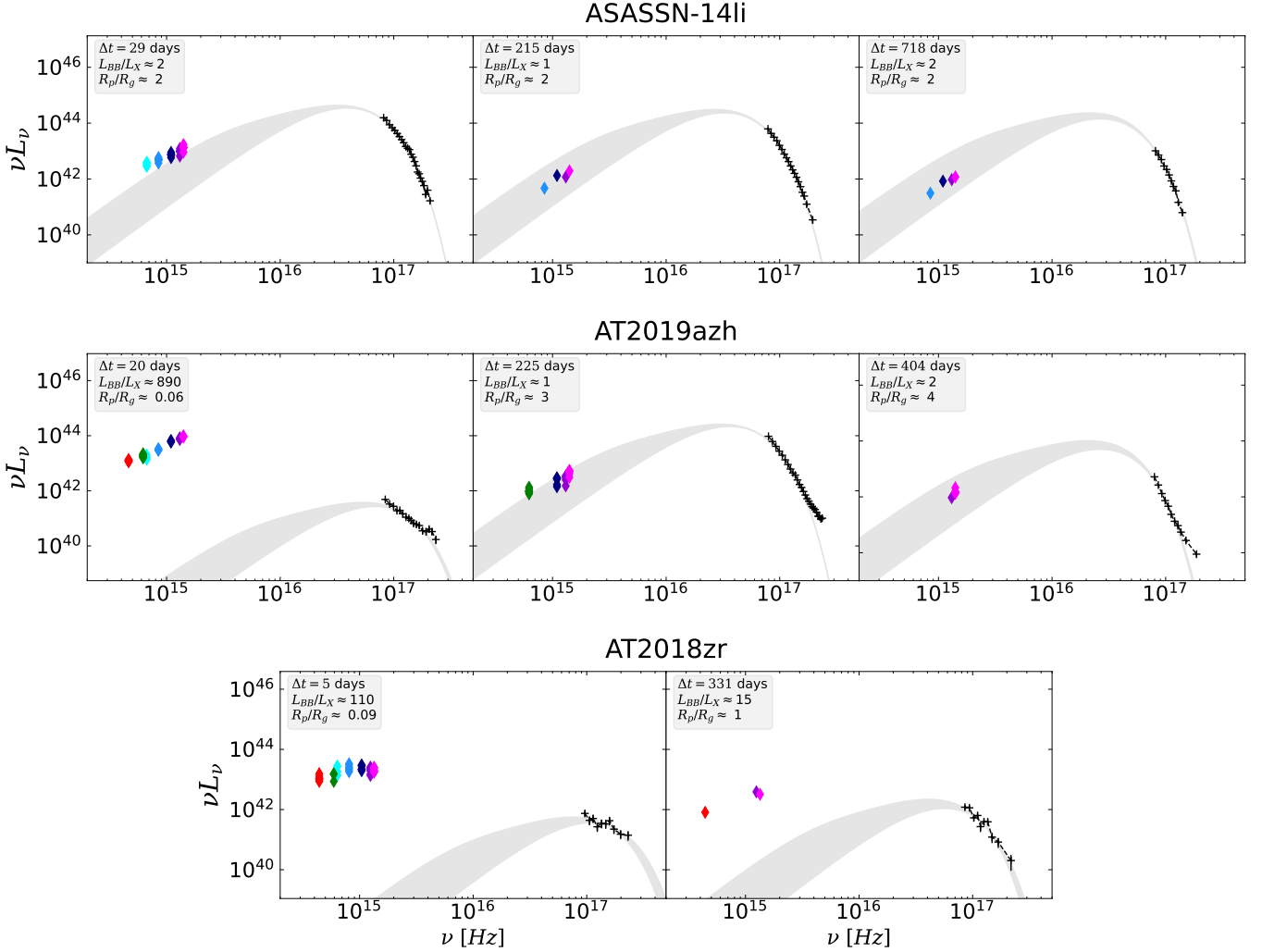


**Figure 15.** Evolution of the SED for three sources, one *Power-law decaying* (Top), one *Late-time Brightening* (middle), and one *X-ray faint* (bottom). Left panels show early time ( $\Delta t \leq 30$  days) SED, middle panel show late time SED ( $\Delta t \approx 200$  days) and right panel show very-late time SED ( $\Delta t \approx 400$  days). No X-ray spectrum of AT2018zr around  $\Delta t \approx 200$  days is available. The colored point show the observed UV/optical photometry (ZTF + *Swift*/UVOT), the black crosses show the unfolded X-ray spectrum, the gray line show the best-fitted disk model (and uncertainty) for the X-ray spectra, and its extrapolation to the UV/optical band is shown in shaded region (see text for details). Main parameters of interest are shown in the legend for each epoch.

tribution function (PDF) based on estimated  $M_{\text{BH}}$  and their uncertainties (see §2.3).

From Fig. 16 there seems to be no distinction between the  $M_{\text{BH}}$  distribution of TDE  $L_{\text{X}}$  higher/lower than  $10^{42}$  erg  $\text{s}^{-1}$ : the difference in the median of the distributions (dotted vertical lines) is only  $\sim 0.1$ dex which is much smaller than the typical uncertainty in  $M_{\text{BH}}$ . In order to statistically investigate the (lack of) difference between the distributions we apply a Kolmogorov-Smirnov test, assuming the null-hypothesis that the two samples are drawn from the same distribution, we recover a  $p$ -value of  $\sim 0.2$ , which means the null-hypothesis can not be excluded, hence there is no statistically significant difference between the distributions. This result

is in agreement with previous ones, that although use distinct samples or selection criteria, also did not find any correlation between X-ray loudness and  $M_{\text{BH}}$  (Wevers et al. 2019b; French et al. 2020; Hammerstein et al. 2023a,b),

#### 4.6. X-ray Luminosity Function

When examining sources with constant flux, such as quasars, the estimation of their luminosity function (LF) involves assigning weights to each source based on its maximum detectable volume,  $V_{\text{max}}$ , as introduced by Schmidt (1968). This approach enables plotting of the number of sources per unit volume as a function of their luminosity. Shifting to transient events, like supernovae

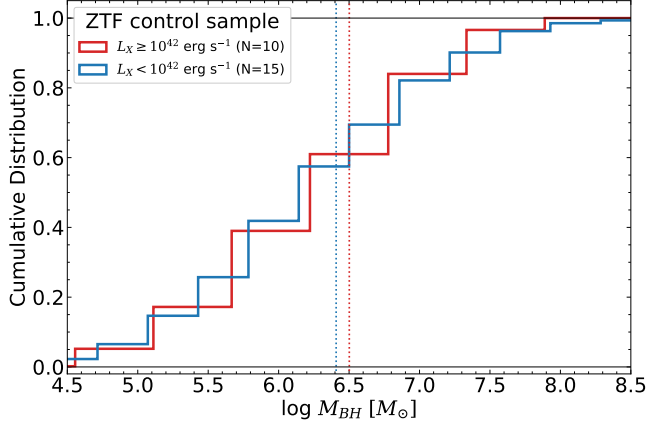


**Figure 16.** Cumulative distribution of black hole mass for the *ZTF control sample* (see §4.5 for definition) with  $L_X$  higher or lower than  $10^{42}$  erg  $s^{-1}$ . The underlying distribution was constructed by adding the normalized PDF of individual sources  $M_{BH}$  based on the estimated values and its uncertainties. No statistically significant difference in the distributions is observed.

(SNe) and TDEs, our interest lies in understanding their volumetric rate, i.e. the number of events per unit volume per unit time relative to their peak luminosity. Extracting this rate from survey data involves applying the “ $1/V_{\max}$ ” method, with a modification accounting for both survey duration and area. This adaptation leads to the definition of a modified parameter,  $\mathcal{V}_{\max}$ :

$$\mathcal{V}_{\max} = V(z_{\max}) A_{\text{survey}} \times \tau_{\text{survey}} \quad (8)$$

where  $A_{\text{survey}} \times \tau_{\text{survey}}$  denotes the product of the effective survey duration and survey area, and  $V(z_{\max})$  is the volume (per unit solid angle) corresponding to the maximum redshift observable with the survey, given its limiting flux.

The luminosity functions of tidal disruption events (TDEs) across different bands have been investigated by a few studies. [van Velzen \(2018\)](#) initially presented a *relative* luminosity function in single-band optical and integrated UV/optical for TDEs, utilizing 13 events discovered before 2018 through UV/optical surveys. Subsequently, [Yao et al. \(2023b\)](#) provided an *absolute* UV/optical luminosity function derived from a sample of 33 homogeneously selected TDEs identified by ZTF. In the X-ray domain, [Sazonov et al. \(2021\)](#) constructed the first luminosity function based on 13 events selected from X-ray transients detected in the  $0^\circ < l < 180^\circ$  hemisphere during *SRG/eROSITA*’s second sky survey. The X-ray luminosity function spanned from  $10^{42.5}$  to  $\leq 10^{45}$  erg  $s^{-1}$  and was best-fitted with a power-law slope of  $0.6 \pm 0.2$ . However, as the X-ray bright TDEs in our study were not discovered by an X-

ray survey but through inhomogeneous follow-up X-ray observations of optically discovered TDEs, and given the non-uniform criteria and cadence for X-ray follow-up, we refrain from obtaining an *absolute* X-ray luminosity function akin to [Sazonov et al. \(2021\)](#). Instead, we propose combining TDEs detected by X-ray surveys with our sample of optically selected X-ray detected TDEs to construct a *relative* luminosity function. This approach aims to provide a broader luminosity range and reduced uncertainty per luminosity bin compared to the one derived from *SRG/eROSITA*, thereby enhancing our ability to constrain its shape.

To construct a large sample of X-ray TDEs, we combine our 17 sources, the 13 discovered by *SRG/eROSITA* ([Sazonov et al. 2021](#)), with 6 discovered by *ROSAT/RASS* and 8 discovered by the *XMM-Newton* Slew Survey as presented in the recent review by [Saxton et al. \(2020\)](#), resulting in 44 X-ray detected TDE ranging from  $10^{41} \leq L_X \leq 10^{45}$  erg  $s^{-1}$ .

We follow the procedures detailed in [van Velzen \(2018\)](#) to construct a *relative* luminosity function from a combined sample discovered by distinct surveys with distinct selection functions and detection efficiency, assuming that each survey discovers events from the same parent distribution so that we can use the discovered/detected number of TDE in each survey to compare the selection efficiencies and thus obtain the *relative* LF. The *effective*  $(A_{\text{survey}} \times \tau_{\text{survey}})^*$  (see Eq. 8) for each survey can be estimated from:

$$(A_{\text{survey}} \times \tau_{\text{survey}})^* \approx \frac{N_{\text{TDE,detected}}}{\dot{N} V(z_{\max*})} \quad (9)$$

where  $N_{\text{TDE,detected}}$  is the number of TDEs detected by the survey, and  $V(z_{\max*})$  denotes the comoving volume (per solid angle) corresponding to maximum redshift ( $z_{\max*}$ ) the survey can detect a ‘typical’ X-ray TDE. We define a ‘typical’ X-ray TDE to have  $L_X^* = 10^{43}$  erg  $s^{-1}$  and  $T_p^* = 60$  eV, and use the detection limit flux ( $F_{X,\text{lim}}$ ) of each survey (see Table 4) to determine  $z_{\max*}$  for each survey. For the optical survey, we assume  $F_{X,\text{lim}}$  to be the flux limit of *Swift*/XRT in a stacked exposure time of 10ks. In eq. 9  $\dot{N}$  is the *assumed* mean event rate which was chosen to be  $\dot{N} = 2 \times 10^{-7}$  Mpc $^{-3}$  yr $^{-1}$ , following [Sazonov et al. \(2021\)](#). The resulting  $(A_{\text{survey}} \times \tau_{\text{survey}})^*$  for each survey is shown in Table 4, while Table 6 show the detailed information from individual sources.

In the upper panel of Fig. 17, we show the distribution of the 44 TDEs in the redshift vs. peak  $L_X$  diagram, where boundaries of the nine  $\Delta \log L_X$  bins are indicated with vertical lines. For a certain bin  $j$  with  $n_j$  TDEs and



**Table 4.** Survey’ Properties

Survey	$N_{TDE}$	$F_{X,lim}$	$(A_{survey} \times \tau_{survey})^*{}^a$
		(erg cm <sup>-2</sup> s <sup>-1</sup> )	(deg <sup>2</sup> yr)
ASASSN+ <i>Swift</i> /XRT	6(3) <sup>b</sup>	$8 \times 10^{-14}$	138
ZTF+ <i>Swift</i> /XRT	12	$8 \times 10^{-14}$	273
OGLE+ <i>Swift</i> /XRT	1	$8 \times 10^{-14}$	22
ROSAT	6	$2 \times 10^{-13}$	2009
XMM-LS	9	$5 \times 10^{-13}$	6484
eROSITA	14	$8 \times 10^{-14}$	645

NOTE—(a) Effective  $A_{survey} \times \tau_{survey}$  as measured from Eq. 9. (b) Three were part of both in ZTF and ASASSN.

width  $\Delta_j \log L_X$ , the rate luminosity function is  $\phi_j = \left[ \sum_{i=1}^n \frac{1}{v_{max,i}} \right] / \Delta_j \log L_X$ , we compute the corresponding uncertainty of  $\phi_j$  based in the Poisson error (Gehrels 1986). For example when  $n_j = 1$ , the upper and lower limits of  $\phi_j$  are  $\phi_j^u = \phi_j \times 3.30/1$  and  $\phi_j^l = \phi_j \times 0.17/1$ , and when  $n_j = 11$ ,  $\phi_j^u = \phi_j \times 14.27/11$  and  $\phi_j^l = \phi_j \times 7.73/11$ . We show  $\phi_j$  vs.  $\log L_X$  in the bottom panel of Fig. 17.

First, we fit the seven LF data points with a single power-law of:

$$\phi(L_X) = \dot{N}_0 \left( \frac{L_X}{L_0} \right)^{-\gamma} \quad (10)$$

For  $L_0 = 10^{43}$  erg s<sup>-1</sup>, we obtained  $\gamma = 1.2 \pm 0.1$ . The best-fit model, shown as an orange line in the bottom panel of Fig. 17, is steeper than the power-law model with  $\gamma = 0.6 \pm 0.2$  present by Sazonov et al. (2021), however, the fit seems to slight over predict the number of low  $L_X$  sources and the number of sources with  $L_X \geq 10^{44.5}$  erg s<sup>-1</sup>.

Next, we describe the luminosity function with a broken (or double) power-law in the form of:

$$\phi(L_X) = \dot{N}_0 \left[ \left( \frac{L_X}{L_{bk}} \right)^{\gamma_1} + \left( \frac{L_X}{L_{bk}} \right)^{\gamma_2} \right]^{-1} \quad (11)$$

Performing a broken power-law fit to the luminosity function (LF) of tidal disruption events (TDEs), with  $-\gamma_1$  representing the faint-end slope,  $-\gamma_2$  the bright-end slope, and  $L_{bk}$  the characteristic break luminosity, we utilize Markov Chain Monte Carlo (MCMC) to obtain  $\gamma_1 = 0.96_{-0.24}^{+0.21}$ ,  $\gamma_2 = 2.65_{-0.90}^{+1.1}$ , and  $\log L_{bk} = 44.1_{-0.5}^{+0.4}$  erg s<sup>-1</sup>. The Bayesian information criterion (BIC) favors the broken power-law fit over the single power-law fit, with a smaller BIC value by 7.1. This suggests that the broken power-law LF provides a superior

description of the data. Notably, our determined  $\gamma_1$  below the break is steeper than the  $\gamma = 0.6 \pm 0.2$  reported by Sazonov et al. (2021), indicating potential underestimation of the low  $L_X$  end or/and overestimation of the high end of the LF in their work. The selection bias in Sazonov et al. (2021)’s criteria, favoring sources with observed flux at least 10 times brighter than the previous upper limit, may contribute to underestimating the low luminosity end. Our findings reveal an extension of the LF to  $L_X$  values below  $10^{42.5}$  erg s<sup>-1</sup> (Sazonov et al. (2021)’s lowest  $L_X$  bin), reaching as low as  $L_X \approx 10^{41}$  erg s<sup>-1</sup>. This suggests a sizable population of X-ray-emitting TDEs that are too faint for current instruments unless occurring at very low redshifts, emphasizing that the absolute rate estimated by Sazonov et al. (2021) represents a lower limit on the rate of X-ray-emitting TDEs.

In the case that the X-ray luminosity of TDEs are Eddington limited, and hence their fraction  $l_x = L_X/L_{Edd}$  is  $< 1$ , the observed suppression of the TDE rate at  $M_{BH} > 10^8 M_\odot$  (van Velzen 2018; Yao et al. 2023b) can naturally explain the break in the X-ray LF at  $\sim 10^{44}$  erg s<sup>-1</sup>. Indeed, based on such arguments, Mummery (2021) estimated a *maximum* X-ray luminosity of  $\sim 10^{44}$  erg s<sup>-1</sup> for non-jetted TDEs<sup>10</sup>. Although a couple TDEs have shown a peak  $L_X > 10^{44}$  erg s<sup>-1</sup> (see top panel of Fig. 17), the steep break, from  $\gamma \approx 1.0$  to  $\gamma \approx 2.7$  in the LF is still in qualitative agreement with the limiting luminosity expectation, given that a TDE with peak  $L_X = 10^{45}$  erg s<sup>-1</sup> should be  $\sim 1000$  times rarer than a TDE with peak  $L_X = 10^{44}$  erg s<sup>-1</sup>.

## 5. DISCUSSION

### 5.1. On the diversity of X-ray evolution: delayed accretion or variable optical depth? an orientation effect?

As we have shown in §4.1, optically selected TDEs have a large diversity in X-ray evolution, with sources rarely showing prompt ( $\Delta t \leq 100$  days) bright ( $L_X \geq 10^{43}$  erg s<sup>-1</sup>) X-ray emission that decays as a power-law with time as predicted from simple fallback accretion models. Instead, most sources show a faint X-ray emission at early times, with a subset showing a delayed increase in the observed X-ray luminosity, while others showing a faint and approximately constant X-ray luminosity during the UV/optical evolution.

<sup>10</sup> TDEs in which the jet is pointed towards us – so-called jetted or relativistic TDEs – have their luminosity beamed, hence those can reach  $L_X \geq 10^{47}$  erg s<sup>-1</sup>. This is a distinct physical scenario, than what is discussed in this section, therefore are not considered.

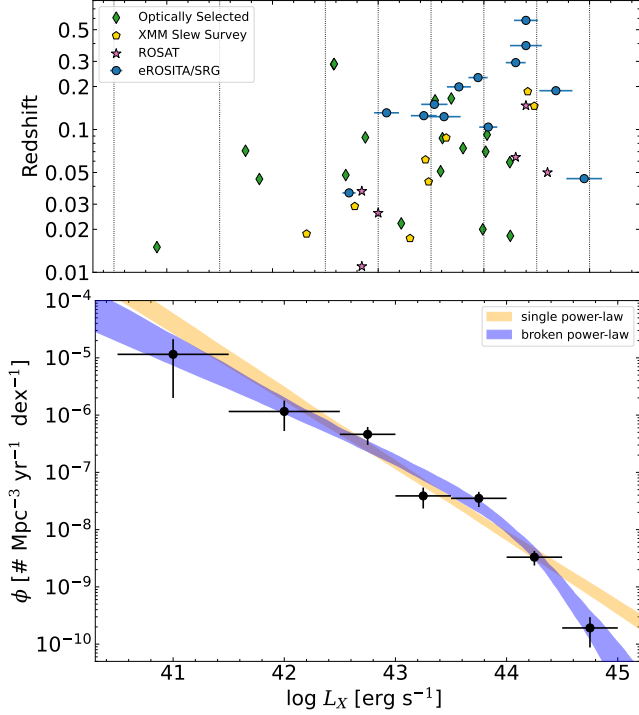


**Figure 17.** Top: Distribution of Redshift  $\times$  peak X-ray luminosity ( $L_X$ ) for all the sources included in the X-ray luminosity function analyses. Bottom: Derived luminosity function (black points), best-fitted single power-law (orange), best-fitted broken power-law (blue).

From our X-ray spectral and SED analyses, a number of conclusions can be drawn:

- The X-ray emission temperature ( $T_p$ ) decreases with time (see Fig. 8);
- The decrease in  $T_p$  is independent of the  $L_X$ , given that *Late-time brightening* sources show highest  $T_p$  at early times, when the  $L_X$  is minimum.
- This independent  $T_p$  and  $L_X$  evolution creates a decoupling between the two parameters in these epochs/sources. Other epochs/sources show a  $L_X \propto T^\alpha$  relation (see Fig. 9).
- The highest  $T_p$  with lowest  $L_X$  results in an unphysical value for the X-ray emission radius ( $R_p/R_g$ ) for these source/epochs. For other epochs/epoch  $R_p$  is consistent with  $R_{ISCO}$  (see Fig. 10).
- The epochs with unphysical  $R_p/R_g$  are also the epochs in which UV/optical to X-ray ratio ( $L_{BB}/L_X$ ) is too high to be produced by *bare/unreprocessed* accretion disk (see Fig. 11).
- There is a large range of observed  $L_{BB}/L_X$  values at early times ( $0.5 \leq L_{BB}/L_X \leq 3000$ ); at late

times these values converge to ( $0.5 \leq L_{BB}/L_X < 10$ ), see Fig. 14.

- There is no  $M_{BH}$  dependence on the presence/absence of luminous X-ray emission ( $L_X \geq 10^{42}$  erg s $^{-1}$ ).

Viable theoretical models for the TDE emission mechanism must be able to reproduce these observational findings.

A possible explanation for the late-time brightening of the X-ray emission, put forward by several authors (e.g., Gezari et al. 2017; Liu et al. 2022), is the delayed formation of the accretion disk in these sources. Some problems arise from this interpretation:

*i)* soft X-ray emission (though faint,  $L_X \leq 10^{42}$  erg s $^{-1}$ ) is detected in the early times for all of the *late-time brightening* sources in which an observation deep enough to detect such faint emission is available<sup>11</sup>; which means that the structure responsible for X-ray emission in these sources is already present at very early times, i.e. is promptly formed;

*ii)* the temperature of these X-ray faint phases are as high or higher than the temperatures at the late-time; *iii)* the overall evolution of the temperature is consistent with a cooling accretion disk (see Fig. 8), that would not necessarily be the case if the late time X-ray emission is tracing a different physical structure (disk) than the early time is tracing (stream-stream shocks), like proposed by Liu et al. (2022);

*iv)* if the presence of bright X-ray emission ( $L_X > 10^{42}$  erg s $^{-1}$ ) is driven by the successful circularization of the debris streams, while in sources with  $L_X \leq 10^{42}$  erg s $^{-1}$  these do not circularize to form a disk; there should be a distinct  $M_{BH}$  distribution underlying the two populations – given the strong  $M_{BH}$  dependence in the circularization time (Bonnerot et al. 2016) – as we have shown in Fig. 16, there is not difference in their  $M_{BH}$  distribution.

As we argued in §4.2, the observed properties seems to point towards the presence of prompt, but suppressed, X-ray emission in the early times of the *Late-time brightening* and *X-ray faint* sources. Suppression of the X-ray emission is an expected consequence of different TDE models that invoke the reprocessing of the high energy emission into the UV/optical wavelengths by an optionally thick material, these models (e.g., Loeb & Ulmer 1997; Ulmer 1999; Coughlin & Begelman 2014; Metzger & Stone 2016; Roth et al. 2016; Dai et al. 2018; Thomsen et al. 2022; Parkinson et al. 2022; Metzger 2022),

<sup>11</sup> The upper limits on AT2020ksf and OGLE16aa are higher than  $10^{42}$  erg s $^{-1}$ , the two are also the highest redshift sources.

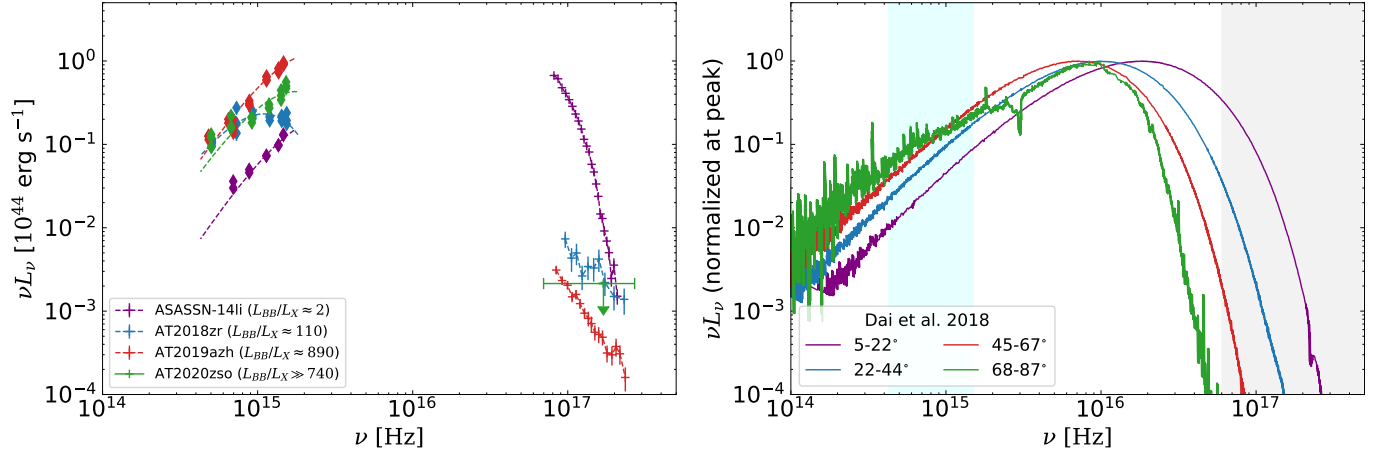


**Figure 18.** Comparison between observed SEDs and model SEDs by Dai et al. (2018). In the right we show the early time (near UV/optical peak) observed SED for ASASSN14-li, AT2018zr and AT2019azh (this work) as well as for AT2020zso (Wevers et al. 2022), showing a large range of  $L_{\text{BB}}/L_{\text{X}}$  values. The left panels show Dai et al. (2018)’s early time simulated SEDs as seen by distinct viewing angles from the disk pole: face-on =  $0^\circ$  and edge-on =  $90^\circ$ .

assume different physical processes and geometries, but have the common property of the reprocessing of the X-ray emission at the highest accretion rates, i.e., early times, and its re-emission at lower energies. Although a large fraction of the optical TDEs in our sample shows suppression of the X-ray emission at early times, some do not, namely, ASASSN-14li, AT2019vcb, AT2019dsg, and AT2019ehz; this is also true for most X-rays discovered TDEs (comparison between these populations will be presented in §5.4). Instead, there is an at least three orders of magnitude range in observed  $L_{\text{BB}}/L_{\text{X}}$  at early times (see Fig. 14, and 15). Some of this diversity was already previously known and had inspired a series of models where the presence/absence of strong reprocessing is orientation dependent (e.g., Dai et al. 2018; Jonker et al. 2020; Thomsen et al. 2022).

In these models, the optical depth through the line-of-sight for the high energies photons has a strong dependence on the accretion rate and likely on the viewing angle, at the highest accretion rate, i.e., early times, if the source is seen at lower inclination angles with respect to the disk pole, the optical depth ( $\tau$ ) and hence the reprocessing, are minimal, and the observed SED resembles the one of the underlying disk (i.e.,  $L_{\text{BB}}/L_{\text{X}} \lesssim 10$ , see Appendix §B), which would explain the *power-law decaying* sources. At the largest inclination angles (towards edge-on), the system should be heavily optically thick ( $\tau \gg 10$ ) to the X-rays which should be reprocessed to the lower energies, making the X-rays undetectable, and high lower limits on  $L_{\text{BB}}/L_{\text{X}}$  to be measured. This should explain the TDE population with UV/optical emission only. When seen at intermediate angles, the system is not completely optically thick, but the optical depth is still important ( $\tau \sim \text{few}$ ), and

only a small fraction of the X-ray can escape unprocessed; the SED is then UV/optical dominated ( $L_{\text{BB}}/L_{\text{X}}$  between  $\text{few} \times 10^1$  to  $\text{few} \times 10^3$ ), but faint X-ray emission is still able to escape and be detected; as the accretion rate decreases, the optical depth of the system decreases, allowing for a larger fraction of the X-ray photons to escape, which would explain the *Late-time brightening* sources (Thomsen et al. 2022), and perhaps the *X-ray faint* sources given some fine tuning in the evolution of the parameters.

In the left panel of Fig. 18, we show four early-time SEDs with a diverse range of  $L_{\text{BB}}/L_{\text{X}}$  values, while in the right panel, we show the four simulated SEDs for distinct inclination angles as presented by Dai et al. (2018). A direct comparison is, of course, not valid, given that in Dai et al. (2018) models, the only parameter changed between the SEDs is the viewing angle towards the system; every other parameter of the system is fixed, while in reality, our four example sources/SEDs may have distinct black hole masses, black hole spin, impact parameter ( $\beta$ ), peak disk temperature, radial profile of the disk temperature and many other differences, that could also shape the SED, however, it is interesting to note that the large diversity of  $L_{\text{BB}}/L_{\text{X}}$  observed can be, in principle, produce just by a change in viewing angle.

This scenario seems to be able to explain several of the observed properties:

- i)* The large range of  $L_{\text{BB}}/L_{\text{X}}$  values at early times, and the convergence to disk-like values at late times;
- ii)* The diversity of X-ray light curves, including the suppressed (but still detected) prompt X-ray emission from the *Late-time brightening* and *X-ray faint* sources;
- iii)* The lack of  $M_{\text{BH}}$  dependence on the presence/absence of luminous X-ray emission.

As we pointed out in §4.2, an important characteristic of the early suppression of the X-ray emission in the *late-time brightening* and *X-ray faint* sources is that such suppression seems to have minimal effect in the measured  $T_p$ , given that the expected decline in temperature is still observed,  $T_p$  is the highest at early time and decay at late times. This would mean that although a large fraction of the X-rays are absorbed by this reprocessing-layer of ionized gas<sup>12</sup>, the output spectrum seems to have a similar temperature (shape) of the supposed underlying emitted spectrum. This would require the absorption and re-emission process to have a ‘*quasi-grey*’ net effect in the X-ray 0.3-2.0 range. Such effect is, however, quite hard to be produced, for example, in Thomsen et al. (2022)’s simulations the early time output X-ray temperature can be up to  $\sim 50\%$  colder than the injected spectrum, depending on the viewing angle and the ionization state of the gas. This effect does not seem to be present – given the observed decline of  $T_p$  with time for all classes of sources – although the temperature of the underlying emission is, of course, not accessible for a direct comparison. Alternatively, if in these sources, the absorbing material is heavily optically thick but clumpy or has small holes so that a fraction of the source X-rays can get through unprocessed, then this could explain the apparent suppression of the observed X-ray emission – given the inferred disk radius would be reduced by a factor of the square root of the transmitted over emitted fluxes – while the emerging temperature would not be strongly modified (Takeuchi et al. 2013; Kobayashi et al. 2018; Yao et al. 2022). Independently of the driven mechanism, the X-ray emitting structure (consistent with an accretion disk) is promptly formed even in those sources showing a late-time brightening, and their early-time emission seems to point towards a partial absorption/reprocess scenario.

The *flaring* source, AT2019ehz, has not been addressed yet; we first note that such short term flaring differs from the gradual late time X-ray increase of the *late-time brightening* sources, the reprocessing scenario does not work in this case, given that this system is bright at early times, fade, and then re-brighten, which would disagree with the net brightening predicted under the reprocessing scenario. Furthermore, the flaring behavior is accompanied by an increase in  $T_p$ , a relation between  $T_p$  and  $L_X$  is present (interestingly with

the highest best-fitted  $\alpha$  for a  $L_X \propto T^\alpha$  relation), and no large variations in  $R_p$  is observed, with  $R_p/R_g$  always in the physically valid range. This behavior differs from the other sources with early X-ray faint emission – as extensively discussed above – and instead points towards a disk seen directly without much reprocessing, but with intrinsic variability.

One possibility is that X-ray variability is produced by random short term fluctuations in the peak disk temperature (Mummery & Balbus 2022). Alternatively, the nascent accretion disk may be initially misaligned with respect to the MBH’s spin axis, which would induce relativistic torques on the disk and causes it to precess (Lense-Thirring precession), producing repeating flares, that should also modulated the observed  $T_p$  (Stone & Loeb 2012; Franchini et al. 2016; Pasham et al. 2024). In this scenario relativistic torque effects aligns the disk and terminates precession and the flares; the flares are indeed not observed at late times in AT2019ehz, although the cadence of observation is not enough to confirm this. In both cases, a short term decoupling between the hotter (X-ray) and colder (UV/optical) emission regions, as observed, would be expected.

A definitive explanation for the flaring behavior of AT2019ehz is not within the scope of this work, it may not be possible at all, given the cadence/quality of the available data. A TDE discovered in 2022 (Yao & Gezari 2022) has shown similar flaring behavior, for that source the cadence of the observations is much higher (several per day for hundreds of days), and distinct models for the flaring behavior will be tested in a forthcoming study (Yao, Guolo, et al. in prep).

## 5.2. On the large population of X-ray quiet TDEs

As we have shown in §4.5, most (up to 60%) discovered by optical surveys are X-ray quiet ( $L_X \leq 10^{42}$  erg s<sup>-1</sup>), the definitive picture for why that is the case is beyond the scope of this paper. However, a couple of insights can be made.

First, TDEs with detectable X-ray emission, but having  $L_X \leq 10^{42}$  erg s<sup>-1</sup> do exist, as we have demonstrated, and should be common given: *i*) the derived LF (see §4.6), *ii*) the possible orientation effects (see §5.1) that should make a large fraction of X-ray emission to be absorbed.

However, such X-ray luminosities can hardly be observed unless the TDE happens at extremely low redshifts. Even with a modest  $\sim 20$  ks *XMM-Newton* observation upper-limits of  $L_X \approx 10^{41}$  erg s<sup>-1</sup> can rarely be placed for the typical redshift range in which TDEs are observed (see the  $L_X$  upper limits for the non-detected TDE in Table 2). Sometimes these sources show a

<sup>12</sup> The absorption by an ionized gas should not be confused with absorption by a neutral medium (modeled, e.g., by the TBabs in xspec) has a strong energy dependence in the soft X-rays, while (partially) ionized gas absorption, in contrast, has a higher optical depth in the hard X-rays (Thomsen et al. 2022).



strong late-time X-ray rebrightening, but not always (e.g., AT2018zr, AT2018hyz, and AT2019qiz); besides, if a TDE is not detected at early times – which for  $L_X \leq 10^{42}$  erg s $^{-1}$  only occurs for the nearest sources – it is unlikely that this source will continue to be followed-up by an X-ray instrument, much less by *XMM-Newton*.

Furthermore, to be able to produce observable radiation in the 0.3-2 keV range from an accretion disk, the inner temperature ( $T_p$ ) must necessarily be  $\geq 10^{5.1} - 10^{5.2}$  K, since at lower peak temperatures the emission is shifted entirely to the extreme UV.

For a Galactic like gas-to-dust ratio ( $N_H = 5.5 \times 10^{21} \times E(B-V)$ ), soft X-rays are more absorbed than UV light. For instance, with  $N_H = 5 \times 10^{20}$  cm $^{-2}$  ( $E(B-V) = 0.09$ ), about 74% of 0.3 keV X-rays get absorbed, while only 42% of 2600 Å UV light is. With higher absorption of  $N_H = 1 \times 10^{21}$  cm $^{-2}$  ( $E(B-V) = 0.18$ ), 93% of X-rays and 67% of UV are absorbed<sup>13</sup>. Therefore, soft X-rays photons are more affected by absorption along our line of sight than UV photons, making them harder to detect given same emitted flux. See for example the cases of AT2021mhg, AT2021sdu and AT2021yte in §4.5.

Finally, it is still possible that the circularization of the stellar debris does not happen, and no accretion disk is formed in these sources. In contrast, another process, independent of accretion, such as shocks produced by the intersection between the streams, would be responsible for all the UV/optical emission. Although it is not clear why the proposed lack of circularization is not dependent on  $M_{BH}$ , see Fig. 16.

The combination of the effects mentioned above is likely to be able to explain the large fraction of optically discovered TDE with no observable X-ray emission.

### 5.3. On the bolometric luminosity of TDEs

As pointed out by several authors (e.g., Dai et al. 2018; Lu & Kumar 2018; Thomsen et al. 2022; Mummery et al. 2023) a ‘missing energy’ problem (Piran et al. 2015) will only arise when the integrated UV/optical (fitted with a blackbody function) is incorrectly considered as the bolometric luminosity of the TDE. This is an obvious statement for the sources with detected X-ray emission (see Fig. 3), but should also be true for those in which X-ray emission is not detected, since the bulk of the TDE emission should be emitted in the extreme UV (EUV) bands (see right panel of Fig. 18) which is not adequately modeled by the single temperature blackbody

assumption for the UV/optical emission (see also right panel of Figure 5 in Dai et al. 2018).

When the full SED is consistent with a *bare/unreprocessed* accretion disk, i.e., the extrapolated disk model fitted from the X-rays matches the observed UV/optical (usually when  $L_{BB}/L_X < 10$ , see ASASSN-14li and late-time AT2019azh panel in Fig. 15), the bolometric luminosity can be computed simply by integration over the disk SED.

We note, however, that if a *bare/unreprocessed* disk SED is assumed in cases where there is X-ray suppression, e.g., early-times of AT2019azh or AT2018zr, where  $L_{BB}/L_X \gg 100$ , the resulting SED will be based on an unphysical normalization ( $R_p/R_g \leq 0.3$ ) and hence will underestimate the true bolometric luminosity, even if considering the ‘disk bolometric luminosity’.

For the cases – usually at early times – in which the strong UV/optical excess (i.e.,  $L_{BB}/L_X > 100$ ) is present (see again right panel of Fig. 18) the SED shape is strongly dependent on the radiative processes involved, and have large uncertainties because of the lack of constraints in the unobservable EUV waveband.

### 5.4. On the unification of the TDE population: survey selection biases and the lack of an optical/X-ray dichotomy

As we have shown, optical surveys can discover TDEs with a large range of  $L_{BB}/L_X$  at early times, as we argue in §5.1 some (if not most) of this diversity can be explained by the viewing angle towards the system. We would like to compare the TDEs discovered by optical surveys and by X-ray surveys to look for differences (or lack thereof) in these populations and, if present, what could drive such differences.

TDEs discovered by most X-ray missions (e.g., *ROSAT* and *XMM-Newton* Slew Survey) had very little to no real-time UV/optical follow-up; hence accessing their  $L_{BB}/L_X$  ratio is not possible. We thus focused our analyses on the more recent sources discovered by *SRG/eROSITA*, in particular the 13 TDEs presented Sazonov et al. (2021) and eRASSt J074426.3 +291606 (hereafter J0744) presented by Malyali et al. (2023). Unfortunately, the sources presented in Sazonov et al. (2021) had no UV follow-up, but some constraints on the optical emission from ground-based optical time-domain surveys were obtained.

As reported by Sazonov et al. (2021), all of their sources had  $L_g/L_X$ <sup>14</sup> ratios lower than 0.3. For a typical UV/optical blackbody temperature of 20,000 K (Ham-

<sup>13</sup> For this calculation a standard Wilms et al. (2000) abundance was assumed for the X-ray absorption, using *TBabs*, while the UV extinction was based on Calzetti et al. (2000) law.

<sup>14</sup> Where  $L_g$  is the optical  $g$ -band luminosity.



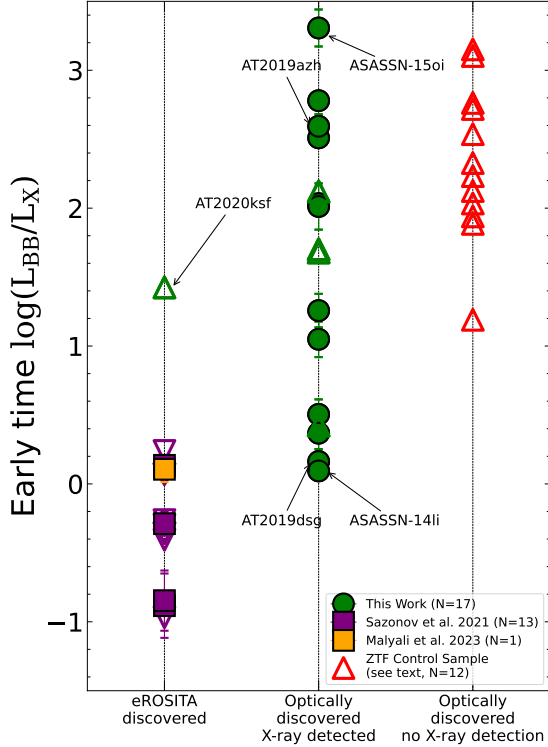


**Figure 19.** Distribution of early time  $L_{BB}/L_X$  based on discovery wavelength/survey. Extreme sources are marked with arrow. Triangles are lower limits on  $L_{BB}/L_X$  (i.e., no X-ray detection), inverse triangles are an upper limit on  $L_{BB}/L_X$  (i.e., no UV/optical detection), filled markers represent detections in both UV/optical and X-rays. Color represent distinct samples or references. Sources with extreme values are marked with arrows. There is a continuous and wide distribution of  $L_{BB}/L_X$  values, instead of a clear dichotomy between optically and X-ray discovered TDEs.

merstein et al. 2023a), this translates into  $L_{BB}/L_X \leq 3$ . Such values, however, do not mean that these sources were ‘X-ray only’. For example, the early time  $L_{BB}/L_X$  of ASASSN-14li and AT2019dsg were also lower than 3. This is also true for J0744, which had  $L_{BB}/L_X \approx 2$  at early times. Most of the sources in Sazonov et al. (2021) had no optical counterpart detection, given the relatively high redshift range of their sample (all but one have  $z > 0.1$ , compare with our sample, in Table 1), ground-based optical surveys are not sensitive enough to detect the typical optical TDE luminosities at these redshifts. For the sources with detected optical counterparts, the range of  $L_{BB}/L_X$  was  $\sim 0.1 \leq L_{BB}/L_X \leq 2$ . As discussed in §5.1, for these values of  $L_{BB}/L_X$ , no UV/optical excess is necessarily present; the shape of the SED shape is fully consistent with an *bare/unreprocessed* accretion disk; hence these systems are likely to be seen at lower angles (i.e., towards face-on orientations), similar to ASASSN-14li and AT2019dsg. The small varia-

tions observed in the  $L_{BB}/L_X$  can be fully explained by a range of values of  $T_p$ , that as shown in appendix §B can produce  $L_{BB}/L_X$  as low as  $\sim 0.05$  for the range of  $T_p$  found in TDEs.

The distribution of  $L_{BB}/L_X$  at early times for sources discovered by distinct methods/surveys is presented in Fig. 19. Triangles are lower limits on  $L_{BB}/L_X$  (i.e., no X-ray detection), inverse triangles are an upper limit on  $L_{BB}/L_X$  (i.e., no UV/optical detection), filled markers represent detections in both UV/optical and X-rays. In Fig. 20 we show the peak  $L_{BB}$  vs. the early time  $L_X$ , where the distinct symbols shows: *SRG/eROSITA* (squares) TDEs, optically selected X-ray detected (circles) and optically selected with no X-ray detection (diamond); filled marker show detection in both optical/UV (y-axis) and X-ray (x-axis), while hollow markers either UV/optical or X-rays (at early times) were no detected, similarly to Fig.19 distinct color represents the different references.

From Fig. 19, it is clear that there is no obvious dichotomy between optical and X-ray discovered TDEs. Instead, there is a continuous distribution of  $L_{BB}/L_X$  values at early times, that is at least as wide as  $L_{BB}/L_X \in (0.1, 32000)$ . This can be explained by the fact that surveys at distinct wavelengths will be biased to discover sources that are brightest in that wavelength range. Optical surveys will discover mostly sources with high  $L_{BB}/L_X$ , up to 60% of which with  $L_X \leq 10^{42}$  erg s $^{-1}$  (see §4.5), but will still sometimes discover sources with lower  $L_{BB}/L_X$ , such as ASASSN-14li and AT2019dsg. X-ray surveys, on the other hand, will most likely discover sources with lower  $L_{BB}/L_X$ , but not always; AT202ksf, for example, had no X-ray detection at early times ( $L_{BB}/L_X \geq 25$ ), was not identified in real-time as a TDE candidate by optical surveys, and later ( $\Delta t \sim 200$  days) was discovered by *SRG/eROSITA* following its X-ray brightening. The same holds for their distribution in  $L_{BB} \times L_X$  plane of Fig. 20, there is a continuous distribution of the X-ray and UV/optical selected populations, instead of clear dichotomy between them.

An *unbiased*<sup>15</sup> discovery of TDEs would be possible with either: *i*) the simultaneous operation of an wide field-of-view (FoV) X-ray survey telescope with UV follow-up capabilities (e.g., STAR-X, Hornschemeier et al. 2023) and a wide FoV optical survey (e.g LSST, Ivezić et al. 2019), *ii*) or the simultaneous and coordinated operation of an wide FoV UV survey telescope

<sup>15</sup> This is still biased towards dust free host galaxies, for heavily dust obscured TDEs the UV/optical and soft X-ray are absorbed and re-emitted in the infrared, see for example Panagiotou et al. (2023) and Masterson et al. (2024).

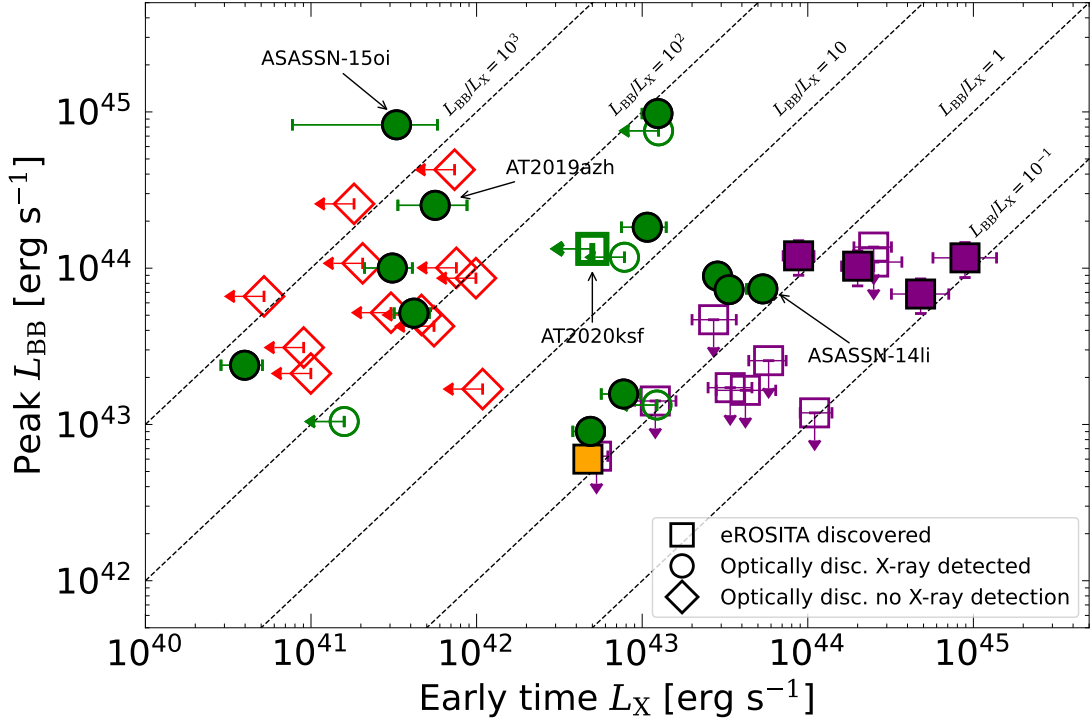


**Figure 20.** Distribution of peak  $L_{\text{BB}} \times$  early time  $L_{\text{X}}$  for different TDE populations. Squares show *SRG*/eROSITA (X-ray) discovered sources, circles show optically discovered X-ray detected, while diamonds show optically discovered with no X-ray detection. Filled markers represent detections in both UV/optical and X-rays (early times), while hollow symbols represent upper limits in one of the two wavelength bands, where the arrows represent their  $3\sigma$  upper limit. The colors are the same as in Fig. 19.

(e.g., ULTRASAT and/or UVEX, Sagiv et al. 2014; Kulkarni et al. 2021) and wide FoV X-ray survey telescope (e.g., *SRG*/eROSITA and/or *Einstein Probe*, Sunyaev et al. 2021; Yuan et al. 2022).

## 6. CONCLUSIONS

We have analyzed the *XMM-Newton* and *Neil Gehrels Swift Observatory* X-ray and broad-band UV/optical emission of 17 optically selected X-ray detected TDEs discovered between 2014 and December 2021; we also compare our sample with the samples of optically discovered X-ray quiet TDEs and X-ray discovered TDEs, our main conclusions are:

- The X-ray light curves show a large diversity, with sources rarely showing a power-law decay and a large fraction showing a late-time brightening.
- The X-ray spectra are extremely soft in most sources and epochs, easily distinguishable from AGN X-ray spectra.
- The overall behavior of the measured radius (normalization) and temperature (shape) resulting from the X-ray spectral fitting is in agreement with that expected for the innermost region of a newly

formed and time-evolving accretion disk, including the cooling of the peak temperature and a radius (in most cases) consistent with innermost stable orbit.

- Sources with early-time faint X-ray emission show an unphysical radius for the X-ray emission at these epochs, while their temperature behaves as expected, indicating the apparent suppression/absorption of their intrinsic early X-ray emission.
- The spectral energy distribution (SED) shape, as probed by the ratio ( $L_{\text{BB}}/L_{\text{X}}$ ) between the UV/optical and X-ray luminosities, has a large range of values  $L_{\text{BB}}/L_{\text{X}} \in (0.5, 3000)$  at early times, at late times the range converges to disk-like values,  $L_{\text{BB}}/L_{\text{X}} \in (0.5, 10)$ , for all sources.
- The combined X-ray spectral and SED properties and evolution favors a change in the optical depth (thick  $\rightarrow$  thin) for the high energies photons through the line-of-sight, instead of the delayed formation of the accretion disk, in order to explain the late-time brightening observed in some sources.

- Three sources show a soft  $\rightarrow$  hard X-ray spectral transition, indicative of the formation of a hot corona akin to active galaxies, with the state transitions occurring at least 200 days after the UV/optical peak, but it is not sustained for more than a couple of months.
- We estimated that the fraction of optically discovered TDEs that are X-ray loud, with  $L_X \geq 10^{42}$  erg s $^{-1}$ , is at least 40% and that X-ray loudness is not dependent on  $M_{\text{BH}}$ .
- We show that the TDE X-ray luminosity function from  $10^{41} - 10^{45}$  erg s $^{-1}$  has a broken-power-law shape in the form of  $dN/dL_X \propto L_X^{-1.0 \pm 0.2}$  at  $L_X < L_{bk}$  and  $dN/dL_X \propto L_X^{-2.7 \pm 1.0}$  at  $L_X \geq L_{bk}$  with break luminosity of  $\log(L_{bk}) = 44.1^{+0.3}_{-0.5}$  erg s $^{-1}$ . Revealing a large population of TDE with  $L_X \leq 10^{42}$  erg s $^{-1}$  (and high  $L_{\text{BB}}/L_X$ ), for which the X-ray emission can not be detected with current instruments unless occurs at very low  $z$ .
- We show that there is no dichotomy between optical and X-ray discovered TDEs, and instead there is a continuous range of early time  $L_{\text{BB}}/L_X$ , at least as wide as  $L_{\text{BB}}/L_X \in (0.1, 3000)$ , with X-ray/optical surveys discovering preferentially, but not exclusively, from the lower/higher portion of the distribution, in agreement with unification models for the overall TDE population.

1 *Acknowledgments* – M.G. thanks T. Wevers, J. Kro-  
 2 lik, P. Jonker and E. Coughlin for comments, sugges-  
 3 tions and discussions. M.G. and S.G. are supported  
 4 in part by NASA XMM-Newton grants 80NSS23K0621  
 5 and 80NSSC22K0571. Y. Y. acknowledges support by  
 6 NASA XMM-Newton grant 80NSSC23K0482. E.H. ac-  
 7 knowledges support by NASA under award number  
 8 80GSFC21M0002. This work is based on observations  
 9 obtained with the Samuel Oschin Telescope 48-inch and  
 10 the 60-inch Telescope at the Palomar Observatory as  
 11 part of the Zwicky Transient Facility project. ZTF  
 12 is supported by the National Science Foundation un-  
 13 der grant No. AST-2034437 and a collaboration in-  
 14 cluding Caltech, IPAC, the Weizmann Institute of Sci-  
 15 ence, the Oskar Klein Center at Stockholm Univer-  
 16 sity, the University of Maryland, Deutsches Elektronen-  
 17 Synchrotron and Humboldt University, the TANGO  
 18 Consortium of Taiwan, the University of Wisconsin at  
 19 Milwaukee, Trinity College Dublin, Lawrence Livermore  
 20 National Laboratories, IN2P3, University of Warwick,  
 21 Ruhr University Bochum, and Northwestern Univer-  
 22 sity. Operations are conducted by COO, IPAC, and  
 23 UW. The ZTF forced-photometry service was funded  
 24 under the Heising-Simons Foundation grant #12540303  
 25 (PI: Graham). This work has made use of data from  
 26 the Asteroid Terrestrial-impact Last Alert System (AT-  
 27 LAS) project. The Asteroid Terrestrial-impact Last  
 28 Alert System (ATLAS) project is primarily funded to  
 29 search for near earth asteroids through NASA grants  
 30 NN12AR55G, 80NSSC18K0284, and 80NSSC18K1575.  
 31 This work made use of data supplied by the UK Swift  
 32 Science Data Centre at the University of Leicester.

*Software:* `astropy` (Astropy Collaboration et al. 2013), `emcee` (Foreman-Mackey et al. 2013), `heasoft` (Heasarc 2014), `matplotlib` (Hunter 2007), `Prospector` (Johnson et al. 2021), `scipy` (Virtanen et al. 2020), `xspec` (Arnaud 1996).

*Facilities:* XMM, Swift, eROSITA, PO:1.2m., OGLE.

## REFERENCES

- Agol, E., & Krolik, J. H. 2000, *ApJ*, 528, 161,  
doi: [10.1086/308177](https://doi.org/10.1086/308177)
- Alexander, K. D., Berger, E., Guillochon, J., Zauderer, B. A., & Williams, P. K. G. 2016, *ApJL*, 819, L25,  
doi: [10.3847/2041-8205/819/2/L25](https://doi.org/10.3847/2041-8205/819/2/L25)
- Arnaud, K. A. 1996, in *Astronomical Society of the Pacific Conference Series*, Vol. 101, *Astronomical Data Analysis Software and Systems V*, ed. G. H. Jacoby & J. Barnes, 17
- Astropy Collaboration, Robitaille, T. P., Tollerud, E. J., et al. 2013, *A&A*, 558, A33,  
doi: [10.1051/0004-6361/201322068](https://doi.org/10.1051/0004-6361/201322068)
- Bade, N., Komossa, S., & Dahlem, M. 1996, *A&A*, 309, L35
- Balbus, S. A., & Hawley, J. F. 1991, *ApJ*, 376, 214,  
doi: [10.1086/170270](https://doi.org/10.1086/170270)
- Blagorodnova, N., Gezari, S., Hung, T., et al. 2017, *ApJ*, 844, 46, doi: [10.3847/1538-4357/aa7579](https://doi.org/10.3847/1538-4357/aa7579)
- Blagorodnova, N., Neill, J. D., Walters, R., et al. 2018, *PASP*, 130, 035003, doi: [10.1088/1538-3873/aaa53f](https://doi.org/10.1088/1538-3873/aaa53f)
- Blagorodnova, N., Cenko, S. B., Kulkarni, S. R., et al. 2019, *ApJ*, 873, 92, doi: [10.3847/1538-4357/ab04b0](https://doi.org/10.3847/1538-4357/ab04b0)
- Bonnerot, C., Rossi, E. M., & Lodato, G. 2017, *MNRAS*, 464, 2816, doi: [10.1093/mnras/stw2547](https://doi.org/10.1093/mnras/stw2547)
- Bonnerot, C., Rossi, E. M., Lodato, G., & Price, D. J. 2016, *MNRAS*, 455, 2253, doi: [10.1093/mnras/stv2411](https://doi.org/10.1093/mnras/stv2411)
- Bright, J. S., Fender, R. P., Motta, S. E., et al. 2018, *MNRAS*, 475, 4011, doi: [10.1093/mnras/sty077](https://doi.org/10.1093/mnras/sty077)
- Brown, G. C., Levan, A. J., Stanway, E. R., et al. 2017, *MNRAS*, 472, 4469, doi: [10.1093/mnras/stx2193](https://doi.org/10.1093/mnras/stx2193)
- Burrows, D. N., Hill, J. E., Nousek, J. A., et al. 2005, *SSRv*, 120, 165, doi: [10.1007/s11214-005-5097-2](https://doi.org/10.1007/s11214-005-5097-2)

- Calzetti, D., Armus, L., Bohlin, R. C., et al. 2000, *ApJ*, 533, 682, doi: [10.1086/308692](https://doi.org/10.1086/308692)
- Cannizzaro, G., Wevers, T., Jonker, P. G., et al. 2021, *MNRAS*, 504, 792, doi: [10.1093/mnras/stab851](https://doi.org/10.1093/mnras/stab851)
- Cannizzo, J. K., Lee, H. M., & Goodman, J. 1990, *ApJ*, 351, 38, doi: [10.1086/168442](https://doi.org/10.1086/168442)
- Cash, W. 1979, *ApJ*, 228, 939, doi: [10.1086/156922](https://doi.org/10.1086/156922)
- Cenko, S. B., Krimm, H. A., Horesh, A., et al. 2012, *ApJ*, 753, 77, doi: [10.1088/0004-637X/753/1/77](https://doi.org/10.1088/0004-637X/753/1/77)
- Cenko, S. B., Cucchiara, A., Roth, N., et al. 2016, *ApJL*, 818, L32, doi: [10.3847/2041-8205/818/2/L32](https://doi.org/10.3847/2041-8205/818/2/L32)
- Chornock, R., Berger, E., Gezari, S., et al. 2014, *ApJ*, 780, 44, doi: [10.1088/0004-637X/780/1/44](https://doi.org/10.1088/0004-637X/780/1/44)
- Conroy, C., Gunn, J. E., & White, M. 2009, *ApJ*, 699, 486, doi: [10.1088/0004-637X/699/1/486](https://doi.org/10.1088/0004-637X/699/1/486)
- Coughlin, E. R., & Begelman, M. C. 2014, *ApJ*, 781, 82, doi: [10.1088/0004-637X/781/2/82](https://doi.org/10.1088/0004-637X/781/2/82)
- Dai, L., McKinney, J. C., Roth, N., Ramirez-Ruiz, E., & Miller, M. C. 2018, *ApJL*, 859, L20, doi: [10.3847/2041-8213/aab429](https://doi.org/10.3847/2041-8213/aab429)
- Done, C., Davis, S. W., Jin, C., Blaes, O., & Ward, M. 2012, *MNRAS*, 420, 1848, doi: [10.1111/j.1365-2966.2011.19779.x](https://doi.org/10.1111/j.1365-2966.2011.19779.x)
- Evans, P. A., Beardmore, A. P., Page, K. L., et al. 2007, *A&A*, 469, 379, doi: [10.1051/0004-6361:20077530](https://doi.org/10.1051/0004-6361:20077530)
- . 2009, *MNRAS*, 397, 1177, doi: [10.1111/j.1365-2966.2009.14913.x](https://doi.org/10.1111/j.1365-2966.2009.14913.x)
- Fabian, A. C., Zoghbi, A., Ross, R. R., et al. 2009, *Nature*, 459, 540, doi: [10.1038/nature08007](https://doi.org/10.1038/nature08007)
- Foreman-Mackey, D., Hogg, D. W., Lang, D., & Goodman, J. 2013, *Publications of the Astronomical Society of the Pacific*, 125, 306, doi: [10.1086/670067](https://doi.org/10.1086/670067)
- Franchini, A., Lodato, G., & Facchini, S. 2016, *MNRAS*, 455, 1946, doi: [10.1093/mnras/stv2417](https://doi.org/10.1093/mnras/stv2417)
- French, K. D., Wevers, T., Law-Smith, J., Graur, O., & Zabludoff, A. I. 2020, *SSRv*, 216, 32, doi: [10.1007/s11214-020-00657-y](https://doi.org/10.1007/s11214-020-00657-y)
- Gabriel, C., Denby, M., Fyfe, D. J., et al. 2004, in *Astronomical Society of the Pacific Conference Series*, Vol. 314, *Astronomical Data Analysis Software and Systems (ADASS) XIII*, ed. F. Ochsenbein, M. G. Allen, & D. Egret, 759
- Gehrels, N. 1986, *ApJ*, 303, 336, doi: [10.1086/164079](https://doi.org/10.1086/164079)
- Gehrels, N., Chincarini, G., Giommi, P., et al. 2004, *ApJ*, 611, 1005, doi: [10.1086/422091](https://doi.org/10.1086/422091)
- Gezari, S. 2021, *ARA&A*, 59, doi: [10.1146/annurev-astro-111720-030029](https://doi.org/10.1146/annurev-astro-111720-030029)
- Gezari, S., Cenko, S. B., & Arcavi, I. 2017, *ApJL*, 851, L47, doi: [10.3847/2041-8213/aaa0c2](https://doi.org/10.3847/2041-8213/aaa0c2)
- Gezari, S., Chornock, R., Rest, A., et al. 2012, *Nature*, 485, 217, doi: [10.1038/nature10990](https://doi.org/10.1038/nature10990)
- Gilfanov, M., Sazonov, S., Sunyaev, R., et al. 2020, *The Astronomer's Telegram*, 14246, 1
- Greiner, J., Schwarz, R., Zharikov, S., & Orio, M. 2000, *A&A*, 362, L25. <https://arxiv.org/abs/astro-ph/0009430>
- Grupe, D., Thomas, H. C., & Leighly, K. M. 1999, *A&A*, 350, L31. <https://arxiv.org/abs/astro-ph/9909101>
- Guillochon, J., Manukian, H., & Ramirez-Ruiz, E. 2014, *ApJ*, 783, 23, doi: [10.1088/0004-637X/783/1/23](https://doi.org/10.1088/0004-637X/783/1/23)
- Gültekin, K., King, A. L., Cackett, E. M., et al. 2019, *ApJ*, 871, 80, doi: [10.3847/1538-4357/aaf6b9](https://doi.org/10.3847/1538-4357/aaf6b9)
- Haardt, F., & Maraschi, L. 1991, *ApJL*, 380, L51, doi: [10.1086/186171](https://doi.org/10.1086/186171)
- Hammerstein, E., van Velzen, S., Gezari, S., et al. 2023a, *ApJ*, 942, 9, doi: [10.3847/1538-4357/aca283](https://doi.org/10.3847/1538-4357/aca283)
- Hammerstein, E., Cenko, S. B., Gezari, S., et al. 2023b, *arXiv e-prints*, arXiv:2307.15705, doi: [10.48550/arXiv.2307.15705](https://doi.org/10.48550/arXiv.2307.15705)
- Heasarc. 2014, *HEASoft: Unified Release of FTOOLS and XANADU*. <http://ascl.net/1408.004>
- HI4PI Collaboration, Ben Bekhti, N., Flöer, L., et al. 2016, *A&A*, 594, A116, doi: [10.1051/0004-6361/201629178](https://doi.org/10.1051/0004-6361/201629178)
- Hills, J. G. 1975, *Nature*, 254, 295, doi: [10.1038/254295a0](https://doi.org/10.1038/254295a0)
- Holoien, T. W. S., Prieto, J. L., Bersier, D., et al. 2014, *MNRAS*, 445, 3263, doi: [10.1093/mnras/stu1922](https://doi.org/10.1093/mnras/stu1922)
- Holoien, T. W. S., Kochanek, C. S., Prieto, J. L., et al. 2016a, *MNRAS*, 455, 2918, doi: [10.1093/mnras/stv2486](https://doi.org/10.1093/mnras/stv2486)
- . 2016b, *MNRAS*, 463, 3813, doi: [10.1093/mnras/stw2272](https://doi.org/10.1093/mnras/stw2272)
- Holoien, T. W. S., Huber, M. E., Shappee, B. J., et al. 2019, *ApJ*, 880, 120, doi: [10.3847/1538-4357/ab2ae1](https://doi.org/10.3847/1538-4357/ab2ae1)
- Hornschemeier, A., Zhang, W., STAR-X Team, & Kara, E. 2023, in *American Astronomical Society Meeting Abstracts*, Vol. 55, *American Astronomical Society Meeting Abstracts*, 120.05
- Hung, T., Gezari, S., Blagorodnova, N., et al. 2017, *ApJ*, 842, 29, doi: [10.3847/1538-4357/aa7337](https://doi.org/10.3847/1538-4357/aa7337)
- Hunter, J. D. 2007, *Computing In Science & Engineering*, 9, 90, doi: [10.1109/MCSE.2007.55](https://doi.org/10.1109/MCSE.2007.55)
- Ivezić, Ž., Kahn, S. M., Tyson, J. A., et al. 2019, *ApJ*, 873, 111, doi: [10.3847/1538-4357/ab042c](https://doi.org/10.3847/1538-4357/ab042c)
- Jiang, Y.-F., Guillochon, J., & Loeb, A. 2016, *ApJ*, 830, 125, doi: [10.3847/0004-637X/830/2/125](https://doi.org/10.3847/0004-637X/830/2/125)
- Johnson, B. D., Leja, J., Conroy, C., & Speagle, J. S. 2021, *ApJS*, 254, 22, doi: [10.3847/1538-4365/abef67](https://doi.org/10.3847/1538-4365/abef67)
- Jonker, P. G., Stone, N. C., Generozov, A., van Velzen, S., & Metzger, B. 2020, *ApJ*, 889, 166, doi: [10.3847/1538-4357/ab659c](https://doi.org/10.3847/1538-4357/ab659c)



- Kajava, J. J. E., Giustini, M., Saxton, R. D., & Miniutti, G. 2020, *A&A*, 639, A100, doi: [10.1051/0004-6361/202038165](https://doi.org/10.1051/0004-6361/202038165)
- Kara, E., Dai, L., Reynolds, C. S., & Kallman, T. 2018, *MNRAS*, 474, 3593, doi: [10.1093/mnras/stx3004](https://doi.org/10.1093/mnras/stx3004)
- Kobayashi, H., Ohsuga, K., Takahashi, H. R., et al. 2018, *PASJ*, 70, 22, doi: [10.1093/pasj/psx157](https://doi.org/10.1093/pasj/psx157)
- Komossa, S., & Greiner, J. 1999, *A&A*, 349, L45. <https://arxiv.org/abs/astro-ph/9908216>
- Kosec, P., Pasham, D., Kara, E., & Tombesi, F. 2023, *ApJ*, 954, 170, doi: [10.3847/1538-4357/aced87](https://doi.org/10.3847/1538-4357/aced87)
- Koss, M. J., Ricci, C., Trakhtenbrot, B., et al. 2022, *ApJS*, 261, 2, doi: [10.3847/1538-4365/ac6c05](https://doi.org/10.3847/1538-4365/ac6c05)
- Krolik, J., Piran, T., Svirski, G., & Cheng, R. M. 2016, *ApJ*, 827, 127, doi: [10.3847/0004-637X/827/2/127](https://doi.org/10.3847/0004-637X/827/2/127)
- Kulkarni, S. R., Harrison, F. A., Grefenstette, B. W., et al. 2021, arXiv e-prints, arXiv:2111.15608, doi: [10.48550/arXiv.2111.15608](https://doi.org/10.48550/arXiv.2111.15608)
- Lin, D., Maksym, P. W., Irwin, J. A., et al. 2015, *ApJ*, 811, 43, doi: [10.1088/0004-637X/811/1/43](https://doi.org/10.1088/0004-637X/811/1/43)
- Liu, X.-L., Dou, L.-M., Chen, J.-H., & Shen, R.-F. 2022, *ApJ*, 925, 67, doi: [10.3847/1538-4357/ac33a9](https://doi.org/10.3847/1538-4357/ac33a9)
- Lodato, G., & Rossi, E. M. 2011, *MNRAS*, 410, 359, doi: [10.1111/j.1365-2966.2010.17448.x](https://doi.org/10.1111/j.1365-2966.2010.17448.x)
- Loeb, A., & Ulmer, A. 1997, *ApJ*, 489, 573, doi: [10.1086/304814](https://doi.org/10.1086/304814)
- Lu, W., & Kumar, P. 2018, *ApJ*, 865, 128, doi: [10.3847/1538-4357/aad54a](https://doi.org/10.3847/1538-4357/aad54a)
- Madsen, K., Hickox, R., Bachetti, M., et al. 2019, in *Bulletin of the American Astronomical Society*, Vol. 51, 166
- Mainzer, A., Bauer, J., Cutri, R. M., et al. 2014, *ApJ*, 792, 30, doi: [10.1088/0004-637X/792/1/30](https://doi.org/10.1088/0004-637X/792/1/30)
- Makishima, K., Maejima, Y., Mitsuda, K., et al. 1986, *ApJ*, 308, 635, doi: [10.1086/164534](https://doi.org/10.1086/164534)
- Malyali, A., Liu, Z., Merloni, A., et al. 2023, *MNRAS*, 520, 4209, doi: [10.1093/mnras/stad046](https://doi.org/10.1093/mnras/stad046)
- Masci, F. J., Laher, R. R., Rusholme, B., et al. 2019, *PASP*, 131, 018003, doi: [10.1088/1538-3873/aae8ac](https://doi.org/10.1088/1538-3873/aae8ac)
- . 2023, arXiv e-prints, arXiv:2305.16279, doi: [10.48550/arXiv.2305.16279](https://doi.org/10.48550/arXiv.2305.16279)
- Masterson, M., De, K., Panagiotou, C., et al. 2024, arXiv e-prints, arXiv:2401.01403, doi: [10.48550/arXiv.2401.01403](https://doi.org/10.48550/arXiv.2401.01403)
- Metzger, B. D. 2022, *ApJL*, 937, L12, doi: [10.3847/2041-8213/ac90ba](https://doi.org/10.3847/2041-8213/ac90ba)
- Metzger, B. D., & Stone, N. C. 2016, *MNRAS*, 461, 948, doi: [10.1093/mnras/stw1394](https://doi.org/10.1093/mnras/stw1394)
- Miller, J. M., Kaastra, J. S., Miller, M. C., et al. 2015, *Nature*, 526, 542, doi: [10.1038/nature15708](https://doi.org/10.1038/nature15708)
- Miller, K. A., & Stone, J. M. 2000, *ApJ*, 534, 398, doi: [10.1086/308736](https://doi.org/10.1086/308736)
- Mitsuda, K., Inoue, H., Koyama, K., et al. 1984, *PASJ*, 36, 741
- Mummery, A. 2021, *MNRAS*, 507, L24, doi: [10.1093/mnrasl/slab088](https://doi.org/10.1093/mnrasl/slab088)
- Mummery, A., & Balbus, S. 2022, *MNRAS*, 517, 3423, doi: [10.1093/mnras/stac2844](https://doi.org/10.1093/mnras/stac2844)
- Mummery, A., & Balbus, S. A. 2020, *MNRAS*, 492, 5655, doi: [10.1093/mnras/staa192](https://doi.org/10.1093/mnras/staa192)
- . 2021, *MNRAS*, 505, 1629, doi: [10.1093/mnras/stab1141](https://doi.org/10.1093/mnras/stab1141)
- Mummery, A., Wevers, T., Saxton, R., & Pasham, D. 2023, *MNRAS*, 519, 5828, doi: [10.1093/mnras/stac3798](https://doi.org/10.1093/mnras/stac3798)
- Nicholl, M., Wevers, T., Oates, S. R., et al. 2020, *MNRAS*, 499, 482, doi: [10.1093/mnras/staa2824](https://doi.org/10.1093/mnras/staa2824)
- Panagiotou, C., De, K., Masterson, M., et al. 2023, *ApJL*, 948, L5, doi: [10.3847/2041-8213/acc02f](https://doi.org/10.3847/2041-8213/acc02f)
- Parkinson, E. J., Knigge, C., Matthews, J. H., et al. 2022, *MNRAS*, 510, 5426, doi: [10.1093/mnras/stac027](https://doi.org/10.1093/mnras/stac027)
- Pasham, D. R., Cenko, S. B., Levan, A. J., et al. 2015, *ApJ*, 805, 68, doi: [10.1088/0004-637X/805/1/68](https://doi.org/10.1088/0004-637X/805/1/68)
- Pasham, D. R., Lucchini, M., Laskar, T., et al. 2023, *Nature Astronomy*, 7, 88, doi: [10.1038/s41550-022-01820-x](https://doi.org/10.1038/s41550-022-01820-x)
- Pasham, D. R., Zajacek, M., Nixon, C. J., et al. 2024, arXiv e-prints, arXiv:2402.09689, doi: [10.48550/arXiv.2402.09689](https://doi.org/10.48550/arXiv.2402.09689)
- Piran, T., Svirski, G., Krolik, J., Cheng, R. M., & Shiokawa, H. 2015, *ApJ*, 806, 164, doi: [10.1088/0004-637X/806/2/164](https://doi.org/10.1088/0004-637X/806/2/164)
- Predehl, P., Andritschke, R., Arefiev, V., et al. 2021, *A&A*, 647, A1, doi: [10.1051/0004-6361/202039313](https://doi.org/10.1051/0004-6361/202039313)
- Quintin, E., Webb, N. A., Guillot, S., et al. 2023, *A&A*, 675, A152, doi: [10.1051/0004-6361/202346440](https://doi.org/10.1051/0004-6361/202346440)
- Rees, M. J. 1988, *Nature*, 333, 523, doi: [10.1038/333523a0](https://doi.org/10.1038/333523a0)
- Remillard, R. A., & McClintock, J. E. 2006, *ARA&A*, 44, 49, doi: [10.1146/annurev.astro.44.051905.092532](https://doi.org/10.1146/annurev.astro.44.051905.092532)
- Ricci, C., Trakhtenbrot, B., Koss, M. J., et al. 2017, *ApJS*, 233, 17, doi: [10.3847/1538-4365/aa96ad](https://doi.org/10.3847/1538-4365/aa96ad)
- Ricci, C., Kara, E., Loewenstein, M., et al. 2020, *ApJL*, 898, L1, doi: [10.3847/2041-8213/ab91a1](https://doi.org/10.3847/2041-8213/ab91a1)
- Roming, P. W. A., Kennedy, T. E., Mason, K. O., et al. 2005, *SSRv*, 120, 95, doi: [10.1007/s11214-005-5095-4](https://doi.org/10.1007/s11214-005-5095-4)
- Roth, N., Kasen, D., Guillochon, J., & Ramirez-Ruiz, E. 2016, *ApJ*, 827, 3, doi: [10.3847/0004-637X/827/1/3](https://doi.org/10.3847/0004-637X/827/1/3)
- Sagiv, I., Gal-Yam, A., Ofek, E. O., et al. 2014, *AJ*, 147, 79, doi: [10.1088/0004-6256/147/4/79](https://doi.org/10.1088/0004-6256/147/4/79)
- Saxton, R., Komossa, S., Auchtell, K., & Jonker, P. G. 2020, *SSRv*, 216, 85, doi: [10.1007/s11214-020-00708-4](https://doi.org/10.1007/s11214-020-00708-4)
- Saxton, R. D., Read, A. M., Komossa, S., et al. 2017, *A&A*, 598, A29, doi: [10.1051/0004-6361/201629015](https://doi.org/10.1051/0004-6361/201629015)

- Sazonov, S., Gilfanov, M., Medvedev, P., et al. 2021, *MNRAS*, 508, 3820, doi: [10.1093/mnras/stab2843](https://doi.org/10.1093/mnras/stab2843)
- Schlafly, E. F., & Finkbeiner, D. P. 2011, *ApJ*, 737, 103, doi: [10.1088/0004-637X/737/2/103](https://doi.org/10.1088/0004-637X/737/2/103)
- Schmidt, M. 1968, *ApJ*, 151, 393, doi: [10.1086/149446](https://doi.org/10.1086/149446)
- Schnittman, J. D., Krolik, J. H., & Noble, S. C. 2016, *ApJ*, 819, 48, doi: [10.3847/0004-637X/819/1/48](https://doi.org/10.3847/0004-637X/819/1/48)
- Shakura, N. I., & Sunyaev, R. A. 1973, *A&A*, 24, 337
- Shiokawa, H., Krolik, J. H., Cheng, R. M., Piran, T., & Noble, S. C. 2015, *ApJ*, 804, 85, doi: [10.1088/0004-637X/804/2/85](https://doi.org/10.1088/0004-637X/804/2/85)
- Short, P., Nicholl, M., Lawrence, A., et al. 2020, *MNRAS*, 498, 4119, doi: [10.1093/mnras/staa2065](https://doi.org/10.1093/mnras/staa2065)
- Stein, R., Velzen, S. v., Kowalski, M., et al. 2021, *Nature Astronomy*, 5, 510, doi: [10.1038/s41550-020-01295-8](https://doi.org/10.1038/s41550-020-01295-8)
- Steiner, J. F., Narayan, R., McClintock, J. E., & Ebisawa, K. 2009, *PASP*, 121, 1279, doi: [10.1086/648535](https://doi.org/10.1086/648535)
- Stern, D., Assef, R. J., Benford, D. J., et al. 2012, Mid-infrared Selection of Active Galactic Nuclei with the Wide-Field Infrared Survey Explorer. I. Characterizing WISE-selected Active Galactic Nuclei in COSMOS, doi: [10.1088/0004-637X/753/1/30](https://doi.org/10.1088/0004-637X/753/1/30)
- Stone, N., & Loeb, A. 2012, *PhRvL*, 108, 061302, doi: [10.1103/PhysRevLett.108.061302](https://doi.org/10.1103/PhysRevLett.108.061302)
- Strüder, L., Briel, U., Dennerl, K., et al. 2001, *A&A*, 365, L18, doi: [10.1051/0004-6361:20000066](https://doi.org/10.1051/0004-6361:20000066)
- Sunyaev, R., Arefiev, V., Babushkin, V., et al. 2021, *A&A*, 656, A132, doi: [10.1051/0004-6361/202141179](https://doi.org/10.1051/0004-6361/202141179)
- Takeuchi, S., Ohsuga, K., & Mineshige, S. 2013, *PASJ*, 65, 88, doi: [10.1093/pasj/65.4.88](https://doi.org/10.1093/pasj/65.4.88)
- Thomsen, L. L., Kwan, T. M., Dai, L., et al. 2022, *The Astrophysical Journal Letters*, 937, L28, doi: [10.3847/2041-8213/ac911f](https://doi.org/10.3847/2041-8213/ac911f)
- Titarchuk, L., & Lyubarskij, Y. 1995, *ApJ*, 450, 876, doi: [10.1086/176191](https://doi.org/10.1086/176191)
- Tonry, J. L., Denneau, L., Heinze, A. N., et al. 2018, *PASP*, 130, 064505, doi: [10.1088/1538-3873/aabadf](https://doi.org/10.1088/1538-3873/aabadf)
- Trakhtenbrot, B., Arcavi, I., MacLeod, C. L., et al. 2019, *ApJ*, 883, 94, doi: [10.3847/1538-4357/ab39e4](https://doi.org/10.3847/1538-4357/ab39e4)
- Udalski, A., Szymański, M. K., & Szymański, G. 2015, *AcA*, 65, 1. <https://arxiv.org/abs/1504.05966>
- Ulmer, A. 1999, *ApJ*, 514, 180, doi: [10.1086/306909](https://doi.org/10.1086/306909)
- van Velzen, S. 2018, *ApJ*, 852, 72, doi: [10.3847/1538-4357/aa998e](https://doi.org/10.3847/1538-4357/aa998e)
- van Velzen, S., Gezari, S., Cenko, S. B., et al. 2019, *ApJ*, 872, 198, doi: [10.3847/1538-4357/aafe0c](https://doi.org/10.3847/1538-4357/aafe0c)
- van Velzen, S., Gezari, S., Hammerstein, E., et al. 2021, *ApJ*, 908, 4, doi: [10.3847/1538-4357/abc258](https://doi.org/10.3847/1538-4357/abc258)
- Virtanen, P., Gommers, R., Oliphant, T. E., et al. 2020, *Nature Methods*, 17, 261, doi: [10.1038/s41592-019-0686-2](https://doi.org/10.1038/s41592-019-0686-2)
- Wang, J., Kara, E., Lucchini, M., et al. 2022, *ApJ*, 930, 18, doi: [10.3847/1538-4357/ac6262](https://doi.org/10.3847/1538-4357/ac6262)
- Wen, S., Jonker, P. G., Stone, N. C., Zabludoff, A. I., & Psaltis, D. 2020, *ApJ*, 897, 80, doi: [10.3847/1538-4357/ab9817](https://doi.org/10.3847/1538-4357/ab9817)
- Wevers, T. 2020, *MNRAS*, 497, L1, doi: [10.1093/mnras/slaa097](https://doi.org/10.1093/mnras/slaa097)
- Wevers, T., Pasham, D. R., van Velzen, S., et al. 2019a, *MNRAS*, 488, 4816, doi: [10.1093/mnras/stz1976](https://doi.org/10.1093/mnras/stz1976)
- Wevers, T., Stone, N. C., van Velzen, S., et al. 2019b, *MNRAS*, 487, 4136, doi: [10.1093/mnras/stz1602](https://doi.org/10.1093/mnras/stz1602)
- Wevers, T., Pasham, D. R., van Velzen, S., et al. 2021, *ApJ*, 912, 151, doi: [10.3847/1538-4357/abf5e2](https://doi.org/10.3847/1538-4357/abf5e2)
- Wevers, T., Nicholl, M., Guolo, M., et al. 2022, *A&A*, 666, A6, doi: [10.1051/0004-6361/202142616](https://doi.org/10.1051/0004-6361/202142616)
- Wilms, J., Allen, A., & McCray, R. 2000, *ApJ*, 542, 914, doi: [10.1086/317016](https://doi.org/10.1086/317016)
- Wyrzykowski, L., Zieliński, M., Kostrzewa-Rutkowska, Z., et al. 2017, *MNRAS*, 465, L114, doi: [10.1093/mnras/slw213](https://doi.org/10.1093/mnras/slw213)
- Yao, Y., & Gezari, S. 2022, *The Astronomer's Telegram*, 15751, 1
- Yao, Y., Lu, W., Harrison, F., et al. 2023a, arXiv e-prints, arXiv:2308.09834, doi: [10.48550/arXiv.2308.09834](https://doi.org/10.48550/arXiv.2308.09834)
- Yao, Y., Wang, Q. D., & Nan Zhang, S. 2005, *MNRAS*, 362, 229, doi: [10.1111/j.1365-2966.2005.09294.x](https://doi.org/10.1111/j.1365-2966.2005.09294.x)
- Yao, Y., Lu, W., Guolo, M., et al. 2022, *The Astrophysical Journal*, 937, 8, doi: [10.3847/1538-4357/ac898a](https://doi.org/10.3847/1538-4357/ac898a)
- Yao, Y., Ravi, V., Gezari, S., et al. 2023b, *ApJL*, 955, L6, doi: [10.3847/2041-8213/acf216](https://doi.org/10.3847/2041-8213/acf216)
- Yuan, W., Zhang, C., Chen, Y., & Ling, Z. 2022, in *Handbook of X-ray and Gamma-ray Astrophysics*, 86, doi: [10.1007/978-981-16-4544-0\\_151-1](https://doi.org/10.1007/978-981-16-4544-0_151-1)
- Zauderer, B. A., Berger, E., Soderberg, A. M., et al. 2011, *Nature*, 476, 425, doi: [10.1038/nature10366](https://doi.org/10.1038/nature10366)

## APPENDIX

A. MODELING OF CORONA EMISSION IN TDES WITH `simPL`

In the study of active galactic nuclei (AGN), the corona is the primary X-ray emitter, while the cold accretion disks mainly emit in the UV bands. AGN X-ray spectra are often described using the `powerlaw` model, despite some attempts to develop more comprehensive models like `Optxagnf` (Done et al. 2012), these face challenges due to numerous parameters and degeneracies. Therefore, the `powerlaw` model remains prevalent in AGN X-ray literature.

In X-ray binaries (XRBs), the accretion disks are hotter and emit mainly in the X-ray bands. In the soft state of XRBs, the accretion disk dominates the X-ray emission, but as they transition to the hard state, an emergent corona with a power-law spectrum becomes dominant. The `powerlaw` model is widely used in XRB modeling but suffers from the drawback of rising infinitely at low energies, which is inconsistent with Comptonization.

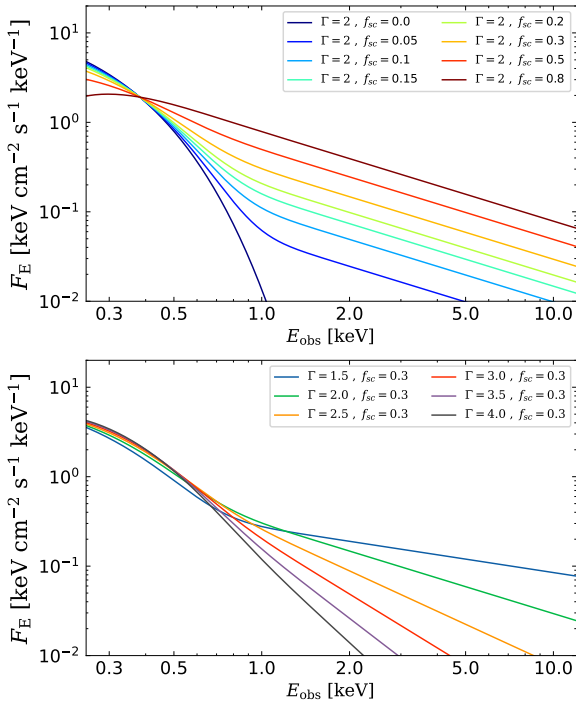


**Figure 21.** Simulation of `SimPL` model spectra. Upper panel: Fixed power law index ( $\Gamma_{sc}$ ) varying fraction of up-scattered photons ( $f_{sc}$ ). Bottom panel: Fixed  $f_{sc}$  varying  $\Gamma_{sc}$ .

To overcome the limitation of the `powerlaw` model in accurately describing Comptonization, Steiner et al.

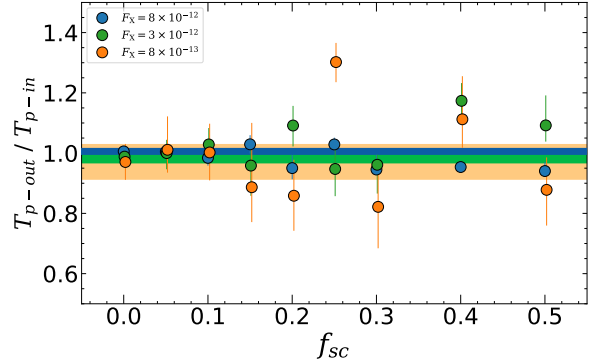


**Figure 22.** Simulation on the measurement of the underlying disk properties in the presence of a corona comptonization. The y-axis show the ratio between the input and output  $T_p$  as a function of the corona strength ( $f_{sc}$ ). The color show distinct fluxes of the mock spectra, and the shaded regions the uncertainty in the  $f_{sc} = 0$  spectra, i.e. the uncertainty from the instrumental S/N.

(2009) introduced `simPL`, a flexible convolution model for fitting X-ray spectra of XRBs. `simPL` captures Comptonization effects using any seed photon spectrum and shares parameters such as the photon index ( $\Gamma$ ) with the `powerlaw` model. However, it employs the scattered fraction ( $f_{sc}$ ) as the normalization factor instead of photon flux, simplifying the model by omitting specific details of the Comptonizing medium while maintaining a physically consistent approach. Unlike the `powerlaw` model, `simPL` directly links the power-law component to the input photon energy distribution, resulting in a power-law tail at higher energies without extending indefinitely to lower energies. This behavior aligns with Compton-scattering expectations and is commonly observed in physical Comptonization models. Notably, in the soft X-ray bands, `simPL` exhibits a natural cutoff consistent with Comptonization, whereas the `powerlaw` model continues to rise without limit (Yao et al. 2005).

Similarly to XRBs, TDEs also have a portion of their continuum disk emission in the X-rays. Therefore, a similar approach can be applied to model the X-ray spectra of TDEs. Figure 21 demonstrates the effects of using `simPL` through a series of simulations where a thermal model with  $T_p \approx 70$  eV and  $R_p \approx 10^{12}$  cm is convoluted with `simPL` using different values of  $f_{sc}$  (top panel) and  $\Gamma$  (bottom panel). With  $f_{sc} = 0$ , there is no corona emission, the resulting model corresponds to the input disk spectrum. As  $f_{sc}$  increases from 0.05, the spectrum remains dominated by the disk, but with a faint hard excess. Between  $0.5 \leq f_{sc} \leq 0.20$ , the source enters an

intermediate state, where the thermal and non-thermal spectra have similar fluxes. When  $f_{sc} \approx 0.3$ , the total spectrum becomes almost indistinguishable from a pure power-law, and the spectrum remains consistent with a power law for higher values.

An important question to our X-ray spectral analyses (3 and 4.2) is up to what corona strength (as probed by  $f_{sc}$ ) the underlying thermal continuum can be recovered from the fitting. To answer this question we simulate mock X-ray spectra using the `fakeit` command in `xspec` for a stacked 30 ks observation with *Swift*/XRT, assuming `simPL $\otimes$ tdediscspec`, a random  $T_p$  in the range of observed in our sample, for three fluxes ( $F_X = 8 \times 10^{-12}, 3 \times 10^{-12}, 8 \times 10^{-13} \text{ erg cm}^{-2} \text{ s}^{-1}$ ) levels, and varying  $f_{sc}$  between 0.0 (no corona) and 0.5. We then fit the mock spectra with the same model in order to measure the best-fit  $T_p$ , and compare with the input value. Fig. 22 summarized our findings. The underlying (input) temperature can be recovered (within the error-bar) considering the uncertainties related with the S/N of the instrument (shaded regions) up to  $f_{sc} \approx 0.2$ , at higher values the underlying information on the temperature of the disk is lost by the emergency of the corona in the higher energies of the disk spectrum, and can not be uniquely recovered.

### B. SIMULATION OF EXPECTED $L_{BB}/L_X$ FOR STANDARD DISK

An important observational probe of TDE emission is the ratio  $L_{BB}/L_X$  between the UV/optical luminosity (as fitted by a blackbody) and the 0.3-10 keV X-ray luminosity. Although additional emission processes should be involved, the formation of accretion disk is a natural prediction of a tidal disruption event. In this section, we aim to probe the range of  $L_{BB}/L_X$  that can be produce by an *bare/unreprocessed* accretion disk, given the range of inner peak temperatures ( $T_p$ ) we observe from the X-ray fitting. To obtain that we simulate accretion disk with varying  $T_p$  between  $5.5 \leq \log T_p \leq 6.1$  Kelvin, we test two distinct disk solutions for the the temperature profile of the disk: the standard vanishing ISCO stress solution (Shakura & Sunyaev 1973; Makishima et al. 1986),  $T(R) \propto R^{-3/4}$ , and the finite ISCO stress (Agol & Krolik 2000),  $T(R) \propto R^{-7/8}$ . We also explore distinct disk outer radius, from  $R_{out}/R_p \in (5, 50)$ . We pass the synthetic SED into the sensibility curve of the six UVOT and two ZTF filters, and fitted the resulting broad-band UV/optical with a blackbody to obtain  $L_{BB}$ , the same way it was done in the observed data (see Fig. 3 for illustration). The ratio  $L_{BB}/L_X$  as a function of  $T_p$  for the two distinct disk solution is shown in Fig. 23. For the entire range  $L_{BB}/L_X$  is between  $5 \times 10^{-2}$  and a

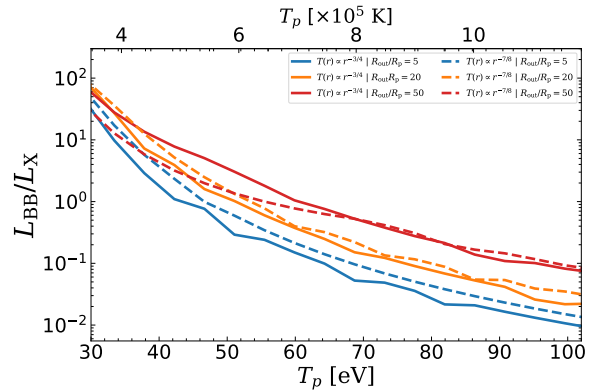


**Figure 23.** Simulation of expected UV/optical to X-ray luminosity ratio ( $L_{BB}/L_X$ ) for standard disk. The y-axis show the expected  $L_{BB}/L_X$  from a *bare/unreprocessed* accretion disk with two distinct temperature profiles (solid and dashed lines), as a function of the peak temperature of the disk ( $T_p$ ).

maximum of  $\sim 70$ . At late times, most our sample shows disk cooling, and all TDE have  $\log T_p \leq 5.8$ , this limits  $L_{BB}/L_X$  to values  $> 0.3$ , but rarely higher than 10, which is in agreement with our findings in Fig. 14.

### C. THE BASS AGN SAMPLE

The *Swift*/BAT 70-month AGN catalog consists of 858 nearby ( $z \lesssim 0.3$  for unbeamed) AGN (Koss et al. 2022), and using soft X-ray observations by XMM-Newton, *Swift*, ASCA, Chandra, and Suzaku, their broadband X-ray spectra were characterized and presented by Ricci et al. (2017). Some of the properties they constrain are the intrinsic X-ray luminosity (in the 2–10, 20–50, and 14–150 keV bands), the line-of-sight column density of obscuring material ( $N_H$ ), the slope of the X-ray power-law continuum, and the temperature of the thermal plasma for obscured sources. The many phenomenological models used are broadly classified into four groups: unobscured (352), obscured (386), blazars (97), and other non-AGN models (2). The remaining details of the X-ray modeling of the BASS sample can be found in Ricci et al. (2017).

From among these sources, we selected those that were either obscured or unobscured (which excludes beamed and non-AGN sources), and that had spectroscopic redshift measurements from optical counterparts. This resulted in 617 sources. To calculate the HR, the X-ray spectra were simulated from the models using `XSPEC`, and the count rate was recorded for the soft (0.3–2.0 keV) and hard (2.0–10.0 keV) bands. Spectra were measured with a long response time (1 Ms) to minimize the effects of statistical noise on the HR. This was done twice: with the response files for *Swift*/XRT photon counting grade 0-12 and XMM-Newton Epic PN. We also measured the 0.3-10.0 keV intrinsic luminosities by

setting all  $N_{\text{H}}$  parameters of all model components to zero (or, in certain cases, the minimum nonzero value allowed by the model) and using the `calcLumin` command.

#### D. SUPPLEMENTARY DATA

**Table 5.** ZTF control sample, described in §4.5.

Source	$z$	$L_X \geq 10^{42} \text{ erg s}^{-1}$	$\log(M_{\text{BH}}/M_{\odot})^{\text{a}}$
AT2018zr	0.075	False	$5.83 \pm 0.51$
AT2018bsi	0.051	False	$7.46 \pm 0.47$
AT2018hco	0.088	False	$6.44 \pm 0.48$
AT2018iih	0.212	False	$7.93 \pm 0.48$
AT2018hyz	0.046	False	$6.12 \pm 0.46$
AT2018lna	0.091	False	$5.21 \pm 0.54$
AT2019azh	0.022	True	$6.68 \pm 0.46$
AT2019dsg	0.051	True	$7.04 \pm 0.45$
AT2019ehz	0.074	True	$5.75 \pm 0.59$
AT2019mha	0.148	False	$6.41 \pm 0.49$
AT2019meg	0.152	False	$5.81 \pm 0.52$
AT2019qiz	0.015	False	$6.49 \pm 0.49$
AT2019teq	0.087	True	$6.32 \pm 0.49$
AT2020pj	0.068	False	$6.43 \pm 0.49$
AT2019vcb	0.088	True	$5.59 \pm 0.52$
AT2020ddv	0.160	True	$6.09 \pm 0.55$
AT2020ksf	0.092	True	$5.92 \pm 0.48$
AT2020ocn	0.070	True	$6.77 \pm 0.49$
AT2020mot	0.070	False	$7.04 \pm 0.47$
AT2020wey	0.027	False	$5.38 \pm 0.51$
AT2020zso	0.057	False	$6.12 \pm 0.48$
AT2020vwl	0.033	False	$5.80 \pm 0.48$
AT2021ehb	0.018	True	$7.04 \pm 0.46$
AT2021nwa	0.047	False	$7.21 \pm 0.46$
AT2020ksf	0.092	True	$5.92 \pm 0.48$
AT2021yzv	0.286	True	$7.45 \pm 0.47$

NOTE—<sup>a</sup>) Black hole masses. When a  $\sigma_*$  measurement is available it is estimated using the Gültekin et al. (2019)  $\sigma_*-M_{\text{BH}}$  relation, when  $\sigma_*$  is not available, this is estimated from the  $M_*-M_{\text{BH}}$  relation presented in Yao et al. 2023b.

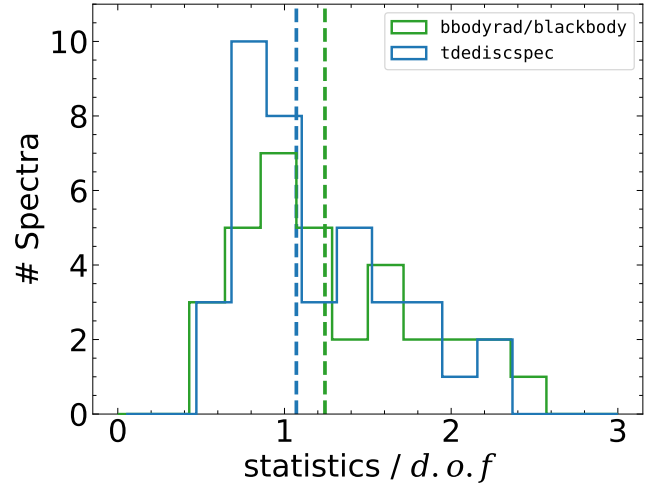


**Figure 24.** Distribution of ratio of the statistics ( $\chi^2$  for *XMM-Newton* and ‘c-statistics’ (Cash 1979) for *Swift/XRT*) over degrees of freedom (*d.o.f*) for spectra with negligible ‘hard excess’ (i.e.  $f_{sc} \sim 0.0$ ) for `tddiscspec` and `blackbody`, `xspec` models. Dashed line show the median values for the models.



**Table 6.** Luminosity function data

Source	z	'peak' $L_X$ ( $\text{erg s}^{-1}$ )	Survey
AT2018zr	0.071	$5.55 \times 10^{41}$	ZTF
AT2018hyz	0.045	$7.51 \times 10^{41}$	ZTF/ASASSN
AT2019azh	0.022	$1.65 \times 10^{43}$	ZTF/ASASSN
AT2019dsg	0.051	$3.90 \times 10^{43}$	ZTF
AT2019ehz	0.074	$6.35 \times 10^{43}$	ZTF
AT2019qiz	0.015	$8.06 \times 10^{40}$	ZTF/ASASSN
AT2019teq	0.087	$4.06 \times 10^{43}$	ZTF
AT2019vcb	0.088	$1.66 \times 10^{43}$	ZTF
AT2020ddv	0.160	$3.45 \times 10^{43}$	ZTF
AT2020ksf	0.092	$1.07 \times 10^{44}$	ZTF/eROSITA
AT2020ocn	0.070	$1.04 \times 10^{44}$	ZTF
AT2021ehb	0.018	$1.78 \times 10^{44}$	ZTF
ASASSN-14li	0.020	$9.77 \times 10^{43}$	ASASSN
ASASSN-15oi	0.048	$4.93 \times 10^{42}$	ASASSN
AT2018fyk	0.059	$1.76 \times 10^{44}$	ASASSN
OGLE16aaa	0.165	$4.92 \times 10^{43}$	OGLE
AT2021yzv	0.288	$3.83 \times 10^{42}$	ZTF
J135514.8+311605	0.199	$5.80 \times 10^{43}$	eROSITA
J013204.6+122236	0.123	$4.20 \times 10^{43}$	eROSITA
J153503.4+455056	0.231	$8.80 \times 10^{43}$	eROSITA
J163831.7+534020	0.581	$2.50 \times 10^{44}$	eROSITA
J163030.2+470125	0.294	$2.00 \times 10^{44}$	eROSITA
J021939.9+361819	0.387	$2.50 \times 10^{44}$	eROSITA
J161001.2+330121	0.131	$1.20 \times 10^{43}$	eROSITA
J171423.6+085236	0.036	$5.30 \times 10^{42}$	eROSITA
J071310.6+725627	0.104	$1.10 \times 10^{44}$	eROSITA
J095928.6+643023	0.045	$8.90 \times 10^{44}$	eROSITA
J091747.6+524821	0.187	$4.80 \times 10^{44}$	eROSITA
J133053.3+734824	0.150	$3.40 \times 10^{43}$	eROSITA
J144738.4+671821	0.125	$2.70 \times 10^{43}$	eROSITA
NGC5905	0.011	$7.00 \times 10^{42}$	ROSAT
RXJ1624+7554	0.064	$2.00 \times 10^{44}$	ROSAT
RBS 1032	0.026	$1.00 \times 10^{43}$	ROSAT
RXJ1420+5334	0.147	$2.50 \times 10^{44}$	ROSAT
RXJ 1242-1119	0.050	$4.00 \times 10^{44}$	ROSAT
TDXF1347-3254	0.037	$7.00 \times 10^{42}$	ROSAT
NGC 3599	0.003	$1.20 \times 10^{41}$	XMMLS
SDSS J1323+48	0.087	$4.40 \times 10^{43}$	XMMLS
SDSS J0939+37	0.184	$2.60 \times 10^{44}$	XMMLS
2MASX J0203-07	0.062	$2.80 \times 10^{43}$	XMMLS
2MASX J02491-04	0.019	$2.10 \times 10^{42}$	XMMLS
SDSS J1201+30	0.146	$3.00 \times 10^{44}$	XMMLS
2MASX 0740-85	0.017	$2.00 \times 10^{43}$	XMMLS
XMMSL2 J1446+68	0.029	$6.00 \times 10^{42}$	XMMLS
XMMSL1 J1404	0.043	$3.00 \times 10^{43}$	XMMLS

Table 7. Best-fit parameters for final X-ray models: `tdediscspec` or `simPL`⊗`tdediscspec`.

Source	MJD	Instrument	$T_p$ [K]	$R_p$ [cm]	$f_{sc}$	$\Gamma_{sc}$	statistics <sup>a</sup> /d.o.f
AT2018zr	58220	<i>XMM-Newton</i>	$1.1^{+0.1}_{-0.1} \times 10^6$	$2.5^{+1.1}_{-0.7} \times 10^{10}$	...	...	6.3/8
	58241	<i>XMM-Newton</i>	$1.0^{+0.2}_{-0.1} \times 10^6$	$2.0^{+1.0}_{-0.6} \times 10^{10}$	...	...	6.0/6
	58569	<i>XMM-Newton</i>	$5.2^{+0.6}_{-0.4} \times 10^5$	$2.0^{+1.0}_{-0.6} \times 10^{11}$	...	...	11.3/7
AT2018shyz	58463 <sup>+30</sup> <sub>-28</sub>	<i>Swift/XRT</i>	$1.2^{+0.3}_{-0.2} \times 10^6$	$1.1^{+0.9}_{-0.5} \times 10^{10}$	...	...	13.0/22
AT2019azh	58579	<i>XMM-Newton</i>	$5.7^{+1.4}_{-0.7} \times 10^5$	$8.9^{+4.2}_{-1.9} \times 10^{10}$	$0.03^{+0.06}_{-0.02}$	$2.2^{+1.2}_{-0.7}$	10.3/16
	58760	<i>XMM-Newton</i>	$4.1^{+0.1}_{-0.3} \times 10^5$	$2.4^{+0.3}_{-0.3} \times 10^{12}$	$0.01^{+0.02}_{-0.01}$	$1.3^{+2.3}_{-1.3}$	30.2/18
	58788	<i>XMM-Newton</i>	$3.5^{+0.1}_{-0.1} \times 10^5$	$4.0^{+0.2}_{-0.1} \times 10^{12}$	$0.01^{+0.01}_{-0.01}$	$4.3^{+0.5}_{-0.2}$	34.4/21
	58971	<i>XMM-Newton</i>	$2.8^{+0.1}_{-0.1} \times 10^5$	$6.2^{+6.0}_{-6.0} \times 10^{12}$	...	...	16.1/7
AT2019dsg	58625 <sup>+4</sup> <sub>-5</sub>	<i>Swift/XRT</i>	$6.7^{+1.4}_{-1.0} \times 10^5$	$2.3^{+3.7}_{-1.3} \times 10^{12}$	...	...	26.0/41
	58633	<i>XMM-Newton</i>	$5.7^{+0.1}_{-0.6} \times 10^5$	$2.6^{+0.2}_{-0.9} \times 10^{12}$	...	...	33.3/22
	58641 <sup>+7</sup> <sub>-7</sub>	<i>Swift/XRT</i>	$5.1^{+0.9}_{-0.7} \times 10^5$	$2.8^{+5.1}_{-1.5} \times 10^{12}$	...	...	36.4/34
AT2019ehz	58628 <sup>+1</sup> <sub>-1</sub>	<i>Swift/XRT</i>	$1.1^{+0.1}_{-0.1} \times 10^6$	$2.5^{+0.4}_{-0.3} \times 10^{11}$	...	...	84.8/78
	58633	<i>XMM-Newton</i>	$8.2^{+0.6}_{-0.5} \times 10^5$	$8.3^{+1.9}_{-1.4} \times 10^{10}$	...	...	6.5/9
	58682 <sup>+2</sup> <sub>-2</sub>	<i>Swift/XRT</i>	$1.1^{+0.1}_{-0.1} \times 10^6$	$1.9^{+0.4}_{-0.3} \times 10^{11}$	...	...	52.4/58
AT2019teq	58841	<i>XMM-Newton</i>	$1.9^{+0.1}_{-0.1} \times 10^6$	$2.5^{+0.6}_{-0.1} \times 10^{10}$	...	...	34.2/41
	58915	<i>XMM-Newton</i>	...	...	...	...	82.5/48
AT2019vcb	58991	<i>XMM-Newton</i>	$5.4^{+0.4}_{-0.3} \times 10^5$	$3.9^{+2.4}_{-1.2} \times 10^{11}$	...	...	25.1/18
	59764	<i>XMM-Newton</i>	$4.0^{+1.0}_{-0.5} \times 10^5$	$2.9^{+9.5}_{-0.5} \times 10^{11}$	...	...	9.1/8
AT2020ddv	58967	<i>XMM-Newton</i>	$7.0^{+0.2}_{-0.1} \times 10^5$	$8.4^{+0.7}_{-0.5} \times 10^{11}$	...	...	29.8/16
AT2020ksf	59185 <sup>+5</sup> <sub>-3</sub>	<i>Swift/XRT</i>	$8.0^{+0.4}_{-0.4} \times 10^5$	$7.0^{+1.2}_{-0.9} \times 10^{11}$	...	...	48.9/57
	59202 <sup>+3</sup> <sub>-3</sub>	<i>Swift/XRT</i>	$6.5^{+0.5}_{-0.4} \times 10^5$	$1.1^{+0.3}_{-0.2} \times 10^{12}$	...	...	38.8/35
	59311 <sup>+3</sup> <sub>-3</sub>	<i>Swift/XRT</i>	$6.8^{+0.5}_{-0.4} \times 10^5$	$1.0^{+0.3}_{-0.2} \times 10^{12}$	...	...	39.6/42
	59725	<i>XMM-Newton</i>	$4.3^{+0.2}_{-0.1} \times 10^5$	$2.1^{+0.3}_{-0.1} \times 10^{12}$	...	...	21.4/13
AT2020ocn	59041 <sup>+1</sup> <sub>-1</sub>	<i>Swift/XRT</i>	$8.0^{+0.7}_{-0.6} \times 10^5$	$4.5^{+1.4}_{-1.0} \times 10^{11}$	...	...	29.7/42
	59048	<i>XMM-Newton</i>	$4.9^{+0.1}_{-0.4} \times 10^5$	$2.3^{+0.1}_{-0.4} \times 10^{12}$	...	...	35.2/15
	59051 <sup>+2</sup> <sub>-3</sub>	<i>Swift/XRT</i>	$5.4^{+0.4}_{-0.4} \times 10^5$	$8.2^{+2.8}_{-1.9} \times 10^{11}$	...	...	27.8/34
	59067 <sup>+4</sup> <sub>-6</sub>	<i>Swift/XRT</i>	$9.1^{+0.5}_{-0.4} \times 10^5$	$3.2^{+0.5}_{-0.4} \times 10^{11}$	...	...	62.0/59
	59094 <sup>+12</sup> <sub>-9</sub>	<i>Swift/XRT</i>	$8.9^{+0.2}_{-0.2} \times 10^5$	$3.8^{+0.3}_{-0.3} \times 10^{11}$	...	...	89.4/84
	59131 <sup>+18</sup> <sub>-18</sub>	<i>Swift/XRT</i>	$5.1^{+0.3}_{-0.3} \times 10^5$	$1.1^{+0.2}_{-0.2} \times 10^{12}$	...	...	30.7/36
	59189 <sup>+18</sup> <sub>-18</sub>	<i>Swift/XRT</i>	$7.9^{+0.5}_{-0.4} \times 10^5$	$3.1^{+0.6}_{-0.6} \times 10^{11}$	...	...	39.4/51
	59278 <sup>+9</sup> <sub>-8</sub>	<i>Swift/XRT</i>	$7.9 \times 10^5$ (fixed)	$2.7^{+0.2}_{-0.2} \times 10^{11}$	$0.31^{+0.69}_{-0.12}$	$3.0^{+0.4}_{-0.4}$	70.4/90
	59349	<i>XMM-Newton</i>	$7.9 \times 10^5$ (fixed)	$1.5^{+0.8}_{-0.2} \times 10^{11}$	$0.44^{+0.18}_{-0.24}$	$2.9^{+0.1}_{-0.2}$	56.4/56
	59373 <sup>+12</sup> <sub>-11</sub>	<i>Swift/XRT</i>	$7.9 \times 10^5$ (fixed)	$2.0^{+0.2}_{-0.2} \times 10^{11}$	$0.48^{+0.25}_{-0.15}$	$2.6^{+0.2}_{-0.2}$	117.4/126
59712	<i>XMM-Newton</i>	$7.9 \times 10^5$ (fixed)	$2.9^{+3.3}_{-0.2} \times 10^{11}$	$0.12^{+0.07}_{-0.06}$	$3.1^{+0.8}_{-0.5}$	12.2/16	
AT2021ehb	59407 <sup>+10</sup> <sub>-10</sub>	<i>Swift/XRT</i>	$1.3^{+0.2}_{-0.1} \times 10^6$	$2.5^{+0.6}_{-0.3} \times 10^{10}$	$0.04^{+0.04}_{-0.01}$	$1.4^{+1.3}_{-0.4}$	78.8/98
	59430	<i>XMM-Newton</i>	$6.0^{+0.2}_{-0.2} \times 10^5$	$1.4^{+0.2}_{-0.1} \times 10^{12}$	$0.06^{+0.02}_{-0.01}$	$4.4^{+0.2}_{-0.2}$	48.7/45
	59441 <sup>+15</sup> <sub>-16</sub>	<i>Swift/XRT</i>	$6.4^{+1.1}_{-0.6} \times 10^5$	$3.8^{+1.8}_{-1.3} \times 10^{11}$	$0.21^{+0.10}_{-0.12}$	$4.1^{+0.3}_{-0.5}$	153.2/156
	59475 <sup>+12</sup> <sub>-12</sub>	<i>Swift/XRT</i>	$9.3^{+0.5}_{-0.5} \times 10^5$	$1.5^{+0.2}_{-0.2} \times 10^{11}$	$0.13^{+0.03}_{-0.02}$	$2.7^{+0.2}_{-0.2}$	262.8/250
	59509 <sup>+12</sup> <sub>-16</sub>	<i>Swift/XRT</i>	$1.2^{+0.1}_{-0.1} \times 10^6$	$7.6^{+1.4}_{-1.0} \times 10^{10}$	$0.20^{+0.04}_{-0.03}$	$2.2^{+0.1}_{-0.1}$	285.4/306
	59539 <sup>+10</sup> <sub>-10</sub>	<i>Swift/XRT</i>	$1.5^{+0.1}_{-0.1} \times 10^6$	$4.0^{+0.8}_{-0.6} \times 10^{10}$	$0.27^{+0.04}_{-0.04}$	$1.9^{+0.1}_{-0.2}$	285.4/359
	59565 <sup>+8</sup> <sub>-9</sub>	<i>Swift/XRT</i>	$1.0^{+0.1}_{-0.1} \times 10^6$	$1.3^{+0.7}_{-0.3} \times 10^{11}$	$0.59^{+0.04}_{-0.05}$	$2.0^{+0.1}_{-0.1}$	401.2/467
	59585 <sup>+7</sup> <sub>-7</sub>	<i>Swift/XRT</i>	$1.3^{+0.2}_{-0.2} \times 10^6$	$9.7^{+4.1}_{-2.5} \times 10^{10}$	$0.59^{+0.07}_{-0.06}$	$1.9^{+0.1}_{-0.1}$	455.9/476
	59604	<i>XMM-Newton</i>	$1.2^{+0.1}_{-0.1} \times 10^6$	$8.6^{+0.7}_{-0.6} \times 10^{10}$	$0.13^{+0.02}_{-0.02}$	$2.8^{+0.1}_{-0.1}$	77.6/79
	59640 <sup>+7</sup> <sub>-7</sub>	<i>Swift/XRT</i>	$1.1^{+0.1}_{-0.1} \times 10^6$	$5.6^{+1.5}_{-0.9} \times 10^{10}$	$0.20^{+0.05}_{-0.04}$	$2.3^{+0.2}_{-0.2}$	183.5/214
59661 <sup>+7</sup> <sub>-7</sub>	<i>Swift/XRT</i>	$3.9^{+1.3}_{-1.2} \times 10^5$	$8.3^{+22.9}_{-5.1} \times 10^{11}$	$0.31^{+0.15}_{-0.09}$	$3.5^{+0.3}_{-0.3}$	66.5/85	
59825	<i>XMM-Newton</i>	$1.6^{+0.2}_{-0.1} \times 10^6$	$2.8^{+0.6}_{-0.5} \times 10^{10}$	$0.22^{+0.06}_{-0.04}$	$2.2^{+0.1}_{-0.1}$	77.2/71	
AT2021yzv	59654	<i>XMM-Newton</i>	$1.0^{+0.6}_{-0.3} \times 10^6$	$1.5^{+13.2}_{-0.9} \times 10^{11}$	...	...	2.9/3
ASASSN-14li	56997	<i>XMM-Newton</i>	$4.1^{+0.1}_{-0.1} \times 10^5$	$3.7^{+0.1}_{-0.1} \times 10^{12}$	...	...	66.3/31
	57023	<i>XMM-Newton</i>	$4.0^{+0.1}_{-0.1} \times 10^5$	$3.8^{+0.1}_{-0.1} \times 10^{12}$	...	...	98.9/25
	57213	<i>XMM-Newton</i>	$3.3^{+0.1}_{-0.1} \times 10^5$	$4.2^{+0.1}_{-0.1} \times 10^{12}$	...	...	21.6/19
	57399	<i>XMM-Newton</i>	$3.0^{+0.1}_{-0.1} \times 10^5$	$4.9^{+0.2}_{-0.2} \times 10^{12}$	...	...	26.5/18
	57726	<i>XMM-Newton</i>	$2.7^{+0.1}_{-0.1} \times 10^5$	$4.8^{+0.3}_{-0.3} \times 10^{12}$	...	...	22.7/12
	58092	<i>XMM-Newton</i>	$2.3^{+0.1}_{-0.1} \times 10^5$	$6.0^{+0.6}_{-0.5} \times 10^{12}$	...	...	18.3/13
ASASSN-15oi	57324	<i>XMM-Newton</i>	$5.2^{+0.1}_{-0.1} \times 10^5$	$5.4^{+0.4}_{-1.6} \times 10^{11}$	...	...	12.7/7
	57482	<i>XMM-Newton</i>	$3.3^{+0.3}_{-0.1} \times 10^5$	$3.3^{+1.8}_{-0.1} \times 10^{12}$	...	...	15.8/10
AT2018fyk	58404 <sup>+13</sup> <sub>-21</sub>	<i>Swift/XRT</i>	$1.3^{+0.1}_{-0.1} \times 10^6$	$1.1^{+0.2}_{-0.1} \times 10^{11}$	$0.01^{+0.04}_{-0.01}$	$1.9^{+1.5}_{-0.9}$	101.5/108
	58436 <sup>+23</sup> <sub>-16</sub>	<i>Swift/XRT</i>	$1.2^{+0.1}_{-0.1} \times 10^6$	$1.4^{+0.4}_{-0.2} \times 10^{11}$	$0.05^{+0.06}_{-0.03}$	$2.4^{+0.6}_{-0.6}$	128.1/117
	58461	<i>XMM-Newton</i>	$1.2^{+0.1}_{-0.1} \times 10^6$	$1.5^{+0.1}_{-0.1} \times 10^{11}$	...	...	32.5/31
	58476 <sup>+15</sup> <sub>-12</sub>	<i>Swift/XRT</i>	$1.3^{+0.1}_{-0.1} \times 10^6$	$1.1^{+0.3}_{-0.2} \times 10^{11}$	$0.01^{+0.02}_{-0.01}$	$1.4^{+0.7}_{-0.5}$	112.9/103
	58598 <sup>+34</sup> <sub>-35</sub>	<i>Swift/XRT</i>	$1.7^{+0.1}_{-0.1} \times 10^6$	$9.1^{+0.9}_{-0.7} \times 10^{10}$	$0.19^{+0.03}_{-0.02}$	$2.1^{+0.1}_{-0.1}$	428.0/470
	58681 <sup>+30</sup> <sub>-45</sub>	<i>Swift/XRT</i>	$1.4^{+0.1}_{-0.1} \times 10^6$	$1.2^{+0.3}_{-0.2} \times 10^{11}$	$0.27^{+0.05}_{-0.04}$	$2.3^{+0.1}_{-0.1}$	372.8/354
	58745 <sup>+34</sup> <sub>-28</sub>	<i>Swift/XRT</i>	$1.8^{+0.3}_{-0.3} \times 10^6$	$4.7^{+2.2}_{-1.1} \times 10^{10}$	$0.13^{+0.09}_{-0.05}$	$1.8^{+0.3}_{-0.3}$	165.6/194
	58783	<i>XMM-Newton</i>	$1.3^{+0.1}_{-0.1} \times 10^6$	$1.1^{+0.1}_{-0.1} \times 10^{11}$	$0.16^{+0.01}_{-0.01}$	$2.2^{+0.1}_{-0.1}$	160.4/136
58822 <sup>+35</sup> <sub>-38</sub>	<i>Swift/XRT</i>	$2.1^{+0.2}_{-0.2} \times 10^6$	$4.0^{+1.0}_{-0.6} \times 10^{10}$	$0.14^{+0.06}_{-0.04}$	$1.7^{+0.2}_{-0.2}$	221.4/282	
OGLE16aaa	57548	<i>XMM-Newton</i>	$5.6^{+0.9}_{-0.8} \times 10^5$	$4.1^{+4.6}_{-1.6} \times 10^{11}$	...	...	11.1/16
	57558 <sup>+1</sup> <sub>-1</sub>	<i>Swift/XRT</i>	$5.6^{+0.9}_{-0.7} \times 10^5$	$2.5^{+2.1}_{-1.0} \times 10^{12}$	...	...	9.2/15
	57722	<i>XMM-Newton</i>	$5.5^{+0.2}_{-0.2} \times 10^5$	$1.4^{+0.2}_{-0.1} \times 10^{12}$	...	...	12.0/15

NOTE—(a)  $\chi^2$ -statistics for *XMM-Newton* spectra, and 'c-statistics' (Cash 1979) for *Swift/XRT* spectra.